

Cluster search for neutrinos from Active Galactic Nuclei

Cluster-Suche nach Neutrinos von
aktiven Galaxienkernen

Der Naturwissenschaftlichen Fakultät der
Friedrich-Alexander-Universität Erlangen-Nürnberg

zur

Erlangung des Doktorgrades Dr. rer. nat.



vorgelegt von

Ulf Fritsch

aus Forchheim

Juni 2014

Als Dissertation genehmigt von der Naturwissenschaftlichen Fakultät der
Friedrich-Alexander-Universität Erlangen-Nürnberg

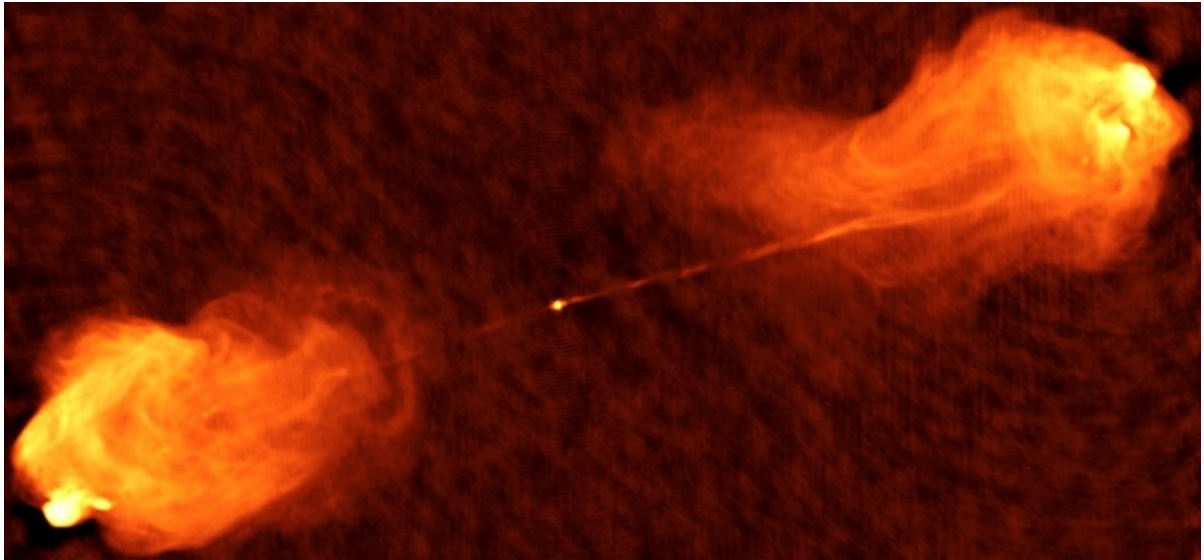


Fig.: http://www.nasa.gov/images/content/188385main_CygA-YellowOrange_med.jpg



Tag der mündlichen Prüfung:20.10.2014
Vorsitzender des Promotionsorgans:Prof. Dr. Johannes Barth
Gutachter/in:Prof. Dr. Ulrich Ferdinand Katz
Gutachter/in:Prof. Dr. Gisela Anton

ECAP-2014-010

Für meine Familie Carola, Klaus und Nico und meine allerliebste Kathrin.

“Falls Gott die Welt geschaffen hat, war seine Hauptsorge sicher nicht, sie so zu machen, dass wir sie verstehen können.” (Albert Einstein).

Abstract

The ANTARES neutrino telescope in the Mediterranean Sea near Toulon, France, is the world's only subsea Cherenkov telescope for the detection of astrophysical high-energy neutrinos. 885 photomultipliers are mounted on 500 m long flexible cables that are anchored on the seabed and pulled tight by submersed buoys. Due to underwater sea currents the detector units are tilted and their positions are time dependent. As the reconstruction software tries to find particle tracks from time-stamped photomultiplier hits in the detector, the detector alignment system is a crucial part of the calibration task of the telescope. I have developed, successfully tested and frequently improved the software for the position reconstruction including its data-I/O interface to the central ORACLE-database in Lyon. The software, the implemented algorithm and cross-checks with other ANTARES measurements are presented. The work is also summarized in the paper "The Positioning System of the ANTARES Neutrino Telescope" [1] available from

<http://iopscience.iop.org/1748-0221/7/08/T08002/>.

The main goal of neutrino astronomy using large-scale high-energy neutrino telescopes is the identification of neutrino point-sources in the sky. From theoretical predictions and measurements of high energetic gamma-rays, hadronic particle accelerators candidates in the universe have been identified. From these sources like supernova remnants, gamma ray bursts or active galactic nuclei neutrino emission is predicted. As ANTARES is located on the Northern Hemisphere and looks for neutrinos from the southern sky, the TANAMI (Tracking Active Galactic Nuclei with Austral Milliarcsecond Interferometry) sample of radio-loud and variable AGN south of declination -30 degrees is an ideal target sample. Data from the Large Area Telescope on the *Fermi* satellite show variable photon fluxes on timescales of several weeks and months from many of these sources. I have developed an analysis to search for time-clustered neutrino events, including the full range from event handling up to calculation of statistical parameters. I have chosen 24 sources from the TANAMI sample to look at. For six of them, equally spread over the declination range, a dedicated flare simulation has been performed to test the code. The discovery potential as function of cone size and cuts on track reconstruction quality for the six sources is presented.

In order to test the analysis method on real data, for a small sub-sample of eight sources with a reasonable spread over the sky the data has been unblinded. No significant cluster of neutrino events was found in the data. For the source PKS0208-512, two events were found, for 1954-388 one event. Consequently flux limits are presented for the unblinded sources.

Zusammenfassung

Das ANTARES Neutrinooteleskop, welches sich im Mittelmeer nahe Toulon, Frankreich, befindet, ist derzeit das einzige Tiefseeteleskop zur Messung von hochenergetischen Neutrinos aus astrophysikalischen Quellen. Es besteht aus 885 Photomultipliern, die an 500 m langen flexiblen Kabeln befestigt sind. Die Kabeln werden am Boden mittels eines Ankers fixiert und durch eine Boje straff gehalten. Aufgrund von zeitlich veränderlichen Unterwasserströmungen werden die Kabel ausgelenkt und die Detektorgeometrie wird zeitabhängig. Da die Rekonstruktionssoftware aus der Zeit- und Ortsinformation von Photomultipliersignalen eine Teilchenspur berechnet, wird eine alle zwei Minuten aktualisierte Detektorgeometrie benötigt. Dazu habe ich die benötigte Software entwickelt und getestet, welche sowohl für die Positionsberechnung an sich als auch für den Datenaustausch mit der zentralen ORACLE-Datenbank verantwortlich ist. Diese Arbeit ist auch wichtiger Bestandteil der folgenden ANATARES-Veröffentlichung [1]:

<http://iopscience.iop.org/1748-0221/7/08/T08002/>.

Das große Ziel im Bereich der Neutrinoastronomie ist die Identifikation von Punktquellen am Himmel. Aufgrund theoretischer Vorhersagen und Messungen von hochenergetischer Gamma-Strahlung weiß man dass im Universum Objekte mit hadronischen Beschleunigungsmechanismen existieren, die mit Neutrioemission einhergehen. Quellen wie Supernova-Überreste, Gamma-ray Bursts oder aktiven Galaxienkernen sind derartige Kandidaten. Aufgrund seiner Lage auf der nördlichen Hemisphäre ist das ANTARES Neutrinooteleskop für die Beobachtung der am Südhimmel gelegenen TANAMI (Tracking Active Galactic Nuclei with Austral Milliarcsecond Interferometry) AGNs, welche radio-laut und variabel sind, besonders geeignet. Daten des Large Area Teleskops auf dem Fermi Satelliten zeigen stark variable Photonenströme auf Zeitskalen von mehrere Wochen bis Monaten. Ich habe daher ein neues Softwarepaket zur Auswertung von zeitlich geclusterten Neutrinoevents für ANTARES entworfen und getestet. 24 TANAMI Quellen wurden für diese und kommende Analysen ausgewählt.

Um die Analyse an echten Daten zu testen, wurde ein Subsample von acht Quellen für ein Unblinding ausgewählt, wobei darauf geachtet wurde, dass diese eine möglichst homogene Verteilung am Himmel besitzen. Es konnte kein signifikanter Cluster von Events in den ANTARES Daten gefunden werden. Für die Quelle PKS0208-512 wurden zwei Ereignisse gezählt, für 1954-388 eines. Limits auf den Fluss für die acht Quellen wurden berechnet.

Contents

1	Introduction	11
2	Neutrino sources	13
2.1	Atmospheric neutrinos	13
2.2	Non-AGN neutrino sources	14
2.3	Active Galactic Nuclei	19
3	Neutrino astronomy	23
3.1	The neutrino as a messenger particle	23
3.2	Neutrino detection principle	23
3.3	Experimental signatures from neutrinos	25
3.4	Muon propagation and the Cherenkov effect	26
3.4.1	Muon propagation	26
3.4.2	The Cherenkov effect and light propagation in water	27
3.5	Background for undersea neutrino detection	29
3.5.1	Particle background	29
3.5.2	Optical background	30
3.6	Previous and current neutrino telescopes	30
4	The ANTARES neutrino telescope	35
4.1	Detector layout	35
4.2	Data acquisition and triggers	39
4.3	Time and charge calibration	40
4.3.1	Time calibration	40
4.3.2	Charge calibration	42
5	The alignment of ANTARES	45
5.1	The sea at the ANTARES site	45
5.2	Coordinate systems	47
5.3	Hardware components and measured quantities	49
5.4	In situ calibration of tiltmeters and compasses	50
5.5	Mechanical line shape model	52
5.6	The χ^2 -fit	56
5.7	Nominal detector geometry	57
5.8	AlignReco software, data processing and data storage	57
5.9	Geometry reader for SeaTray	58
5.10	Quality and accuracy of alignment data	59

5.11	Conclusion	63
6	Cluster search	67
6.1	Introduction	67
6.2	The TANAMI program and source candidate selection	68
6.2.1	The TANAMI program	68
6.2.2	Selected sources and observation period	70
6.3	AAFit-strategy, official data production and run selection	72
6.3.1	AAFit strategy and official data production	72
6.3.2	Run selection	78
6.4	Selection of signal events	80
6.5	Scrambled skymaps from data	81
6.6	Comparison of data and Monte Carlo	82
6.6.1	Run-by-run Monte Carlo	82
6.6.2	Monte Carlo simulation chain	82
6.6.3	Event weighting	85
6.6.4	Results and conclusion	85
6.7	Background estimation	90
6.7.1	Assuming a constant background rate	90
6.8	Source flux simulation	90
6.8.1	Introduction and procedure	90
6.8.2	Generating events, absolute event times and weights	94
6.8.3	Sampling events	97
6.8.4	Reconstruction, injection and source association	98
6.9	Clustering	98
6.9.1	Cluster definition	99
6.9.2	Software and procedure	100
6.10	Calculation of p -values	102
6.10.1	Expected number of clusters	102
6.10.2	p -values	104
6.11	Discovery scenario and trail correction	107
6.12	Errors on p -values from rate variations	108
7	Results from simulation	111
7.1	Discovery potential and sensitivity	111
7.1.1	Cone size for $\Lambda > -5.2$	111
7.1.2	Λ -cut	111
7.2	Simulation of a short-duration flare	116
7.3	Time variable background	116
7.4	Conclusion from simulation	120
7.5	Limit setting procedure	120
8	Results after unblinding	123
8.1	Unblinding request	123
8.2	Results after unblinding	124

9 Conclusion and outlook	131
10 Appendix	133
10.1 List of run numbers	133
10.2 Sparking runs	136
10.3 Baseline rate	137
10.4 GPS timestamp	137
10.5 Random time generation	137
10.6 Astro-package and coordinate transformations benchmark	138
10.7 Check on SeaTray internal angle conversion	139
10.8 Additional material on alignment	139
10.8.1 AlignReco versions	139
10.8.2 Data format and database tables for detector geometries	140
Bibliography	149
Danksagung/Lebenslauf	159

Contents

1 Introduction

In 1930 the energy distribution of electrons in β -decays, measured to be continuous, which is only possible for a three-body decay, led Wolfgang Pauli to postulate a new particle: the neutrino. Three years later, a theoretical formalism for the β -decay including Pauli's new particle was found by Enrico Fermi. As the neutrino is electrically neutral and has a tiny mass, its detection becomes an experimental challenge. Many years after its postulation, the neutrino was discovered in 1956 by Reines and Cowan using the high $\bar{\nu}_e$ -flux from a nuclear power plant. In 1967 Davis and others started to measure solar neutrinos using a large radio-chemical experiment in the Homestake mine in the USA. The results, which were incompatible with theoretical flux predictions from the Sun's fusion processes, were called the "solar neutrino problem". The deficit in solar neutrinos was confirmed by the experiments GALLEX¹, SAGE² and Kamiokande. With the detection of a clear oscillation pattern of atmospheric neutrinos in 1998 by Super-Kamiokande a consistent picture of neutrino oscillations emerged that also explained the solar neutrino problem.

Besides the Sun and anthropogenic sources, physicists started to consider other sources of neutrino emission in the universe: theoretical predictions of fundamental astrophysical processes like supernovae explosions (neutrinos from the Supernova 1987A in 1987 were detected by Kamiokande and IMB), gamma-ray bursts and jet ejections of active galactic nuclei as well as measurements of ultra high-energetic photons and cosmic rays give many hints for neutrino emission in the Universe. An overview of these sources and the neutrino production mechanisms can be found in chapter 2. The community started early to develop and probe the first large-scale water and ice detectors like the Lake-Baikal neutrino telescope [2] or the AMANDA [3] in-ice detector at the South Pole for the detection of high-energy neutrinos. The principles of high-energy neutrino detection using 3D-arrays of photomultipliers and an overview of running and outdated experiments is discussed in chapter 3.

In 2008, the first deep-sea neutrino telescope ANTARES was completed and is since then taking data in its full configuration comprising more than 800 photomultipliers spread in an instrumented volume of $\approx 0.01 \text{ km}^3$. ANTARES has been deployed in the Mediterranean Sea at a depth of roughly 2500 m near the coast off Toulon, France. As this thesis is based on data obtained with ANTARES, the layout, functionality and parts of the calibration topics for this telescope are described in chapter 4. Undersea telescopes like ANTARES have to deal with a particular topic concerning the calibration: As variable sea currents result in a time-dependent detector geometry, the positions of detection units must be monitored with a reasonable time sampling.

¹German-Italian GALLIum EXperiment

²Soviet American Gallium Experiment

1 Introduction

The methods and software developed for the position calibration of ANTARES are explained in detail in chapter 5.

One of most the interesting puzzles to be solved in the field of astroparticle physics is the origin of ultra-high-energetic cosmic rays. Events in the region of 10^{19} eV have been observed. The ultra-relativistic outflow of AGN jets is one of the promising sites for acceleration processes up to these energies. As a direct consequence of a possible hadronic particle acceleration, the emission of high-energy neutrinos is expected. Unfortunately, no point-like neutrino sources have been detected so far by the currently operating neutrino telescopes (IceCube has detected a significant diffuse neutrino signal in 2013 [4]). A discovery of neutrino emission from AGN jets would help a lot to understand the processes in these sources and also to provide substantial input for simulation scenarios that might lead to a better understanding of jet formation, jet collimation and propagation over distances of several hundred Schwarzschild radii away from the central black hole.

The formation of AGN jets itself is attributed only to a fraction of all existing black hole systems: the ones that show radio emission, so-called radio-loud objects. As ANTARES is located on the Northern Hemisphere and therefore observes the southern sky, the TANAMI [5] radio-selected sample of radio-bright AGN at declinations lower than -30 degrees yields excellent candidate sources. TANAMI sources are regularly observed by radio telescope arrays resulting in milliarcsecond resolution images using very long baseline interferometry [6]. This technique provides access to detailed jet structures and from longterm observations also to dynamic jet phenomena like material ejection. Since the launch of the *Fermi* satellite [7] and its gamma-ray monitor LAT (Large Area Telescope), multi-wavelength information is available. Gamma-ray flux measurements of these sources show variabilities on a wide range of timescales. These observations are supplemented by searching for neutrino signals using the ANTARES telescope. For this reason a new search on time-clustered neutrino emission within ANTARES has been designed (chapter 6). The analysis is meant to be sensitive to any time clustered neutrino emission within a certain observation period from a given source. The work is the first approach to search for neutrino signal from radio-bright AGN on the Southern sky. The search method has been tested using Monte Carlo simulations. The TANAMI program, the search method and tests by Monte Carlo simulations are presented in chapter 7. The application to real data and the results are described in chapter 8. Chapter 9 gives a conclusion and an outlook to subsequent analyses using the experience from this work.

2 Neutrino sources

In brief:

- Due to interaction of cosmic rays with the Earth's atmosphere large numbers of high-energy muon-neutrinos are produced.
- For the observation of cosmic neutrino emitters by high-energy neutrino telescopes on Earth these atmospheric neutrinos and muons are the main sources of background.
- Several assumed galactic and extragalactic neutrino sources such as Gamma Ray Bursts, Supernova remnants and Active Galactic Nuclei are under observation by currently operating neutrino telescopes.
- Particle acceleration mechanisms in Active Galactic Nuclei (AGN) are still barely understood. A detection of neutrinos from these sources would change the situation dramatically.

This chapter gives an overview of the relevant neutrino sources in the field of neutrino astronomy. It is divided in a section on atmospheric neutrinos, a section on galactic and extra-galactic sources (excluding AGN) and finally one on AGN itself. As this thesis pursues a search for AGN neutrinos, there is a particular focus on this source type (see also Chapter 6).

2.1 Atmospheric neutrinos

The Earth's atmosphere plays an important role for neutrino astronomy. Due to the interaction of cosmic rays abundant neutrinos are created there (for cosmic ray spectrum see figure 2.1 left). Atmospheric neutrinos [15] are produced from primary cosmic rays in pion and subsequent muon decays via

$$\pi^\pm \rightarrow \mu^\pm + \nu_\mu(\bar{\nu}_\mu) \rightarrow e^\pm + \nu_e(\bar{\nu}_e) + \bar{\nu}_\mu(\nu_\mu) + \nu_\mu(\bar{\nu}_\mu) \quad (2.1)$$

From these equations (excluding neutrino oscillations) one expects for the ratio between flavours a value of $r = \frac{N_{\nu_\mu + \bar{\nu}_\mu}}{N_{\nu_e + \bar{\nu}_e}} \approx 2$. The ratio r is rising as a function of energy (muons start to reach the ground). The measured flavour ratios are now consistent with neutrino oscillation scenarios (see [16, 17] for examples).

For neutrino telescopes atmospheric neutrinos are an irreducible background. For energies higher than 100 GeV (see figure 8 in [18]) neutrinos from kaon decays become

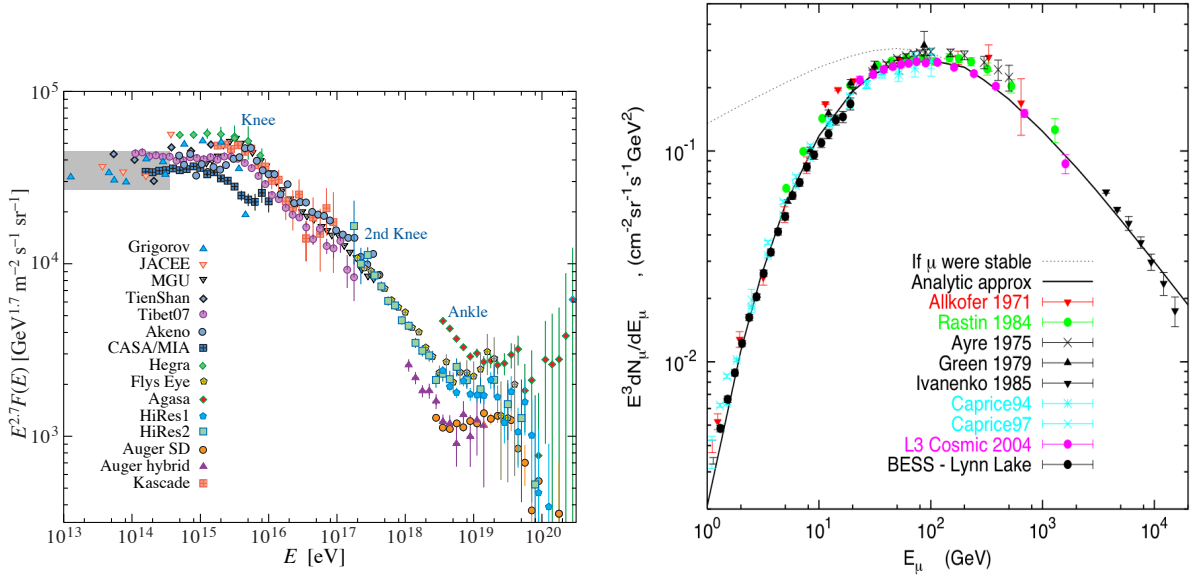


Figure 2.1: *Left*: Cosmic ray all-particle spectrum (flux multiplied by $E^{2.7}$ to emphasize the knee at $3 \cdot 10^{15}$ eV). Measurements from various experiments are shown (figure from [8]). *Right*: Vertical atmospheric muon flux at ground level (figure from [9]).

important: For example $K^\pm \rightarrow \mu^\pm \nu_\mu (\bar{\nu}_\mu)$, $K^\pm \rightarrow \pi^0 e^\pm \nu_e (\bar{\nu}_e)$ in the leptonic and semileptonic channels and $K^\pm \rightarrow \pi^0 \pi^\pm$ in the hadronic channel. As can be seen from the decay chains above, not only neutrinos but also muons are produced in these interaction processes. They become the second component of background for neutrino telescopes. See also figure 2.1 right for expected flux at ground level.

In principle, there are several methods to distinguish atmospheric neutrino events from astrophysical ones, like time and space clustering or the characteristic zenith angle dependence.

For higher energies the different spectral indices of the flux between cosmic and atmospheric ($\alpha \approx 3.7$) neutrinos provide another method to distinguish those two neutrino sources. The main features of the atmospheric neutrino flux are known since the 1960s. Figure 2.2 shows calculations from various authors using different interaction modeling. Uncertainties range from $\pm 15\%$ in the GeV range up to $\pm 40\%$ in the TeV range [15]. At low energies the uncertainties are dominated by uncertainties of hadronic interaction processes, while at larger energies they arise from uncertainties of the primary cosmic ray spectrum. At even higher energies charmed hadron production will become the major source of uncertainty.

2.2 Non-AGN neutrino sources

While atmospheric neutrinos are mainly background that can be used for calibration and fundamental understanding of neutrino telescopes, neutrino astronomers would

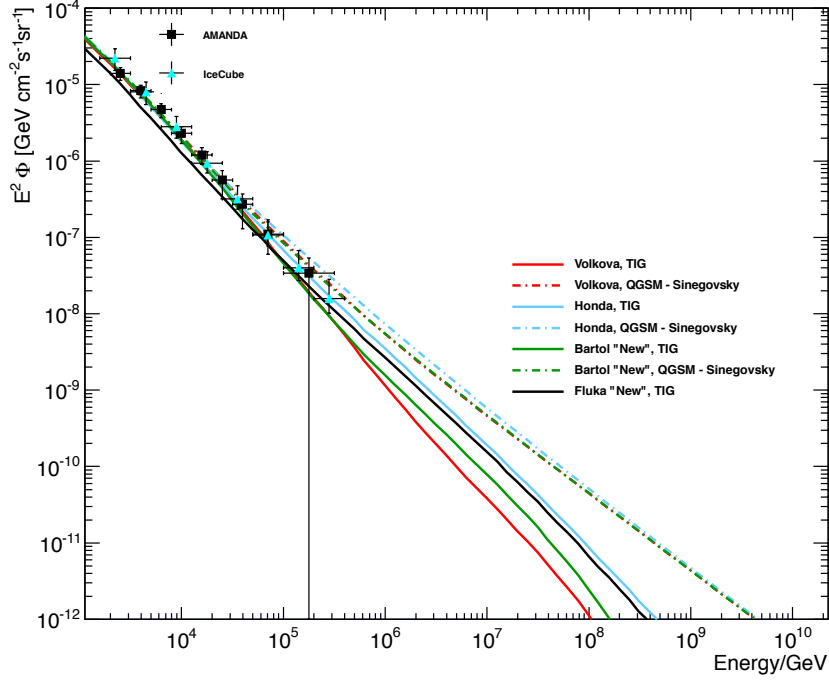


Figure 2.2: Atmospheric neutrino flux up to 10^{10} GeV. Measurements from IceCube and Amanda are shown (figure by Dominick Stransky (ECAP Erlangen) [10], see also [11], [12], [13], [14]).

like to detect signals from astrophysical objects like Supernovae and Supernova Remnants (SNe, SNRs), Gamma Ray Bursts (GRBs) and Active Galactic Nuclei for example. Also Dark Matter (DM) annihilations could produce neutrinos detectable on Earth.

Supernovae

In 1987 it was possible to record 20 (mainly $\bar{\nu}_e$, time-spread of ~ 10 s) out of 10^{58} neutrinos released in the supernova 1987A [19] in the Large Magellanic Cloud, 160000 Lys away, by the two experiments Super-K and SNO [20,21]. During the final collapse and the so-called deleptonization phase a first neutrino burst is created via

$$e^- + p \rightarrow n + \nu_e. \quad (2.2)$$

As the above equation shows, only electron neutrinos are created. In a second phase the huge amount of thermal energy is radiated: During this phase the resulting neutron star is able to produce neutrinos of all flavours coming from electron-positron pairs (produced by photons):

$$e^+ + e^- \rightarrow \nu_\ell + \bar{\nu}_\ell \quad \ell = e, \mu, \tau. \quad (2.3)$$

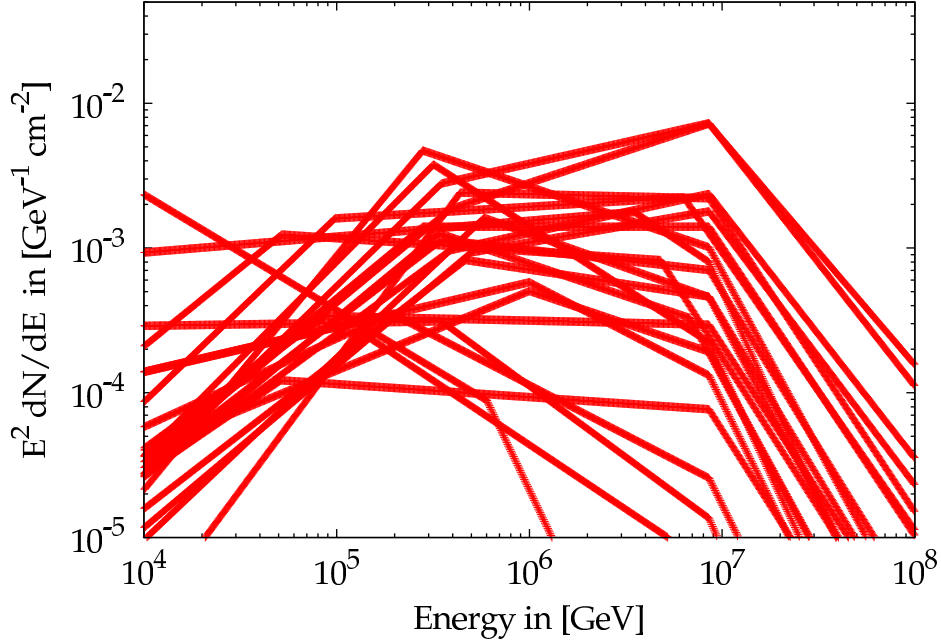


Figure 2.3: Neutrino spectra for a selection of GRBs between 2007 and 2009 with expected neutrino fluxes $> 10^{-8}$ $1/\text{cm}^2$ (above 1 TeV), visible for ANTARES and occurred during low background runs (figure from [22]).

99% of the total energy budget available is taken away by neutrino emission: For example a 10 km 1.4 solar mass star provides $GM^2/2R$ or roughly 10^{53} ergs (1 erg = 10^{-7} J) of gravitational energy. As neutrinos from SNe are in the 10 MeV range (10-30 MeV), no track-like signatures can be measured by high-energy neutrino telescopes. The expected signature for neutrino telescopes would be a simultaneous rise of the photomultiplier counting rates produced by Cherenkov light from electrons in the vicinity of the photomultipliers in water or ice.

Gamma Ray Bursts

Gamma Ray Bursts [23] are the most luminous objects ($10^{51} - 10^{54}$ erg/s) within the Universe. They are distributed isotropically over the sky and can be described by the so-called fireball-model [24]. The enormous amount of released energy on short timescales of seconds and variabilities on scales of microseconds confines the emission region to a size of $r \sim 10^7$ cm. This innermost area is an optically thick plasma of e^+ , e^- and photons, the so-called fireball. Observations of non-thermal emission spectra can be explained by an optical thin emission region which is moving at ultra-relativistic speeds. This region is assumed to be an ejection of shells from the initial compact object. Further afterglow observations provide strong evidence on the fireball-model. For detailed informations on the fireball-model see [25].

From GRBs neutrinos at energies of $10^{13} - 10^{17}$ eV are expected (see figure 2.3). More than 10% of the fireball-energy is expected to be emitted in neutrinos. They are created by pion decay (see equation 2.1). Pions are produced by photo-meson produc-

tion from fireball γ -rays (~ 1 MeV) and fermi-accelerated protons ($\sim 10^{15}$ eV). The neutrino roughly carries 5% of the initial proton energy. The expected neutrino spectrum would be a double broken power law spectrum with three indices and two break energies. The first break comes with the Δ -resonance, while the second break is due to synchrotron cooling of pions and muons before they produce neutrinos (for detailed calculations see [26]). The burst duration varies between a fraction of seconds (short GRBs) to hundreds of seconds (long GRBs). This gives neutrino telescopes the chance to look for events in relatively short time intervals. Therefore significant observations can be possible by detecting a single event. The detection of neutrinos from GRBs could test several scenarios and theories like hadronic particle acceleration, the weak equivalence principle (by detection neutrino and gamma rays at the same time), the fireball model itself and neutrino oscillation (by observing equally distributed neutrino flavours). See [27] for the latest results from IceCube on neutrino emission from GRBs.

Dark Matter

Several measurements have shown that a large fraction ($\approx 23\%$) of our Universe is made of non-baryonic, so-called Dark Matter. It is expected that each galaxy is surrounded by a DM halo. Supersymmetry (Susy) provides a theoretical model to describe these Dark Matter particles. So-called weakly interacting massive particles (WIMPs) build up the DM component. These particles do only interact via the weak force and via gravitation. Therefore it is expected that Susy-particles can be gravitationally trapped in objects like the Sun or the Earth during the movement of these massive objects in the DM halo of the host galaxy. It is also expected that the lightest supersymmetric particle (LSP) could self-annihilate into Standard Model particles, for example neutrinos. The best motivated LSP is the neutralino χ :

$$\chi\chi \rightarrow \{c\bar{c}, b\bar{b}, t\bar{t}, W^+W^-, \dots\} \rightarrow \nu\bar{\nu} + \text{other particles.} \quad (2.4)$$

Therefore indirect Dark Matter searches are possible by looking for neutrino fluxes from the Sun or the Earth [28–31]. Since neutrinos from these DM annihilations are typically below 100 GeV in energy according to the preferred models, special hardware and software requirements are needed for high energy neutrino telescopes. For example a partly denser instrumented sub-volume of the detector and dedicated hit-selection algorithms can lower the energy threshold for neutrino detection from DM annihilations.

Diffuse neutrino flux

Astrophysicists are not only searching for point sources in the sky, but also try to identify neutrinos from unresolved sources like AGN, GRB or Supernovae that form a diffuse neutrino flux. From cosmic ray observations (Waxmann-Bahcall [34, 35]) and γ -ray data (Mannheim-Protheroe-Rachen [36]) one can deduce an upper limit on the diffuse neutrino flux. The Waxmann-Bahcall upper bound is obtained from cosmic ray data at 10^{19} eV: $E^2\Phi < 4.5/2 \cdot 10^{-8} \text{ GeV cm}^{-2} \text{ sr}^{-1} \text{ s}^{-1}$. The spectrum is expected to be harder than the one from atmospheric neutrinos: $\sim E^{-2}$. Therefore one can search for excesses of high-energy neutrinos. Results from ANTARES and IceCube on the

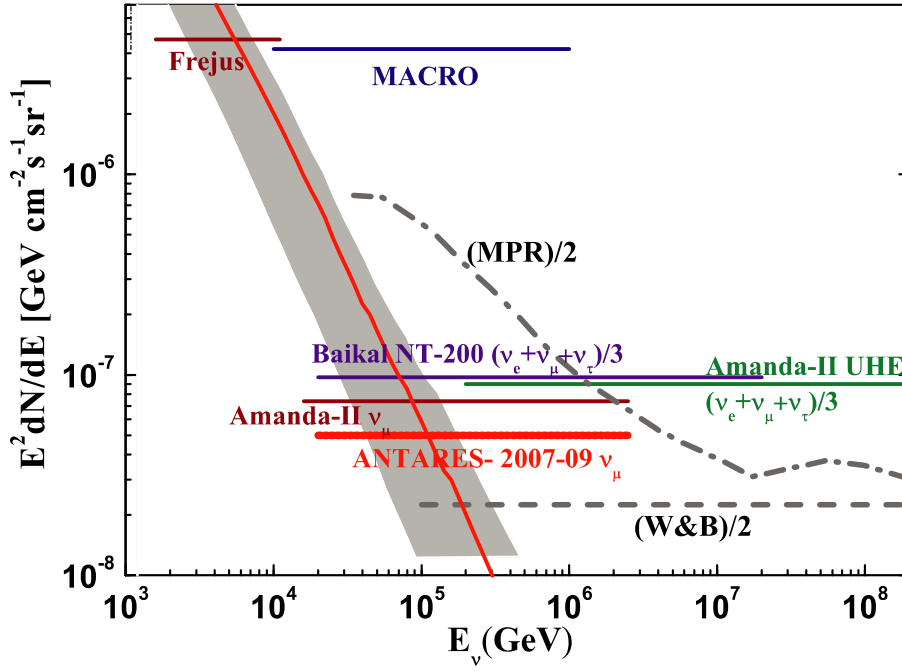


Figure 2.4: ANTARES result (upper limit) for a diffuse $(\nu_\mu + \bar{\nu}_\mu)$ -flux. Limits from other experiments are also shown. The MPR/WMB fluxes are divided by 2 since ANTARES is not sensitive to ν_e . The grey band gives the atmospheric neutrino flux variation. For details and figure reference see [32].

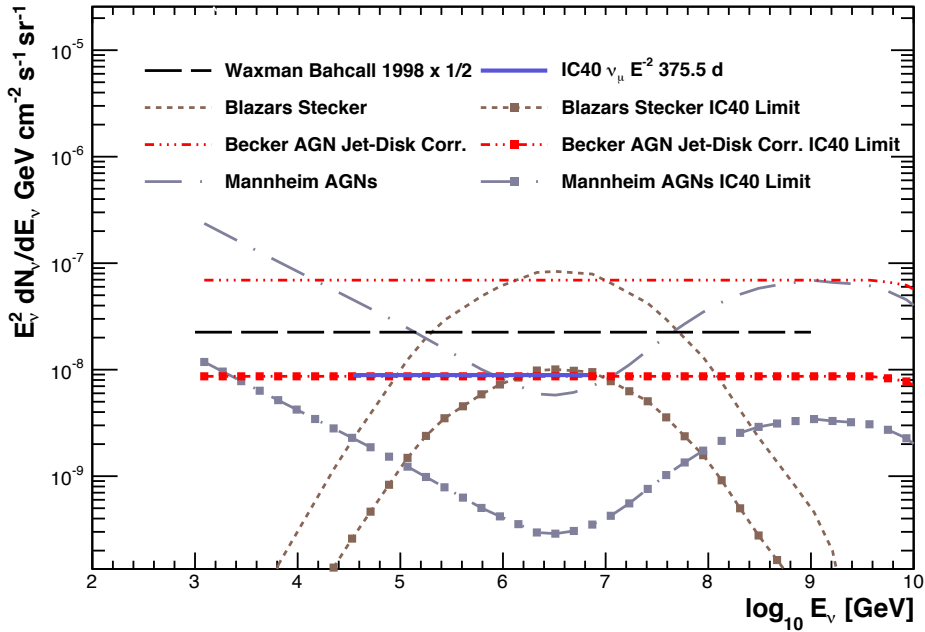


Figure 2.5: Limit on diffuse $(\nu_\mu + \bar{\nu}_\mu)$ -flux obtained by an analysis using the IceCube 40-string detector configuration (IC40). For details and figure reference see [33].

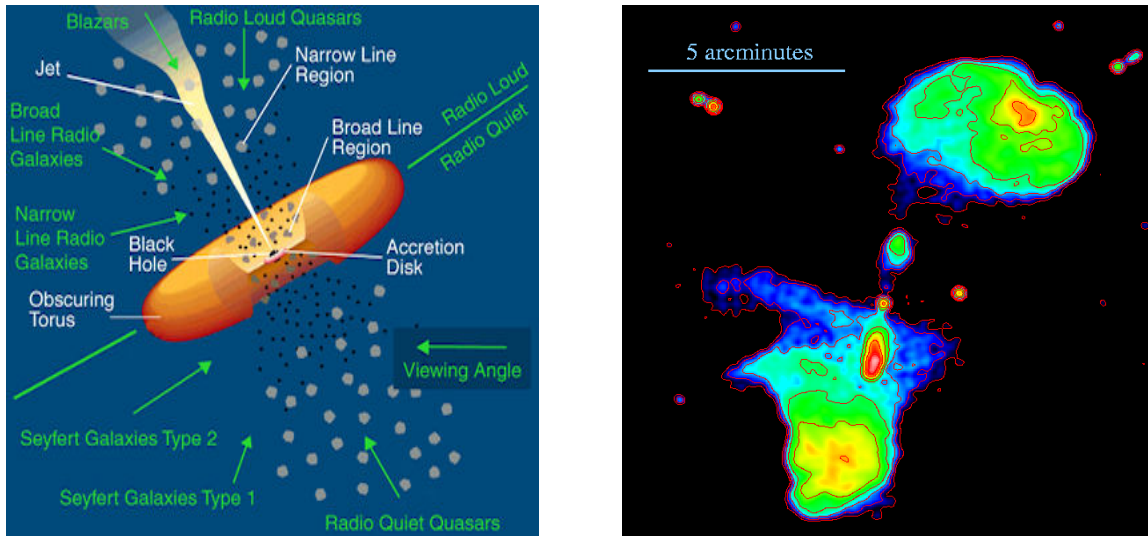


Figure 2.6: *Left:* Topology of AGNs: Detailed view with accretion disk, torus and jet also showing the class objects as function of viewing angle (figure from [37]). *Right:* Radio image of J0116-473. By interaction with the surrounding medium the jets produce large radio lobes (figure from [38]).

diffuse flux limits can be found in [32,33] (see figures 2.4 and 2.5).

Supernova Remnants

Besides AGN the remnants of Supernovae (SNRs) explosions are the most promising sites for hadronic particle acceleration and therefore for neutrino production. During a Supernova the outer shells of the exploding star are ejected into space. Originating from shocks high energetic gamma rays have been measured for example by the HESS experiment. Driven by these observations, hadronic particle acceleration is expected. The detection of high energy neutrinos would be a verification of these acceleration processes. For further details and explicit calculation of the expected neutrino flux for the example of SNR RX J1713.7-3946 refer to [40] and references therein.

2.3 Active Galactic Nuclei

Active Galactic Nuclei are supposed to be strong neutrino sources in the sky [41]. A central black hole is surrounded by an accretion disk where the accretion of matter is the primary energy source of the AGN (see figure 2.6 left). The standard interpretation of the observation of emission spectra is the following: A central continuum source is surrounded by an optically thick obscuring gas and dust torus that prohibits radiation to escape to the side. For some AGN there is an enormous outflow of material, so-called jet, perpendicular to the torus plane. Jet-production is an exclusive phenomenon of AGN with large radio-emission (called radio-load). AGN are rotationally symmetric around the torus or jet axis. As indicated in figure 2.6 left the unified model of AGN can explain a whole class of objects by looking at different angles with respect to

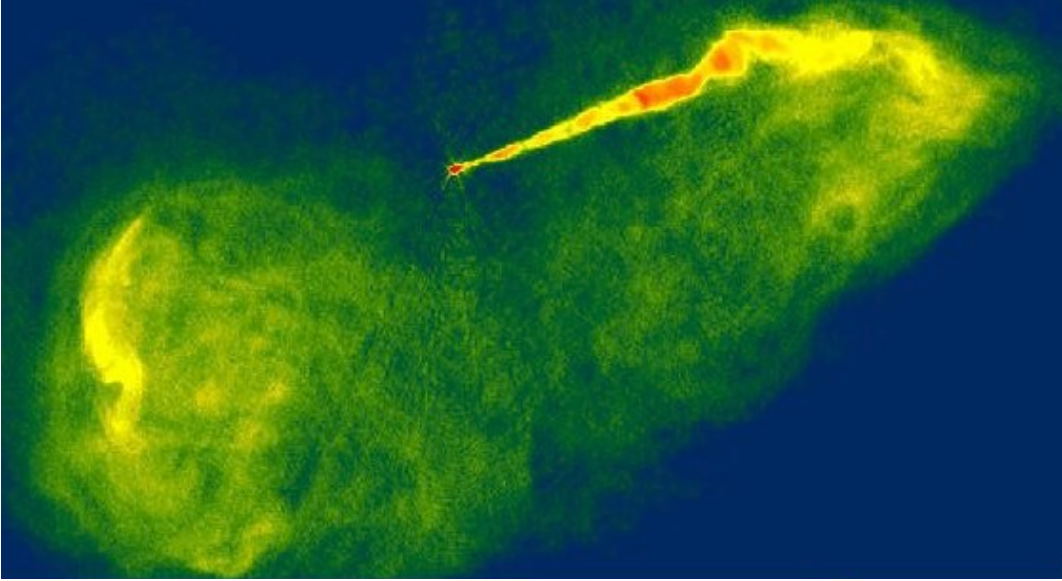


Figure 2.7: VLA-picture of galaxy M87. Due to Doppler boost the jet pointing towards the Earth is fully visible while the counter-jet is not observed. The isotropic emission of the giant lobes, where the jet interacts with the ambient medium is also visible (figure from [39]).

the jet axis. For AGN with large radio emission the emission axis is always aligned with the torus symmetry axis. The interaction of jets with the surrounding matter produces these large areas of radio emission, so-called radio lobes (see figure 2.6 right for example of J0116-473).

Concerning the optical spectra of AGN two emission regions are important: The broad-line region (BLR) and the narrow-line region (NLR). Due to its proximity to the central black hole, the BLR can provide useful information on areas next the central energy source of an AGN. The emission lines from material in this area are broaden due to the Doppler shift caused by the fast motion around the black hole. The line widths range from 500 km/s to 10^4 km/s (FWHM). A typical value is 5000 km/s. The mass of the BLR can be obtained from the luminosity of strong emission lines and is related to this luminosity (here the emission line C_{IV} in units of 10^{42} [42]) by $M_{BLR} = 10^{-3} L_{42}(C_{IV}) M_{\odot}$, the fraction of absorbed radiation from the central object by the BLR is of the order of 0.1.

The fluxes from the narrow-line region (NLR) are strongly orientation depended and originate from spatially extended regions within the AGN. The NLR is not spherically symmetric. For radio loud AGN the NLR symmetry axis is the same as the radio-axis. For radio-quiet AGN so-called ionization cones have been observed. These sharply bounded areas contain low-density gas which is ionized by the central source. As for the BLR the NLR is also filled with a clumpy structure of cold gas and dust. The line-width is in the range of 200-900 km/s. The mass of the NLR can deduced from the $H\beta$ -line [42] luminosity and is much higher than for the BLR: $M_{NLR} = 7 \cdot 10^5 L_{41}(H\beta) n_3^{-1} M_{\odot}$,

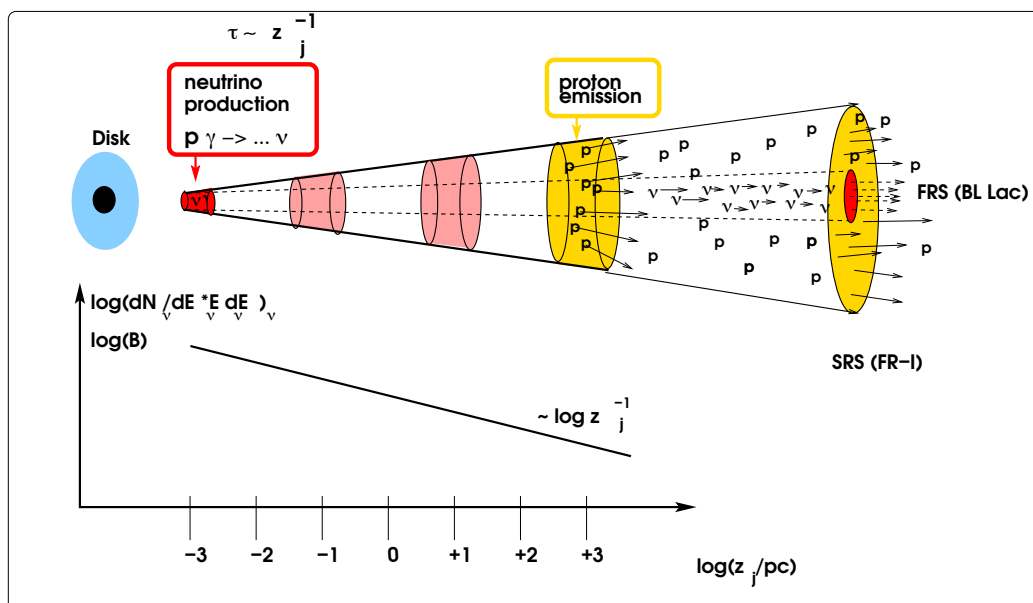


Figure 2.8: Neutrino emission region from an AGN jet near the central black hole. The emission takes place in the first shocks at dense regions, is collimated and can therefore only be observed in BL Lac type objects (figure from [41]).

where n_3 is the electron density in 10^3 cm^{-3} .

For some AGN large jets are formed where often due to relativistic beaming only the approaching jet can be observed and the counter jet is not observable (see figure 2.7). Within these jets it is assumed that particles are accelerated by shocks and give rise to non-thermal emission of radiation. Looking for AGN at a line of sight close to the jet axis (e.g. for Blazars and BL Lacs), the spectrum can be dominated by the emission from the jet although the amount of energy is much lower than the one radiated away in thermal emission by non-jet parts of the AGN. Jets extend on scales much larger than the size of the host galaxy. Although great effort has been made during the last years on observation techniques, it is still under discussion what jets are made of, how the acceleration works in detail, how jets can be collimated over such large distances and if jets are the origin of high energy cosmic rays. Increasing computer power made it possible to give important contributions to the puzzle via simulations. However, this is also a challenging task since relativistic jet simulations need to cover a huge range of scales both in space and time: The jet expands from 100 kpc to 1 Mpc and processes inside of it require the understanding on a scale of the gyro radius of proton and electron at magnetic fields of several Gauss. Jets are also suspected to be an origin of ultra high energy cosmic rays.

The origin of neutrinos from AGN (see figure 2.8) is the decay chain of charged mesons such as pions and kaons. Two processes are important for meson production within AGN from accelerated protons: (a) inelastic pp-scattering and (b) photo-production via dense photon fields ($p\gamma$ interaction, here only the delta-resonance is

2 Neutrino sources

shown):

$$p\gamma \rightarrow \Delta^+ \rightarrow \pi^0 p \rightarrow \text{photons} \quad (2.5)$$

$$\Delta^+ \rightarrow \pi^+ n \rightarrow \mu^+ \nu_\mu n \rightarrow \bar{\nu}_\mu \nu_e \nu_\mu e^+ n, \quad (2.6)$$

where the neutron also decays in neutrinos: $n \rightarrow p + e^- + \bar{\nu}_e$. Basically there are two main regions for neutrino production: (a) The region around the black hole and (b) the ultra-relativistic outflow of the AGN jet. For (a) photo-production of neutrinos is expected since the photon density exceeds the nucleon density by several orders of magnitude in these areas close to the central black hole. Therefore a neutrino beam is expected for BL-Lac type objects, where we look directly into the jet. Due to oscillations the source flavour ratio of $\nu_e : \nu_\mu : \nu_\tau = 1 : 2 : 0$ is converted to $1 : 1 : 1$. For (b) it is assumed that protons are accelerated in plasma shocks within the jet (Fermi acceleration). Again an interaction with ambient photons leads to photo-hadronic meson and therefore neutrino production. Due to large Doppler factors (up to 10) within the jet these mesons are highly boosted in energy. Furthermore AGN can be in different 'states' and show variability in all domains of the electromagnetic spectrum. Also the material outflow within the jets shows high- and low-state periods and is related to the radio emission of the AGN. Possible reasons for AGN flaring are e.g. tidal disruptions of a Sun-like star that passes by close to the supermassive black hole or disc instabilities. For further information refer to [43].

From the above examples it is clear that the observation of high-energy neutrinos from these astrophysical objects is directly connected to hadronic acceleration processes. For this reason the detection of point source signals is a main goal for high-energy neutrino physicists.

3 Neutrino astronomy

In brief:

- Being uncharged and interacting very rarely, neutrinos are the ideal messenger particles from astrophysical sources.
- Due to low cross sections for neutrino interaction, large detection volumes are required for neutrino telescopes.
- Using the Cherenkov light from secondary muons, neutrino directions can be reconstructed in water or ice detectors.
- After several years of gathering experience, two major neutrino telescopes are currently in operation: ANTARES and IceCube.

3.1 The neutrino as a messenger particle

After the discovery of the neutrino physicists started with the detection of low-energy neutrinos and measured successfully MeV neutrinos from the solar fusion processes for example. With growing experimental knowledge, people began to think about high-energy neutrinos as messenger particles for astronomical observations.

Due to its properties, the neutrino is the ideal messenger particle for the observation of astrophysical objects. A neutrino is electrically neutral and therefore not deflected by interstellar magnetic fields (also neutrinos do not decay), while propagating from the source to the Earth. In principle, the measured neutrino direction can be directly associated with the source position. Further, neutrinos have very tiny interaction cross sections. This allows them to escape from dense regions within the universe even before an optical signal is emitted. They are rarely absorbed by interstellar dust. However, the small probability for interaction is at the same time the biggest challenge for neutrino astronomers. Detector volumes have to be extremely large to find a signal at all.

3.2 Neutrino detection principle

The main idea of detecting galactic and extragalactic neutrinos using large scale neutrino telescopes is to look downward through the Earth, as all other particles cannot penetrate it (see figure 3.1). After interaction with the detector medium or the surroundings, the neutrino is converted into the corresponding charged lepton. Therefore,

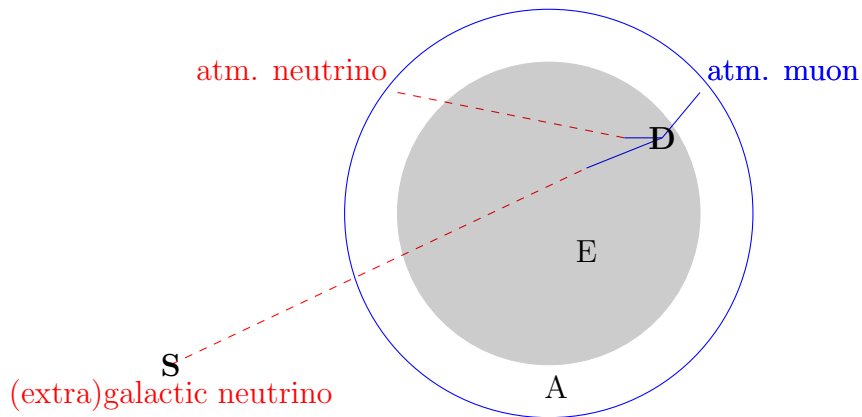


Figure 3.1: Neutrino detection using the Earth (E) as a shield: Neutrinos (red, dashed) from a source (S) can be detected via a charged lepton (blue) traveling through or nearby the detector (D). Signals from atmospheric (atmosphere A) muons or atmospheric neutrinos produce background events.

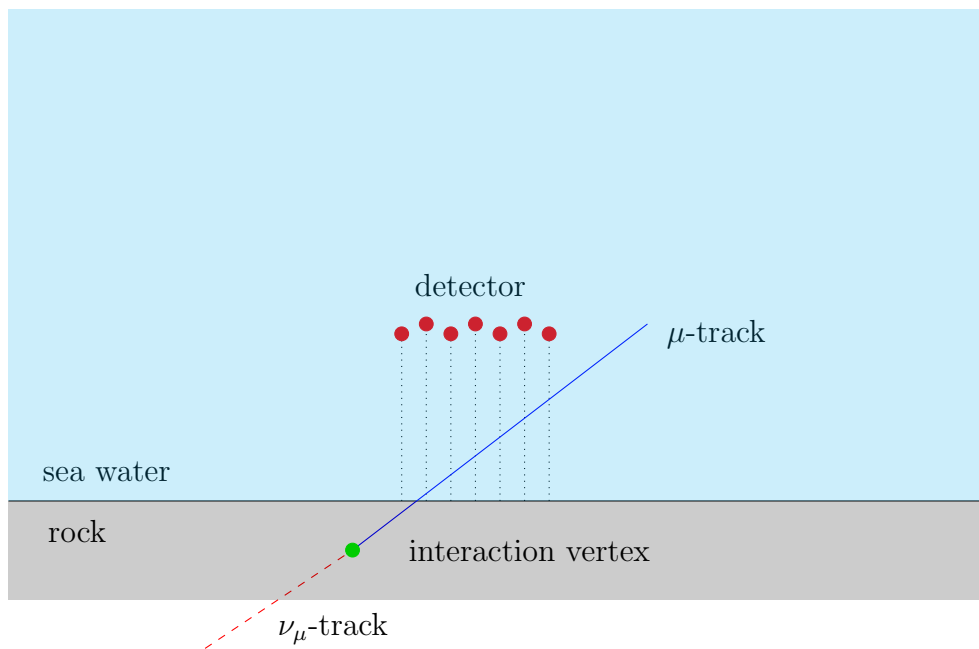


Figure 3.2: After interaction in rock (shown) or sea-water, a neutrino induced muon is traveling upwards through a deep-sea neutrino detector. Depending on the energy, there is a kink between the two tracks.

neutrinos that have crossed the Earth produce upward-going charged lepton tracks in the detector (see figure 3.2). To detect neutrinos, the Cherenkov light of the generated charged lepton traveling through the detection medium is used. In case of muons it is possible to reconstruct their tracks from the arrival times of Cherenkov photons within a 3D-photomultiplier array.

3.3 Experimental signatures from neutrinos

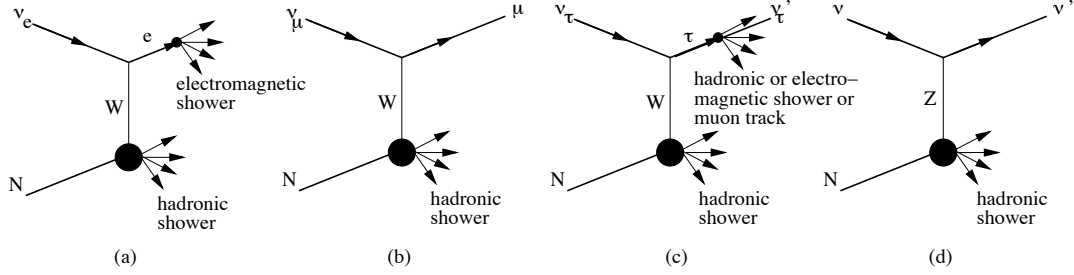


Figure 3.3: Feynman-type diagrams for interactions of ν_e (a), ν_μ (b) and ν_τ (c) via charged-current. Figure (d) shows a neutral-current interaction via Z_0 exchange valid for all neutrino flavours.

The three neutrino flavours produce their individual signatures inside the detector (see figure 3.3):

- Muon neutrinos (ν_μ):

$$\nu_\mu + N \rightarrow \mu^- + X \quad \bar{\nu}_\mu + N \rightarrow \mu^+ + X$$

After a charged-current interaction with protons/neutrons (N) of the surrounding medium (water, rock or ice), the muon neutrino is converted into a muon traveling through the instrumented volume. If the energy is high enough, the emitted Cherenkov light will produce a *track signature* within the 3D-photomultiplier array. At the interaction vertex there will be a hadronic shower. There is an energy dependent kinematic angle between the incoming neutrino and the outgoing muon that limits the angular resolution of such track like events.

- Electron neutrinos (ν_e):

$$\nu_e + N \rightarrow e^- + X \quad \bar{\nu}_e + N \rightarrow e^+ + X$$

High-energy electrons produced in charged-current interactions from electron neutrinos will induce electromagnetic showers. As their longitudinal dimensions do not exceed a few meters, these events give rise to a *pointlike signature* (for further information on shower reconstruction with the ANTARES neutrino telescope see [44, 45]).

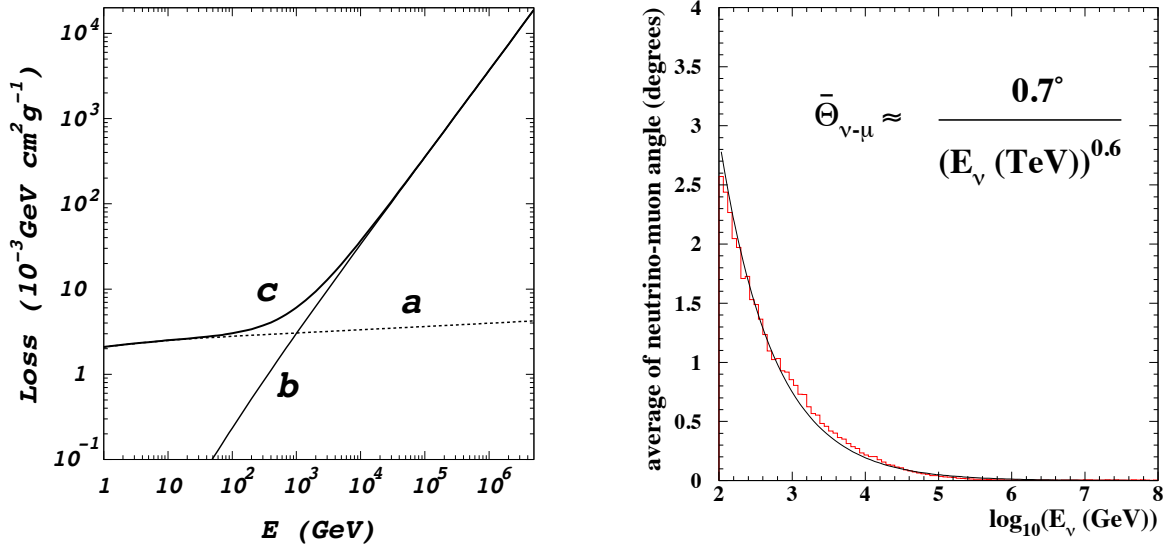
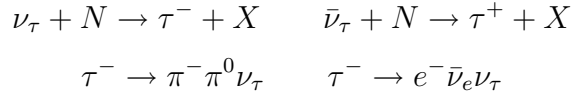


Figure 3.4: *Left*: Muon energy loss in pure water. Ionization (a) is the main component up to 1 TeV. From there radiative processes (b) start to contribute. The overall energy loss is indicated by (c) (figure from [47]). *Right*: Average angle between neutrino and muon direction as a function of energy (figure from [48]).

- Tau neutrinos (ν_τ):



For high energetic tau leptons (lifetime $2.9 \cdot 10^{-13}$ s) created inside the detector volume an interesting event topology can be observed: the primary vertex shower is connected by the tau track to a secondary electromagnetic or hadronic shower (examples for hadronic/leptonic τ^- decays see above). This signature is named *double bang*. For taus created outside the detector only the incoming track and the secondary shower is detected: a so-called *lollipop* signature.

For neutrinos exceeding an energy of 10^6 GeV, the Earth becomes opaque and other techniques like acoustic neutrino detection are proposed [46]. In the next section, the detection of muons is described in detail, which is the most important detection channel for neutrino telescopes.

3.4 Muon propagation and the Cherenkov effect

3.4.1 Muon propagation

During propagation through water, rock or ice a muon loses energy mainly via four processes: ionization, bremsstrahlung, photo-nuclear interaction and pair production.

3.4 Muon propagation and the Cherenkov effect

Losses via ionization are almost constant as a function of muon energy, while radiative losses start to dominate at energies higher than 1 TeV (see figure 3.4 left) [47]. The rate of radiation loss is proportional to its energy. The radiation length for a muon is that of an electron times the factor $(m_\mu/m_e)^2$. Therefore only high-energy muons lose significantly. The resulting ranges for muons are compatible with the dimensions of current neutrino telescopes of several hundreds of metres: a 100 GeV muon travels about 500 m in water.

Three aspects affect the angular resolution of neutrino telescopes as far as the muon track is concerned. There is a kinematic angle between the incident neutrino ν and the produced muon μ . Its energy dependence can be parameterized as follows [48]:

$$\langle \vartheta_{\nu,\mu} \rangle = \frac{0.7^\circ}{(E_\nu[\text{TeV}])^{0.6}}. \quad (3.1)$$

For high energy neutrino events this gives only a tiny contribution to the overall angular resolution (see figure 3.4 right). There is a distortion of the primary muon track due to multiple scattering in the surrounding medium (path length x , radiation length X_0) which is given by

$$\vartheta_{\text{scat}} = \frac{13.6 \text{ MeV}}{E_\mu} \sqrt{x/X_0} (1 + 0.0038 \ln x/X_0). \quad (3.2)$$

This effect is even smaller than the kinematic angle. The third effect is the angular uncertainty of the muon measurement and reconstruction. This topic is covered later in the point source section (see chapter 6).

3.4.2 The Cherenkov effect and light propagation in water

Particles that transverse a medium with a velocity $v > c_{\text{medium}}$ emit so-called Cherenkov light. The angle of emission θ_c (for illustration see figure 3.5) in a medium with refractive index n is given by

$$\cos \theta_c = \frac{1}{n\beta}. \quad (3.3)$$

For muons in sea water ($n \approx 1.35$ at 450 nm, $\beta \approx 1$) this angle is typically around 42° . The threshold energy ($\beta > 1/n$) for a muon with $mc^2 = 106 \text{ MeV}$ is at

$$E_{\text{kin},\mu} = (\gamma - 1)mc^2 = \left(\frac{1}{\sqrt{1 - (1/n)^2}} - 1 \right) mc^2 = 51.8 \text{ MeV} \quad (3.4)$$

For an ANTARES-type photomultiplier, being most sensitive in a wavelength band from 300-600 nm, about 35000 photons are produced per meter for a particle with $z = 1$. The number dN of photons emitted per path length dx and wavelength $d\lambda$ is

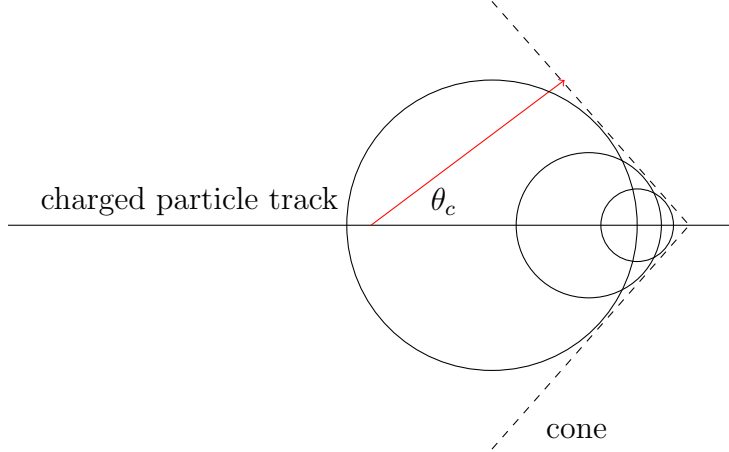


Figure 3.5: Schematic view of the Cherenkov effect. In analogy to a supersonic bang, the positive interference of electromagnetic waves produced along the particle track forms a cone (dashed line). Cherenkov photons (red solid line) are emitted at θ_c .

$$\frac{dN}{dx d\lambda} = 2\pi\alpha z^2 \left(1 - \frac{1}{\beta^2 n^2}\right). \quad (3.5)$$

Using equation 3.3 the number dN of photons (isotropic emission in azimuth around the particle track) produced by a charged particle (charge ze) per path element dx for a wavelength band $[\lambda_1, \lambda_2]$ is given by the FRANK-TAMM-equation:

$$\frac{dN}{dx} = 2\pi\alpha z^2 \frac{\lambda_2 - \lambda_1}{\lambda_1 \lambda_2} \sin^2 \theta_c. \quad (3.6)$$

Therefore, the energy loss by Cherenkov light emission of the particle is almost independent of its energy.

As Cherenkov light is used, detected metres away from the muon track, in order to find the orientation of the track, it is necessary to understand the light propagation within seawater/ice at the detector site [49]. Light propagation is characterized by absorption (absorption length λ_a) and scattering (scattering length λ_s). A widely used measurement for the absorption length of water is the one by Smith&Baker [50]. As recent measurement by Pope&Fry [51] have shown, the result is highly dependent on the water purification and other experimental conditions. For scattering two contributions have to be mentioned: (1) Mie scattering and (2) Rayleigh scattering. The intensity of the emitted light decreases as

$$I(r) = \frac{I_0}{r} e^{-\frac{r}{\lambda_{\text{att}}}}. \quad (3.7)$$

λ_{att} is the attenuation length [52] and $1/\lambda_{\text{att}} = 1/\lambda_s + 1/\lambda_a$. For further measurements and theoretical aspects of light propagation in sea water see [53] and references therein.

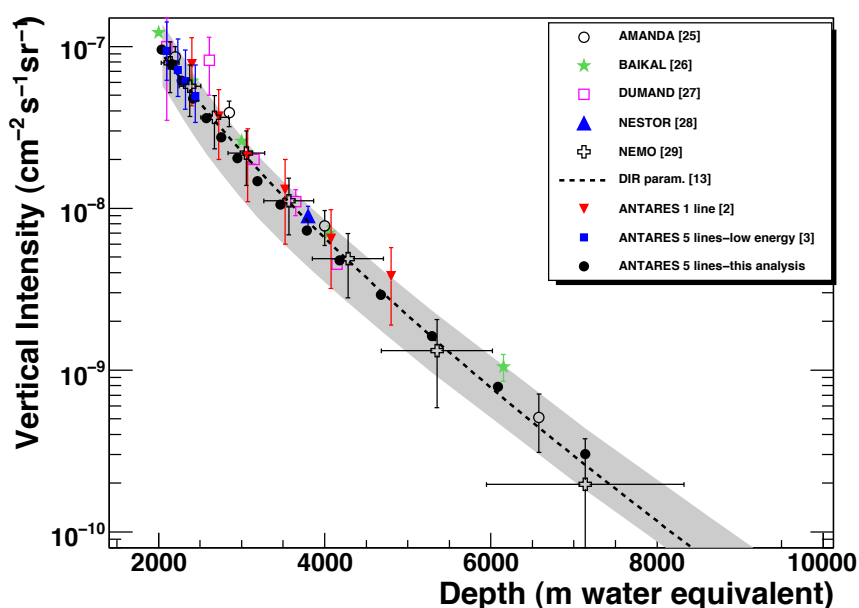


Figure 3.6: Depth intensity relation: vertical atmospheric muon flux as a function of slant depth measured with the ANTARES detector. Expectations from Bugaev parameterization (dashed line) are shown as well as results from other experiments (figure from [54]).

3.5 Background for undersea neutrino detection

The search for cosmic or extragalactic neutrinos is not free of background. Particles transversing the detector (mainly muons), bioluminescence light and light from ^{40}K -decays naturally contained in sea water can mimic the presence of a signal event.

3.5.1 Particle background

On the level of particles, both, neutrinos and muons, originating from interaction of primary cosmic rays with the Earth's atmosphere, need to be considered. An irreducible background for all neutrino telescopes are atmospheric neutrinos coming from the other side of the Earth. Further, the signal muons (from a extraterrestrial neutrino) have to be separated from the large number of atmospheric muons traveling downward through the detector volume and are misreconstructed as upward-going. In order to reduce this background from the view of construction, neutrino telescopes are installed at a large depth. The dependence of the muon flux as a function of depth (metre water equivalent), the so-called depth intensity relation [54], measured by ANTARES can be seen in figure 3.6. At the ANTARES depth the flux of atmospheric muons exceeds that of atmospheric neutrinos by six orders of magnitude.

3.5.2 Optical background

For seawater based detectors another challenge has to be faced. At these sites one can find two main sources of optical background:

- Bioluminescence light.
- ^{40}K -radioactivity:
 - Cherenkov light from electrons produced in ^{40}K -decays (solved in sea water):
 $^{40}\text{K} \rightarrow ^{40}\text{Ca} + e^- + \bar{\nu}_e$ (BR 89.3 %).
 - γ emission from electron capture of ^{40}K (BR 10.6 %).

Occurrence of bioluminescence light (90% of the deep sea animals produce it) strongly depends on the strength of the sea current and other environmental conditions. It is supposed that these animals produce light in particular, when clashing with the detector infrastructure or by getting in turbulent currents caused by detector components. From data of the ANTARES neutrino telescope one knows that this results on average in 60-70 kHz background rate (baseline). This baseline can vary up to several 100 kHz on longer timescales. On short timescales bursts with a hit rate in the MHz range are observed. The bioluminescence burst rate is proportional to the sea current velocity as can be seen from figure 3.7.

Cherenkov light from ^{40}K -decays in seawater produces an additional 30 kHz PMT single rate (from simulations). As the ^{40}K -concentration in sea water is almost constant in time, ^{40}K -decays can be used to monitor the PMT-gain by observing the local coincidence rate of two adjacent PMTs (see figure 3.8) and to check time calibration parameters. Fortunately, photons from these processes are uncorrelated single photons that can be filtered out by a suitable trigger.

3.6 Previous and current neutrino telescopes

Several neutrino telescopes have been developed and operated successfully within the last years. This section gives a short overview of previous and still ongoing projects.

DUMAND. The DUMAND project [56] (Deep Underwater Muon And Neutrino Detector Project) started in 1976 at a depth of 4800 m off the shore of the island of Hawaii. After many years of R&D effort the project was cancelled in 1995 due to technical and funding problems. Nevertheless, major experience and technical know-how obtained in DUMAND were later used in the Mediterranean projects.

Lake Baikal. Up to present the Lake Baikal Deep Underwater Neutrino telescope [57, 58] probes the feasibility of underwater neutrino detection. The NT-200 setup

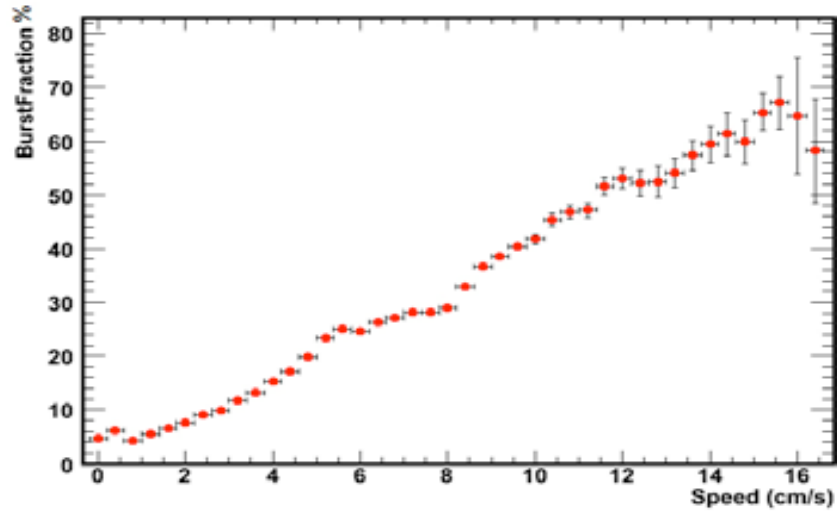


Figure 3.7: Burst fraction (time fraction where the rates exceed 120% of the normal baseline rate) as function of sea current velocity, a clear correlation is found.

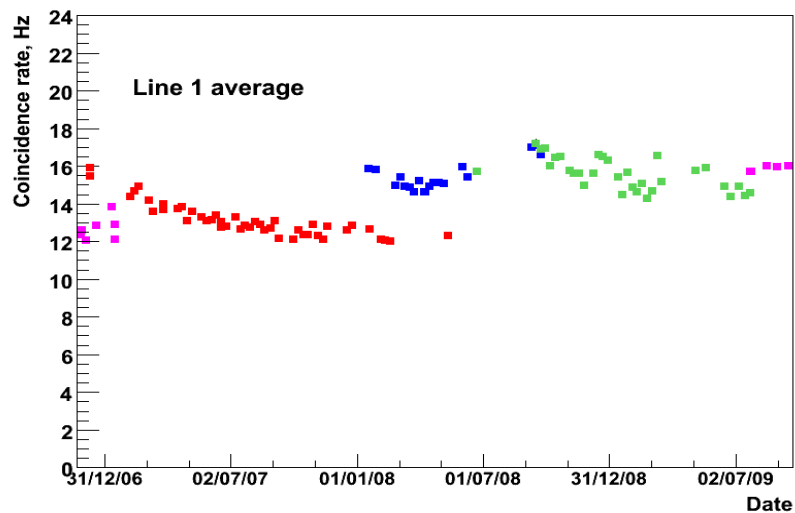


Figure 3.8: ^{40}K coincidence rate of Line 1 as function of time. The negative slope shows a decreasing PMT gain and is compensated by HV tuning (different colours indicate periods with no HV tuning).

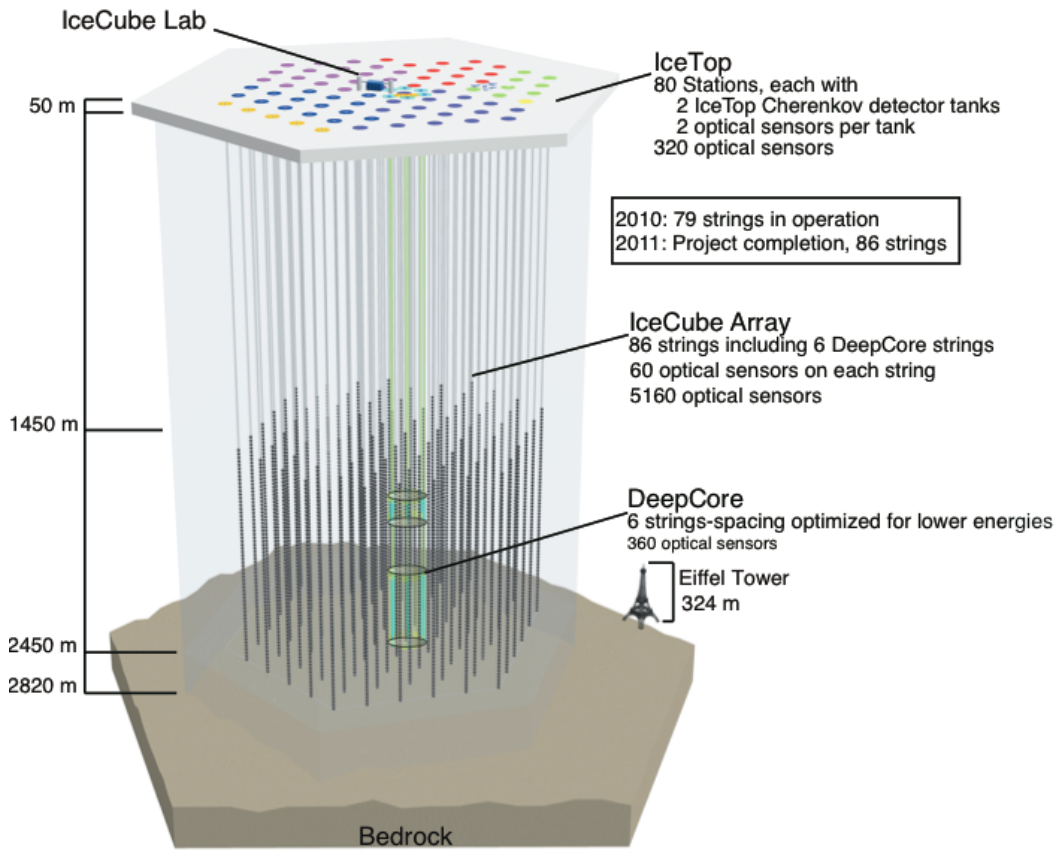


Figure 3.9: Drawing of the IceCube detector including IceTop, DeepCore and the precursor AMANDA (figure from [55]).

contained 192 PMTs on 18 strings, which was updated in 2005 by adding three additional strings with 36 PMTs each. Lake Baikal offers several advantages for such an experiment: low ^{40}K background and the possibility to maintain the detector from the frozen surface. Of course, the low water depth results in high contamination from atmospheric muons during data taking. Further, the short absorption length of only 20 m is another problem for this setup.

NEMO, NESTOR. The Italian project NEMO (Neutrino Mediterranean Observatory) [59–61] has chosen a site 80 km south-east of Capo Passero (Sicily) at a depth of 3350 m. In 2006, the NEMO group developed a self unfolding tower structure for future cubic kilometre telescopes in the sea. The NESTOR (Neutrino Extended Submarine Telescope with Oceanographic Research) collaboration successfully deployed their first PMTs in March 2003 at a depth of 4000 m off the coast of Pylos (Greece).

AMANDA. The first in-ice detector at the South Pole AMANDA [62] (Antarctic Muon And Neutrino Detection Array) took data from 1995 to early 2009. In its final

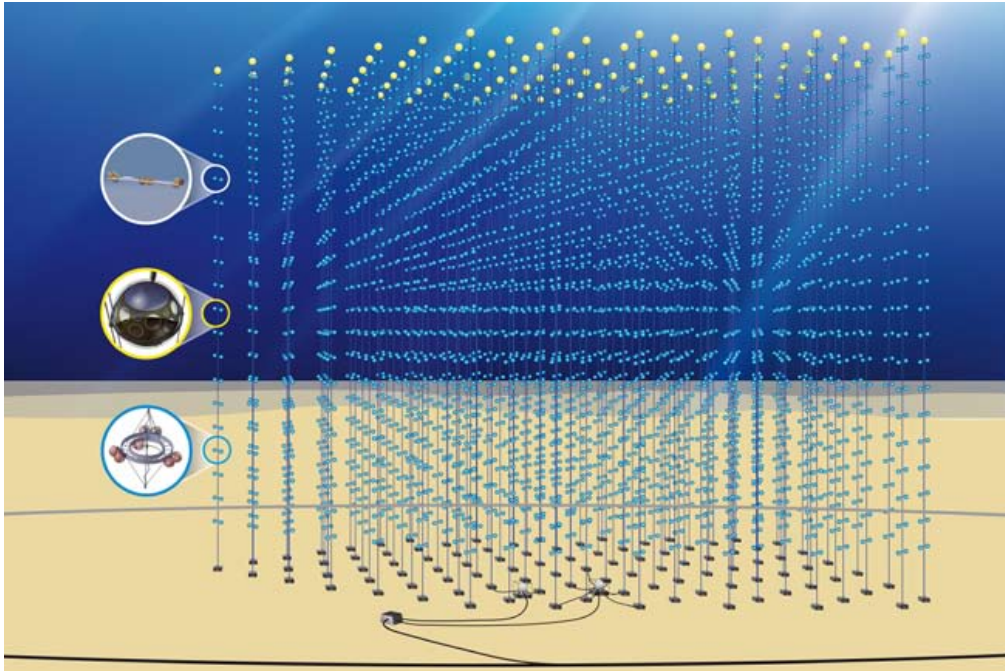


Figure 3.10: Artist's view of the KM3NeT detector to be built in the Mediterranean Sea. Three storey options are shown (figure from KM3NeT-TDR, see text for reference). The instrumented volume is in the order of km^3 .

configuration (AMANDA-II, 2000) it consisted of 677 PMTs on 19 strings. These strings have been deployed in the ice up to a depth of 2350 m.

IceCube. Located at the South Pole, IceCube [55, 63] has been completed in 2011 comprising 4800 PMTs on 80 strings installed in the ice (see figure 3.9). For low-energy events a more densely instrumented volume in the center, called DeepCore, has been installed. On the surface the air shower array IceTop provides a veto for atmospheric muons. So far, no point sources of neutrinos have been observed with this instrument.

ANTARES. As this thesis is based on studies concerning the ANTARES neutrino telescope, detail information can be found in the next section.

KM3NeT. This European infrastructure [64, 65] will combine a deep-sea neutrino telescope of several cubic kilometre size in the Mediterranean sea and an interface for earth and sea science long-term experiments. As a joined effort of ANTARES, NEMO and NESTOR several layouts and techniques have been evaluated and tested successfully. Located on the Northern Hemisphere, this telescope can complement IceCube's sky coverage. An artist's view is shown in figure 3.10. The technical design report can be downloaded from

<http://www.km3net.org/KM3NeT-TDR.pdf>.

4 The ANTARES neutrino telescope

In brief:

- The ANTARES water Cherenkov telescope is made up of 12+1 vertical sub-sea lines carrying 885 photomultipliers in total. Besides the optical part, hydrophones for feasibility studies for acoustic particle detection are implemented on two lines.
- Each standard ANTARES line carries 25 storeys. A storey is made out of three photomultipliers and the corresponding electronics container.
- After transmission to shore, several trigger algorithms are applied to the data stream. Events matching various trigger criteria are stored on disk using the ROOT-format.
- To find track signatures from a time-pattern of hits on several photomultipliers, the relative timing needs to be calibrated up to nanosecond scale. Further, the photomultiplier positions need to be known with centimeter precision.

4.1 Detector layout

The ANTARES (Astronomy with a Neutrino Telescope and Abyss environmental Research) neutrino telescope [48, 66–68], located in the Mediterranean Sea, is the world’s only deep-sea Cherenkov telescope. The detector was completed in May 2008 after several years of construction, assembling and deployment and consists of 885 10-inch-photomultiplier (Hamamatsu, R7081-20 type [69]) tubes implemented in pressure resistant glass spheres. 75 of these so-called Optical Modules (OMs), looking downwards at 45° from the vertical, are mounted in groups of three, called storeys, on a roughly 500 m long flexible string, called line, with a vertical spacing of 14.5 m. The first storey of each line is mounted about 100 m above the sea floor. In total, twelve lines and one additional instrumentation line (IL) are fixed by anchors on the abyssal plane near Toulon/France at a depth of ≈ 2475 m and straightened by a submersed buoy on top (see figures 4.1, 4.2, 4.3). The inter-line spacing is about 70 m. The IL carries environmental probes such as salinity and conductivity detectors [66] and parts of the prototype detector for acoustic neutrino detection [46]. Also a triggered infra-red camera records light bursts from bioluminescent organisms [70]. In detail, an ANTARES line is composed as follows (from bottom to top):

4 The ANTARES neutrino telescope



Figure 4.1: Geographical location of the ANTARES detector (A) in the Mediterranean Sea. The depth of the sea floor is visualized and the abyssal plane is clearly visible (figure from Google Maps).

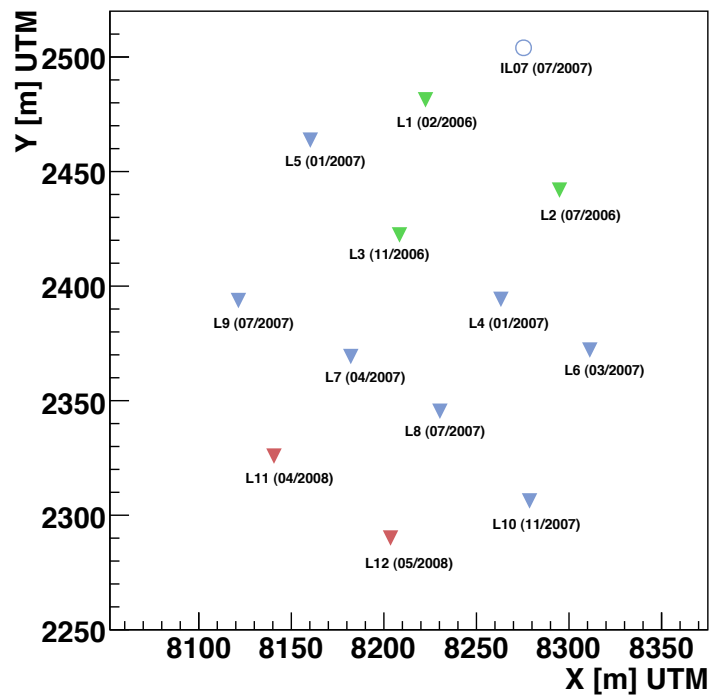


Figure 4.2: Seabed layout (UTM coordinates, see section 5.2) and deployment date (month/year, green: 2006, blue: 2007, red: 2008) of the twelve ANTARES lines (triangles) and the additional instrumentation line (IL07, circle).

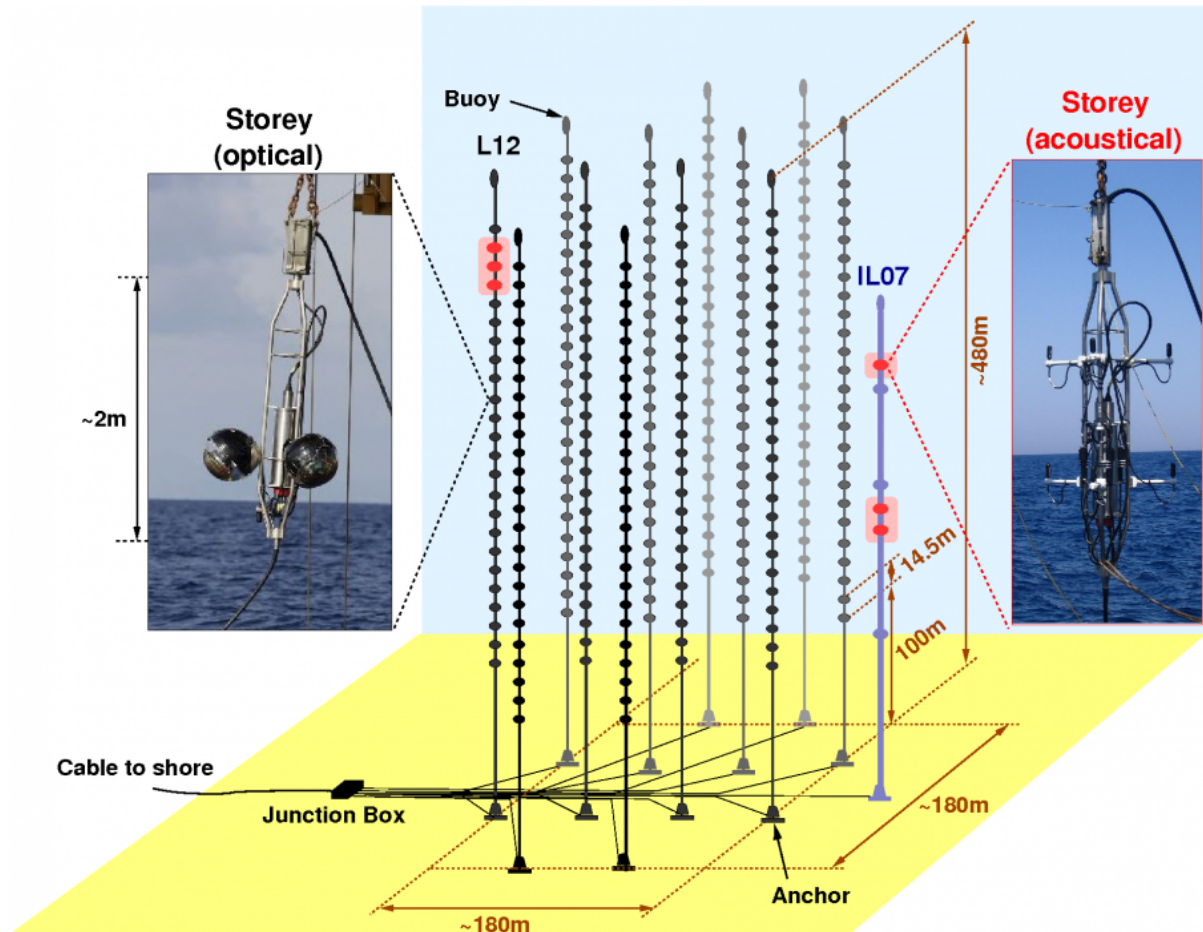


Figure 4.3: Schematic view of the ANTARES detector indicating both optical (full black circles) as well as acoustic storeys (full red circles, on Line 12 and instrumentation line (IL07)). A picture of each type of storey taken during deployment is also shown (figure from ANTARES internal pages).



Figure 4.4: Drawing of an ANTARES storey. The three Optical Modules, the electronics cylinder (grey), the LED-beacon (blue) and the hydrophone (ochre) for acoustic positioning are visible (figure from ANTARES internal pages).

- *Bottom String Socket*: The Bottom String Socket (BSS) is the connection between the line and a dead weight which fixes the whole unit on the seabed (for seabed layout see figure 4.2). For maintenance, this connection can be released remotely from a ship and the line can be recovered at the surface (ascent speed 1 m/s). The BSS also carries a hydrophone (RxTx-)module of the acoustic positioning system for both sending and receiving acoustic signals and communication electronics.
- *Cable*: The electro-optical-mechanical cable has been designed to provide the 14.5 m long mechanical connection between two adjacent storeys and to enclose the optical fibers for signal transport (21 single-mode fibers for data transmission, slow control, clock distribution and trigger readout request signal) as well as nine copper wires for power distribution.
- *Storey*: The titanium frame of an ANTARES storey carries three Optical Modules, a (Master)Local Control Module and additional devices for calibration (see figure 4.4).
 - *OM/PMT*: The Optical Module consists of a pressure resistant glass sphere and houses a 10'' Hamamatsu R7081-20 type photomultiplier (PMT) [71]. The equipment for power supply and read-out electronics is not implemented inside the Optical Module, but can be found in the LCM (see next item). Results on sedimentation and fouling in the deep sea environment

can be found in [72].

- *(M)LCM*: The Local Control Module (LCM) is the main electronic container on each storey, where the PMT output is digitized by the Analog Ring Sampler (ARS). Every fifth storey (five sectors per line), a Master Local Control Module (MLCM) replacing the LCM multiplexes the signal and sends it to the String Control Module (SCM) at the bottom of each line.
- *Optical Beacons*: Each line is equipped with four LED Optical Beacons (LOB) placed at storey 2, 9, 15 and 21 in order to illuminate the OMs located above on the same line for time calibration issues [73] (see figure 4.4). The LOB is made of 36 blue LEDs arranged in groups of six times six on vertical boards, which are placed side by side forming an hexagon.
- *Hydrophones*: At storey 1, 8, 14, 20 and 25 a receiver hydrophone is mounted on a lever for acoustic positioning (see figure 4.4).
- *Acoustic storeys*: Line 12 and the instrumentation line carry so-called acoustic storeys (see figure 4.3). They are equipped either with custom built hydrophones and devices designed and manufactured by the Erlangen group. This acoustic neutrino detection test system called AMADEUS (ANTARES Modules for the Acoustic Detection Under the Sea) probes the feasibility of acoustic underwater neutrino detection (from the thermo-acoustic model [74] a bipolar pressure pulse is expected) at energies exceeding 100 PeV [46].
- *Buoy*: At the top of each standard ANTARES line a buoy (maximum operation depth 2500 m, density 0.5 g/cm^3 , [75]) made of composite syntactic foam is mounted. With buoyancies in the order of 7000 N the lines are kept taut under water. The buoyancies have been measured by the manufacturer and are expected to be constant with operation depth. The exact numerical values for each line can be found in section 5.5.

For power supply and data transmission the lines are connected to a central junction box (JB) via interlink cables. The JB is itself connected via the 40 km long Main-Electro-Optical-Cable (MEOC) to an onshore power hut. For further details on ANTARES hardware see [76].

4.2 Data acquisition and triggers

For ANTARES the “all-data-to-shore” concept has been chosen. The data acquisition (DAQ) [77] splits into three main parts: (a) digitize the analogue PMT signal and send it to shore, (b) process the data stream online and generate physics events by applying dedicated filters and triggers. (c) store the information in an appropriate data format for further physics analyses.

Each Optical Module uses two custom built Analogue Ring Samplers (ARS) to record the PMT output signal and digitize it [78, 79]. They are operating in a token-

ring mode (see section on time calibration below) to minimize the efficiency loss in data taking due to the dead time of about 200 ns of each ARS. The combined digitized information of charge and time is called a hit (SPE mode). Further, the ARS can be operated in a waveform mode, where the whole pulse shape is recorded. In a time window of 104 ms (called data frame) the ARS data is collected and buffered inside the LCM via a field programmable gate array in a 64 MB memory. A Motorola MPC860P CPU runs a real time operating system for data processing. Several further processes handle the DAQ and the Slow Control, that manage the data streams from monitoring and calibration devices. From each LCM the data is sent via the MLCMs, the BSS and the JB to the shore station. For ANTARES all hits larger than typically 0.3 photoelectrons (L0 hits) are transmitted to shore.

Onshore, several filters and triggers are applied to the data stream by use of a LINUX PC-farm. The standard trigger is based on causality between different hits (t_i denotes the time of a hit at position x_i , n the refractive index of water):

$$|t_i - t_j| \leq |x_i - x_j|n/c. \quad (4.1)$$

So-called L1 hits are used as an input, which are based on high amplitudes (a single hit of at least three photoelectrons on a single PMT) or a local coincidence between adjacent PMTs within 20 ns. Each trigger setup is then made of special combinations of L1-hits (mostly at least 4-5). If a hit topology has fired a certain trigger, the hits are recorded as a physics event, besides the L1 hits also L0 hits in a time window of $\pm 2.2 \mu s$ are stored. Further, special directional triggers (for example a galactic center trigger) and triggers for optical follow up observations [80] are applied to the data stream. The trigger rate is dominated by down-going atmospheric muons and optical background from bioluminescence and is usually in the range of 5-10 Hz. The data is finally written to ROOT-files [81] and transferred to a computing centre near Lyon over night for long term storage.

ANTARES also receives two external triggers: The GCN network [82] provides a trigger for gamma ray burst detection, the SNEWS network [83] for supernovae detection. In both cases all buffered data are written to disk for a later analysis.

4.3 Time and charge calibration

In principle, three main calibration issues need to be covered for ANTARES: Time, charge and position calibration. The first two are described below. Position calibration is presented separately in chapter 5.

4.3.1 Time calibration

In order to reconstruct muon tracks from timestamped hits with an angular resolution of a few tenths of a degree, a precise relative timing of the hits used is mandatory [84]. Chromatic dispersion (1.5 ns for a 40 m light path) [49] and the transit time spread of the PMT (1.3 ns RMS) limit the precision of timestamping of individual

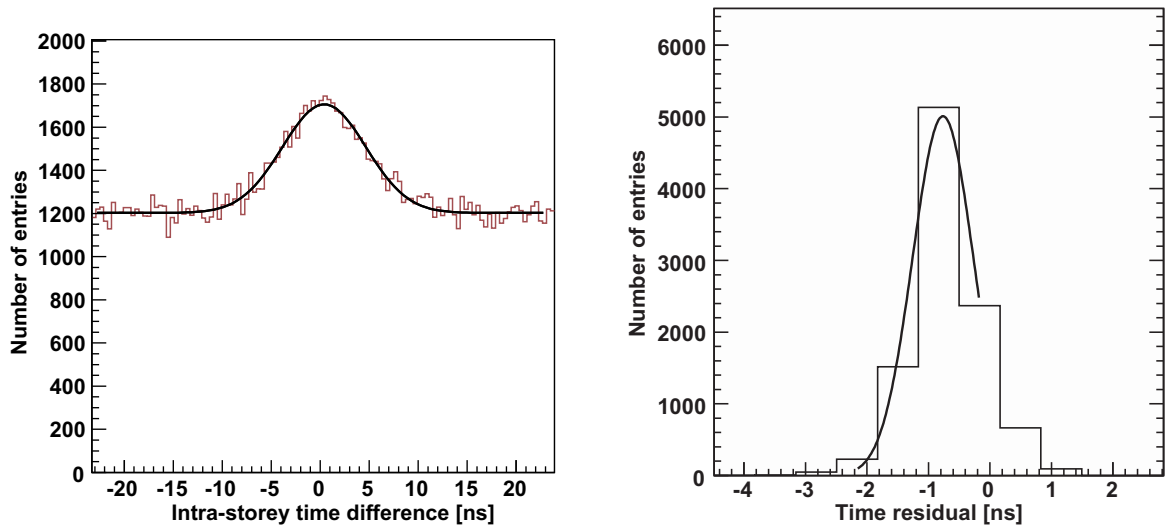


Figure 4.5: *Left:* ^{40}K -events: distribution of hit time differences for a given pair of OMs on the same storey. The fit (solid line) is composed of a flat distribution (random coincidences) and a Gaussian peak. The peak is well centered around zero and therefore shows the time calibration constants for this OM pair to be correct. *Right:* Time residuals of pulses of an OM two floors above an LED optical beacon. The Gaussian fit has a sigma of 0.5 ns. In order to neglect scattered light arriving late at the PMT, the fit is restricted to the photons arriving first (figures from [84]).

hits. The contribution to timing uncertainties from the front-end electronics therefore was designed to be less than 0.5 ns. The absolute timing of an event is less crucial. In order to correlate events with astronomical phenomena a resolution of a few seconds is sufficient. This is achieved by connecting the DAQ to a GPS card providing an absolute timestamp for each run (100 ns accuracy) and therefore for each event within a run. An internal 20 MHz clock is used for a synchronous readout of the PMT signals. This clock signal is generated onshore and received by a dedicated card within the LCM.

The PMT transit time is measured in situ using an internal LED which is implemented at the back side of the PMT inside the OM (peak wavelength 470 nm). Further, the individual time offsets of the OMs are regularly measured in situ using LED (for intra-line calibration) and laser beacons (for inter-line calibration). Figure 4.5 right shows the time residuals for an OM two floors above a LED-beacon. The Gaussian peak with a width of 0.5 ns has been shifted by the light travel time for ~ 30 m. The remaining offset of ~ 1 ns can be explained by the “early photon effect” [85]. The detection of coincident photons from the β -decay of ^{40}K provides an additional and independent check of these offsets (see figure 4.5 left).

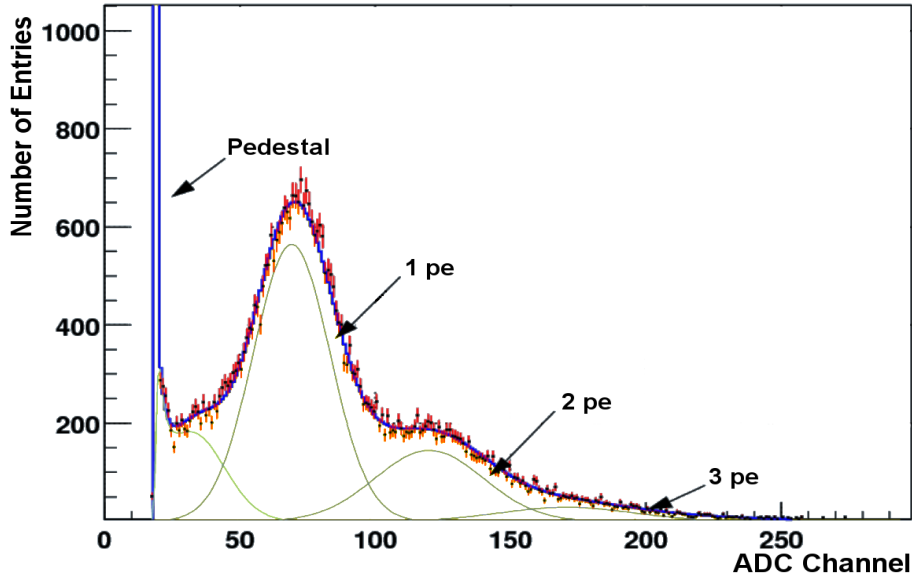


Figure 4.6: Charge measurement from a laboratory test setup: Number of entries in each ADC channel. The pedestal and the photoelectron peaks are clearly visible. The individual components (ochre curves) sum up to the blue curve (figure from [86]).

4.3.2 Charge calibration

The goal of charge calibration is quantifying the PMT-signal in photoelectron units by measuring the PMT response to a single photoelectron (PE) [87]. With this information one can then calculate the number of PEs that caused a given PMT signal. As for time information, the charge is also obtained via the ARS that integrates the PMT output signal for 25 ns and subsequently digitizes the information.

Mainly two parameters need to be known for each ARS: The pedestal, which corresponds to the dark current of the PMT, and the photoelectron peak. The pedestal is obtained during special calibration runs. The photoelectron peak can be extracted from minimum bias events which produce single photonselectrons at the photocathode. For this minimum bias data where higher order photoelectron peaks can be neglected the probability distribution P (x in ADC units) is fitted by

$$P(x) = C_1 e^{-\alpha(x-x_{th})} + C_2 e^{-\frac{(x-x_{pe})^2}{2\sigma^2}} \quad (4.2)$$

where x_{th} is the effective threshold. The first part describes the pedestal, while the second part is the Gaussian photoelectron peak distribution (mean x_{pe}). The position of the pedestal and the one-photoelectron-peak are then used to convert the PMT output signal into photoelectron units (see figure 4.6). To do this correctly one has to take into account the “cross-talk effect”: The charge measurement is influenced by the time measurement due to cross talk of the capacitors within the ARS. The cross talk

4.3 Time and charge calibration

effect has a linear behavior and amounts up to 0.2 photoelectron-units. It is measured for each ARS within the detector and taken into account during hit calibration. The inverse effect (i.e. time measurement is affected by charge measurement) has not been observed.

4 *The ANTARES neutrino telescope*

5 The alignment of ANTARES

In brief:

- At the site of ANTARES the underwater sea current has a velocity of several cm/s.
- Since the detector consists of flexible lines, the detector geometry is time dependent.
- Using data from local tiltmeters and compasses and an acoustic positioning system, one can reconstruct the detector geometry with a two minute sampling.
- The validity of this technique has been proven by two further independent ANTARES measurements.

As has been described in section 4.1, the ANTARES detector is not a rigid structure but is continuously changing its geometry under the influence of underwater sea currents; furthermore the storeys along the line can rotate around their axis of symmetry. For the reconstruction of muon tracks from the time and position information of photomultiplier hits, the positions of the latter need to be known with a reasonable time sampling and an accuracy of several centimetres. In this section the modeling of the shape of the lines, the required software development and the performance of the ANTARES relative positioning system is described. For information on the absolute positioning of the telescope refer to [1, 88].

5.1 The sea at the ANTARES site

The ANTARES detector is located about 40 km offshore on an abyssal plane in the Mediterranean Sea. The water depth at the ANTARES site is about 2475 m. The temperature at the site is nearly constant at around 13 °C. As can be seen in figures 5.1 and 5.2 there is a time-dependent underwater sea current of several centimetres per second. Most of the time its magnitude is below 15 cm/s. Nevertheless, currents above 20 cm/s have been observed. Furthermore, there is a preferred East-to-West direction of the current in agreement with the direction of the Ligurian sea current (“Northern Current”) [89, 90]. Due to the Coriolis force the current shows a periodic structure with a period length of $T = T_{\text{sidereal}} \cdot \sin \varphi \approx 16.3 \text{ h}$, where φ is the latitude of the ANTARES site.

5 The alignment of ANTARES

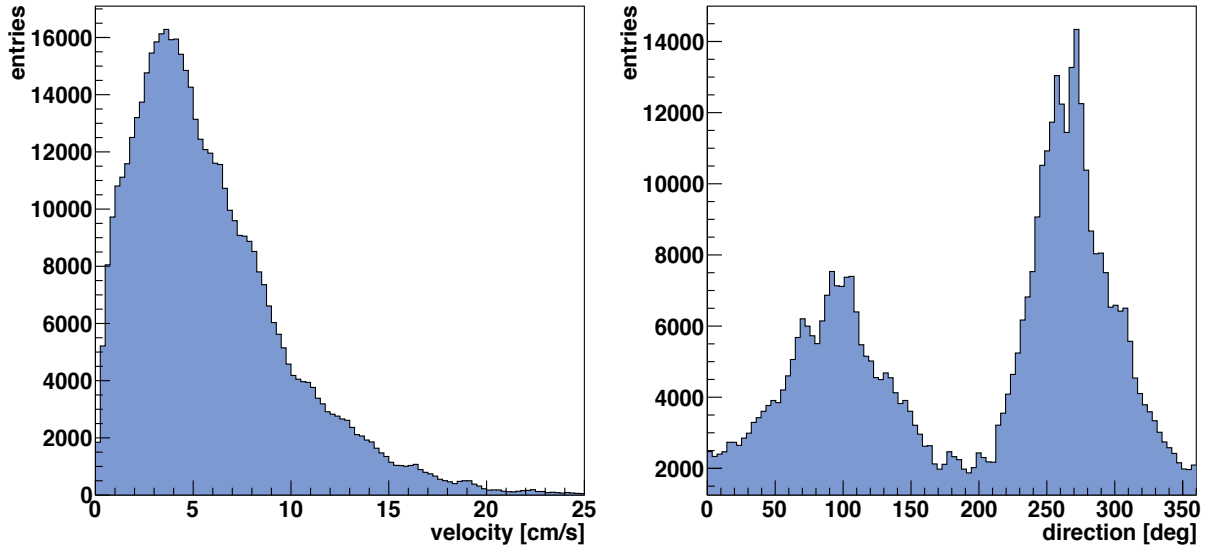


Figure 5.1: Sea current parameters measured by an acoustic doppler current profiler (ADCP) on the instrumentation line: The data have been taken in the year 2009, predominantly during standard operation of the neutrino telescope. *Left:* Histogram of sea current velocity (mean = 5.86 cm/s, RMS = 3.94 cm/s). *Right:* Histogram of sea current direction (0° corresponds to North, 90° to East).

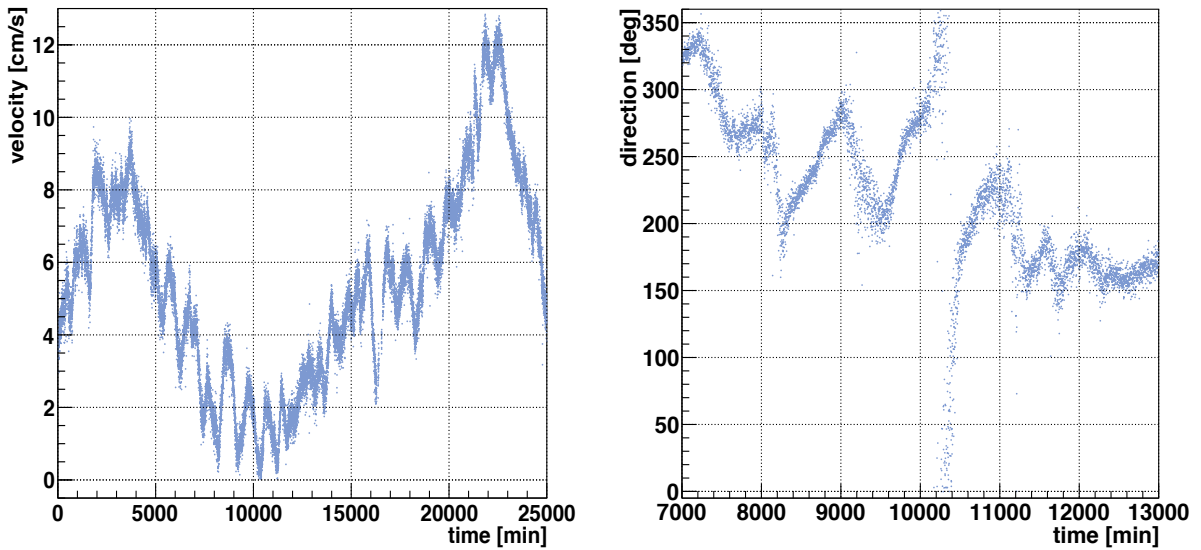


Figure 5.2: *Left:* Sea current velocity versus time. Shown data are taken starting July 2010. The velocity shows a periodicity of about 16 hours due to the Coriolis force. *Right:* Sea current direction versus time (same time reference as in left plot).

5.2 Coordinate systems

Two kinds of coordinate systems are used to generate and save positioning data of the telescope: A global coordinate system based on the UTM-grid (see below) and a local one fixed by the hardware that measures tilts and headings for each storey.

Global coordinate system

ANTARES is located at $42^\circ 48'$ N, $6^\circ 10'$ E. For absolute positioning the UTM-grid is used (Universal Transvers Mercator [91], based on WGS84, for illustration see [92]). The ANTARES site is close to the west bound of zone 32T. The BSS of Line 6, for example, has the coordinates (UTM coordinates in capital letters):

$$X = 8311.6 \text{ m} \quad Y = 2371.4 \text{ m} \quad Z = -2477.4 \text{ m}.$$

Depending on the zone number, there is a convergence angle which measures the deviation of the grid north with respect to the magnetic north direction. For zone 32T it is 1.9258° . The UTM-scale factor of $s = 1.00026$ which measures the length distortion is reduced by the scale factor \tilde{s} introduced at the centre of gravity of the instrumented volume (approx. depth $d = 2200$ m below sea level):

$$\tilde{s} = 1 - \frac{d}{R_{\text{Earth}}} = 1 - 0.34 \cdot 10^{-3} \Rightarrow s \cdot \tilde{s} \approx 1. \quad (5.1)$$

Further the grid-north h_{grid} and the magnetic north direction h_{mag} are connected via magnetic declination (deviation of magnetic and geographic north direction) and convergence angle as follows:

$$h_{\text{grid}} = h_{\text{mag}} + 1.9258^\circ_{\text{con}} + \text{dec}(y). \quad (5.2)$$

The magnetic declination changes by 0.117° per year. This feature is taken into account using a linear correction (per year y): $\text{dec}(y) = 0.483^\circ + 0.117^\circ \cdot (y - 2007)$ [93].

Local storey coordinate system

A local coordinate system fixed to each storey is defined by x , y and z -axis and angles ϑ_x , ϑ_y and ϕ . The OMs of a storey are labeled OM \emptyset , OM1, OM2. The compass-card within the electronic cylinder, that measures the tilt angles and the heading is mounted in such a way, that the following orientation of OM \emptyset is valid (see figure 5.3):

- $B_x = 0, B_y = B_0$: OM \emptyset \rightarrow (magnetic) West
- $B_x = 0, B_y = -B_0$: OM \emptyset \rightarrow (magnetic) East
- $B_x = B_0, B_y = 0$: OM \emptyset \rightarrow (magnetic) North
- $B_x = -B_0, B_y = 0$: OM \emptyset \rightarrow (magnetic) South

5 The alignment of ANTARES

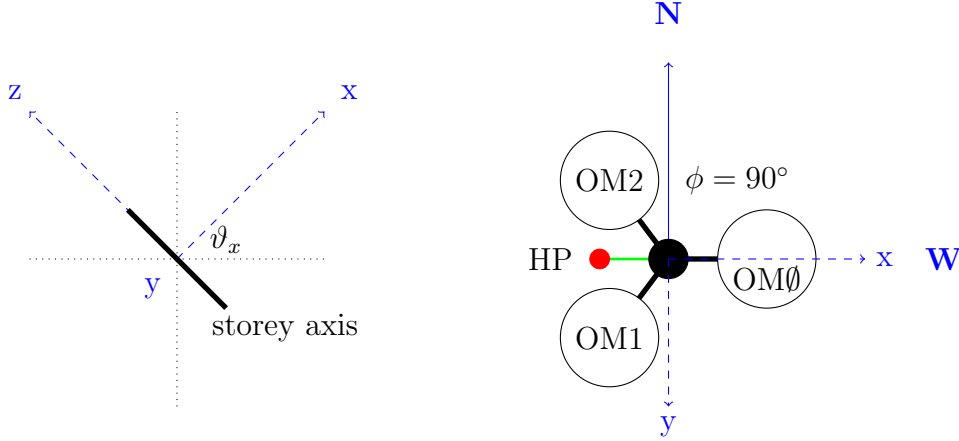


Figure 5.3: Storey orientation and angle definitions. *Left:* Pitch = $\vartheta_x > 0$ (rotation around y -axis). *Right:* This configuration (OM \emptyset \rightarrow W) corresponds to a heading of $+90^\circ$. The hydrophone (HP) for acoustic positioning is mounted on a 0.293 m long arm (green) opposite to OM \emptyset .

B_x and B_y are the two horizontal components of the Earth magnetic field B_{total} . The heading is measured clockwise from the magnetic north (N) direction as the angle between OM \emptyset and N. ϑ_x and ϑ_y are measured counterclockwise as the rotation around the y - and x -axis. The three OMs are arranged clockwise within the storey frame, separated from each other by 120° in azimuth. The PMT centres are 0.142 m below the OM-plane. The radial distance to the storey axis is 0.578 m. In local coordinates the PMTs therefore have the following positions:

- PMT \emptyset : (0.578 m, 0.0 m, -0.142 m)
- PMT1: (-0.578/2 m, -0.578 $\sqrt{3}$ /2 m, -0.142 m)
- PMT2: (-0.578/2 m, 0.578 $\sqrt{3}$ /2 m, -0.142 m)

Euler angles α , β and γ are used to describe the storey orientation and the PMT positions. They are calculated in the track reconstruction software as:

$$\beta = -\arcsin(\sqrt{(\sin \vartheta_x)^2 + (\sin \vartheta_y)^2}) \quad (5.3)$$

$$\gamma = \arctan(\sin(\vartheta_x)/\sin(\vartheta_y)) \quad (5.4)$$

$$\sin \alpha = (-\sin \phi \cos \beta \cos \gamma - \cos \phi \sin \gamma)/\sqrt{1 - \sin^2 \beta \cos^2 \gamma} \quad (5.5)$$

$$\cos \alpha = (\cos \phi \cos \beta \cos \gamma - \sin \phi \sin \gamma)/\sqrt{1 - \sin^2 \beta \cos^2 \gamma} \quad (5.6)$$

$$\alpha = \arctan(\sin \alpha / \cos \alpha). \quad (5.7)$$

5.3 Hardware components and measured quantities

In order to measure the detector geometry in situ, two types of positioning equipment have been installed in ANTARES:

- Tiltmeter Compass System (TCS): Two tiltmeters and three B -field sensors on each storey (mainly TCM2-20 by PNI sensor cooperation [94]). The heading is obtained by measuring two perpendicular components B_x and B_y of the horizontal component of the Earth magnetic field $\vec{B}_0 = \vec{B}_{\text{NS}} + \vec{B}_{\text{EW}}$, which has the following components at the ANTARES site (elevation -2.2 km): $B_{\text{NS}} = 23.9 \mu\text{T}$, $B_{\text{EW}} = 0.06 \mu\text{T}$ (data 2004) [95]. The heading ϕ is obtained by

$$\tan(\phi) = -\frac{B_y B_{\text{NS}} - B_x B_{\text{EW}}}{B_x B_{\text{NS}} + B_y B_{\text{EW}}} \approx -\frac{B_y}{B_x}. \quad (5.8)$$

Pitch and roll of the storey are measured via the tiltmeters. The TCM2-20 device has the following specifications:

- heading: accuracy (leveled/tilted) $0.5^\circ/1.0^\circ$, precision 0.1° (numerical output of the device in multiples of 0.1°).
 - pitch/roll: accuracy 0.5° , precision 0.1° , range $\pm 20^\circ$.
- Acoustic Positioning System (APS): Five receiving hydrophones per line on storeys 1, 8, 14, 20 and 25 (larger density in the upper part of the line) and an emitter/receiver module on each BSS. The APS uses 40-60 kHz signals with an attenuation length of 700-1000 m in water thus covering the full ANTARES detector dimensions, to measure time delays between emitters and receivers. The sound velocity (≈ 1500 m/s) is measured in situ at different positions inside the instrumented volume of the telescope [96]. It depends on temperature, pressure (depth) and salinity. The depth dependence is corrected in first order by $v_s(z) = v_s(z_0) - k_s(z - z_0)$ with $k_s = 1.71$ cm/s/m. The effect of non-linear sound propagation results in a bending radius of about 80 km [97]. Since this is more than 100 times larger than typical dimensions of the detector, the sound path is taken as a straight line. The temperature is stable around 13°C . From the timing information and the measured sound velocity the positions of the hydrophones on a line can be obtained by triangulation. As an example see figure 5.4 where the displacement of the five hydrophones of Line 3 is shown as a function of time. Further details on the APS are found in [1].

The raw data both from the TCS and the APS is taken via Slow Control every two minutes and written to the ANTARES database. Before using this data to compute the detector geometry it needs to be calibrated, as explained in the next section.

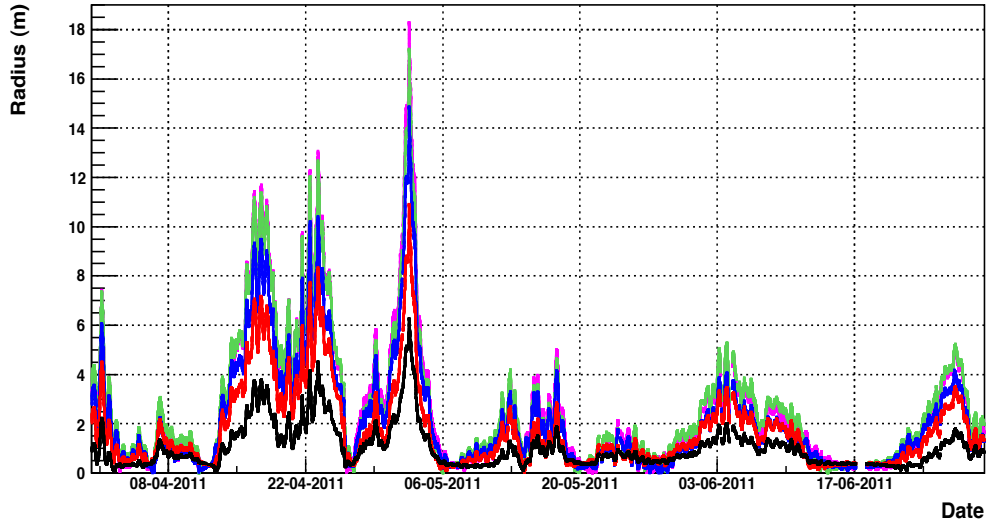


Figure 5.4: Radial displacements of the five hydrophones on Line 3 as function of time. Line displacements from the vertical up to 18m are observed. Colours: Storey 1 black, Storey 8 red, Storey 14 blue, Storey 20 green, Storey 25 magenta (figure from ANTARES internal pages or [1]).

5.4 In situ calibration of tiltmeters and compasses

During the onshore integration of the ANTARES lines the tiltmeters and compasses have been mounted precisely into the LCM and calibrated in the lab. As the operation conditions in the deep sea are quite different from those in the lab (temperature, pressure, full power consumption) these devices need to be re-calibrated in situ on a regular basis.

Calibration of pitch ϑ_x and roll ϑ_y

As the orientation of the whole line and the headings of the storeys vary with time, we expect a distribution of the two locally measured tilt angles around zero if measured for a significantly long period. As can be seen from figure 5.5 there are offsets that are corrected via:

$$\vartheta_i^{\text{calib}} = \vartheta_i^{\text{raw}} - \vartheta_i^{\text{offset}} \quad i \in \{x, y\}. \quad (5.9)$$

As can be seen from table 5.1 these offsets are very stable, even after redeployments of lines. Table 5.1 shows the calibration constants for Line 9 before (deployment in 2007) and after redeployment in 2010. Small differences arise from mechanical stress during recovery and redeployment, especially after opening of a LCM container.

Calibration of heading ϕ via B_x and B_y

5.4 In situ calibration of tiltmeters and compasses

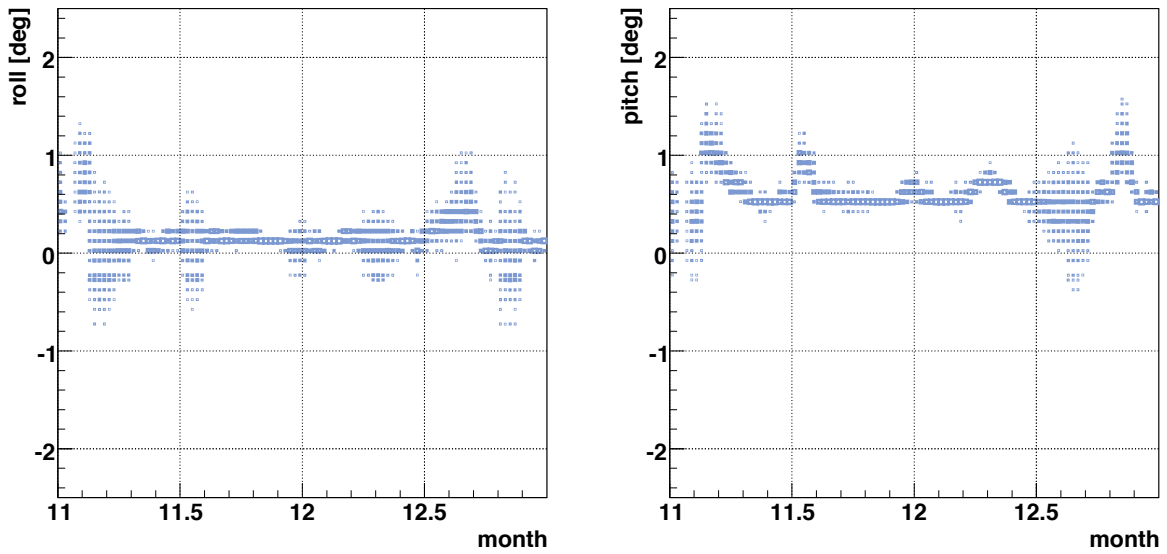


Figure 5.5: *Left*: Uncalibrated roll data of Line 12 Storey 9. *Right*: Uncalibrated pitch data of Line 12 Storey 9. Data for both plots are from Nov./Dec. 2010. In this case the observed offsets are 0.6° for pitch and 0.1° for roll.

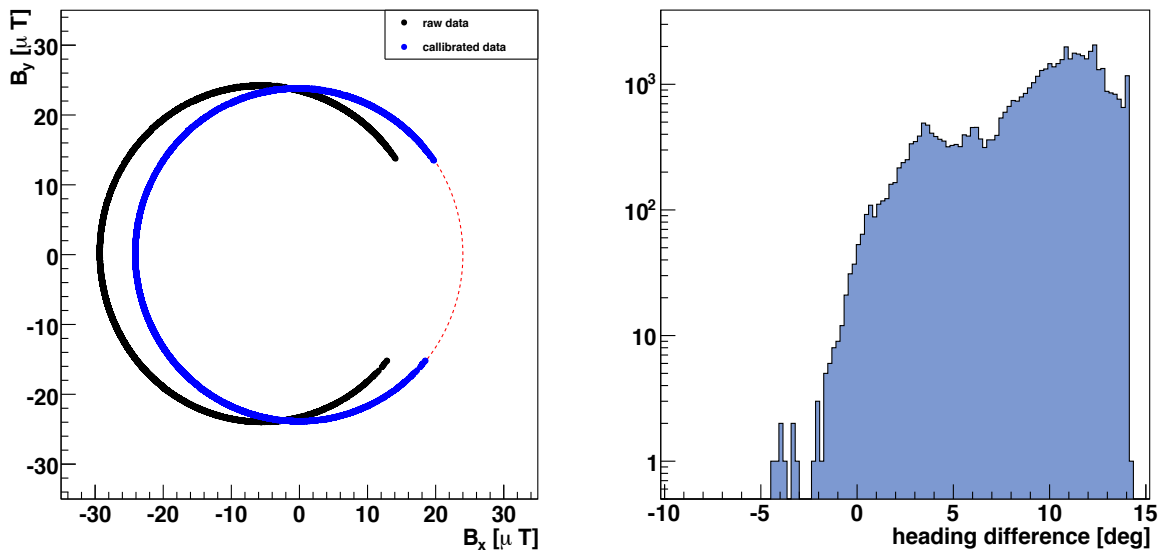


Figure 5.6: *Left*: B-field measurement of the compass on Line 12 Storey 22. Raw data (black) and calibrated data (blue) are shown. The dashed red line represents the expectation, a circle with radius 23.9μ T. *Right*: Distribution of heading difference (in degrees) between raw and calibrated data of Line 1 Storey 17. Differences of more than 10 degrees are observed in this case. Data was taken from 09/2010 to 12/2010.

storey	par	before	after	par	before	after
1	$\vartheta_x^{\text{offset}}$	-0.4	-0.4	$\vartheta_y^{\text{offset}}$	0.0	0.0
2	$\vartheta_x^{\text{offset}}$	-13.2	-13.2	$\vartheta_y^{\text{offset}}$	-0.2	-0.2
3	$\vartheta_x^{\text{offset}}$	-1.1	-1.6	$\vartheta_y^{\text{offset}}$	-0.7	-0.9
4	$\vartheta_x^{\text{offset}}$	1.2	1.1	$\vartheta_y^{\text{offset}}$	1.9	2.5
5	$\vartheta_x^{\text{offset}}$	-1.4	-2.0	$\vartheta_y^{\text{offset}}$	2.9	3.9
6	$\vartheta_x^{\text{offset}}$	-0.3	-0.1	$\vartheta_y^{\text{offset}}$	0.2	0.2
7	$\vartheta_x^{\text{offset}}$	-0.1	-0.3	$\vartheta_y^{\text{offset}}$	-0.2	-0.2
8	$\vartheta_x^{\text{offset}}$	0.0	0.0	$\vartheta_y^{\text{offset}}$	0.3	0.3
9	$\vartheta_x^{\text{offset}}$	-1.4	-1.8	$\vartheta_y^{\text{offset}}$	2.5	2.9
10	$\vartheta_x^{\text{offset}}$	-0.7	-1.1	$\vartheta_y^{\text{offset}}$	4.0	2.9
11	$\vartheta_x^{\text{offset}}$	0.0	0.3	$\vartheta_y^{\text{offset}}$	-0.2	0.0
12	$\vartheta_x^{\text{offset}}$	0.3	0.3	$\vartheta_y^{\text{offset}}$	0.1	0.1

Table 5.1: Tiltmeter calibration parameters (par, in degrees) before (deployment in 2007) and after redeployment of Line 9 in 2010. The first twelve storeys are shown.

Due to magnetic fields originating from currents inside the LCM container under operation and due to mis-calibration of the B-field sensors prior to deployment, also the heading needs to be calibrated regularly in situ. This is done as follows: For a full turn of a particular storey (neglecting the East-West component of $0.06 \mu\text{T}$ compared to North-South component of $23.9 \mu\text{T}$) we expect to obtain a circle with radius $23.9 \mu\text{T}$ in a B_x - B_y -plot (see figure 5.6). Deviations in the radius or elliptical shapes are due to mis-calibrations, while shifts of the centre of the circle are due to internal magnetic fields rotating simultaneously with the storey. For calibration one has to find constants a_i and b_i that are used to map the raw data on the expected centered circle. The calibrated values are calculated via:

$$B_i^{\text{calib}} = a_i(B_i^{\text{raw}} - b_i) \quad i \in \{x, y\}. \quad (5.10)$$

Figure 5.6 right shows the angle difference for the heading of Line 1 Storey 17 between raw and calibrated data. As can be seen, differences up to 15° are observed in this case. The calibration parameters both for B_x and B_y and the tilts are stored in the database (for table design see Appendix). They are automatically read by the alignment software package. Calibration data are available from 02/2007 on. After calibrating the TCS-data, both this and the APS-data are used to reconstruct the storey positions using a mechanical line shape model.

5.5 Mechanical line shape model

In order to determine positions of storeys that do not carry a hydrophone a mechanical model is used and models the line shape for any sea current velocity. For this model, it

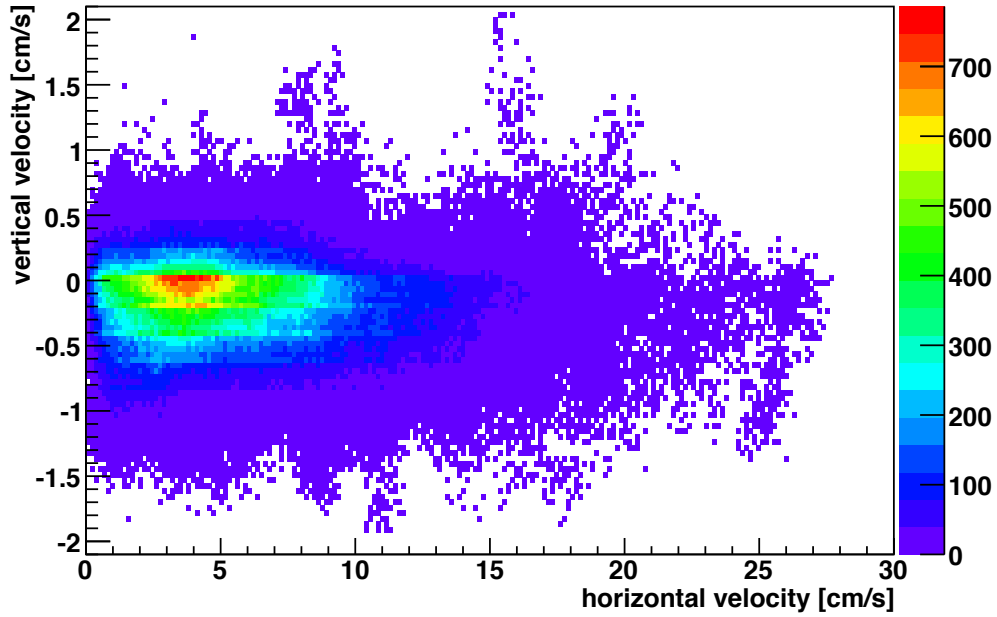


Figure 5.7: Vertical versus horizontal sea current velocity measured by the ADCP in 2009. The vertical velocity component is negligible within the accuracy of the ADCP measurement (mind the different scales on both axes).

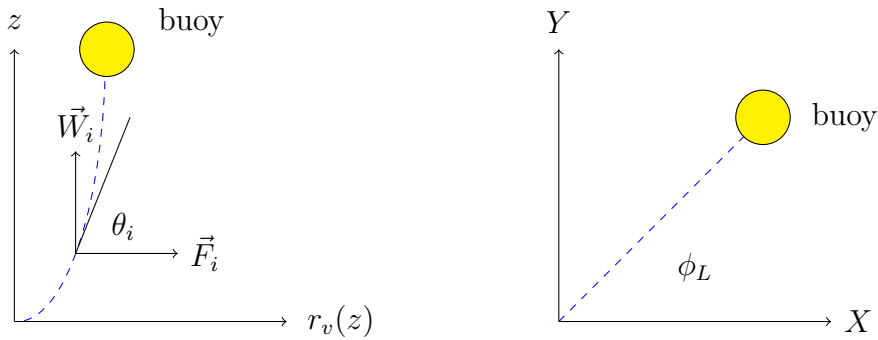


Figure 5.8: *Left*: Forces that act on each line element. Effective weight \vec{W} (weight minus buoyancy) and drag from sea current \vec{F} . *Right*: Illustration of line azimuth ϕ_L (direction of inclination).

is assumed that the sea current velocity \vec{v} has only a time dependence but no depth and horizontal position dependence within the detector volume. Furthermore, the vertical component v_z is assumed to be negligible, which has been confirmed by measurements using an acoustic doppler current profiler (ADCP, see figure 5.7):

5 The alignment of ANTARES

$$\vec{v} = (v_x(t), v_y(t), 0). \quad (5.11)$$

The shape of the line is determined by two forces that act on each line element (storey, cable, buoy):

- Effective weight $\vec{W} = (0, 0, W)$, i.e. weight minus buoyancy.
- Drag from sea current $\vec{F} = (F^x, F^y, 0)$.

The values for W , $\frac{F}{v^2} = \frac{1}{2}\rho c_w A$ and the total line length, mainly composed from cable lengths and storey heights, have been measured prior to deployment (see table 5.2) and are set individually for each line of the detector.

line	id	length	W_{storey}	F/v^2	W_{cable}	F/v^2	W_{buoy}	F/v^2
1	6405	452.844	265.6	383.8	-52.9	222.0	6759.09	453.0
2	6406	461.552	265.6	383.8	-52.9	222.0	6827.76	453.0
3	6407	461.615	265.6	383.8	-52.9	222.0	7112.25	453.0
4	6408	461.651	265.6	383.8	-52.9	222.0	6916.05	453.0
5	6409	461.458	265.6	383.8	-52.9	222.0	6719.85	453.0
6	6410	462.011	265.6	383.8	-52.9	222.0	6984.72	453.0
7	6411	462.241	265.6	383.8	-52.9	222.0	6896.43	453.0
8	6412	462.304	265.6	383.8	-52.9	222.0	6896.43	453.0
9	6413	461.581	265.6	383.8	-52.9	222.0	6906.24	453.0
10	6414	461.802	265.6	383.8	-52.9	222.0	6935.67	453.0
11	4631764	461.807	265.6	383.8	-52.9	222.0	6719.85	453.0
12	4631765	447.259	265.6	383.8	-52.9	222.0	6719.85	453.0

Table 5.2: Individual parameters (id, length, drag, effective weight) for storey, cable (scaled to 14.5 m) and buoy used for the linefit. $[Length] = \text{m}$, $[W] = \text{N}$, $[F/v^2] = \text{Ns}^2/\text{m}^2$. The buoy buoyancies are given by the manufacturer for an operation depth of $\sim 2000 \text{ m}$. Note: For Line 1 the cable to the first floor has been shorten. Line 12 only has 24 storeys.

The line inclination on storey i is given by the ratio of the two overall forces from flow resistance F and effective weight W of the components above (see figure 5.8):

$$\tan \theta_i = \frac{\sum_{j=i}^N F_j}{\sum_{j=i}^N W_j}, \quad (5.12)$$

where $N - i$ is the number of storeys above storey i . The effective weight is given by the weight minus the buoyancy and the flow resistance by $F_j = 1/2\rho c_w A_j v^2$. To obtain a continuous function, the effective weights of storeys and cables (25 per line) are smeared homogeneously over the whole line (length l), while the buoy effective

weight and drag is assigned to the line top. The first 100 m of cable from the BSS to the first storey are labeled by the subscript ‘‘BSS’’. This results in

$$W(z) = (25(W_{\text{storey}} + W_{\text{cable}}) + W_{\text{cable,BSS}}) \frac{l-z}{l} + W_{\text{buoy}}. \quad (5.13)$$

The flow resistance is treated in the same way:

$$F(z) = (25(\frac{F_{\text{storey}}}{v^2} + \frac{F_{\text{cable}}}{v^2}) + \frac{F_{\text{cable,BSS}}}{v^2}) v^2 \frac{l-z}{l} + \frac{F_{\text{buoy}}}{v^2} v^2. \quad (5.14)$$

Identifying the ratio W/F by the slope of the line at height z one gets (r denotes the radial displacement):

$$\frac{dz}{dr} = \frac{W(z)}{F(z)} = \frac{a-bz}{c-dz} =: \frac{1}{f(z)}, \quad (5.15)$$

where a , b , c and d are defined as follows:

$$a = 25(W_{\text{storey}} + W_{\text{cable}}) + W_{\text{cable,BSS}} + W_{\text{buoy}}, \quad (5.16)$$

$$b = \frac{25}{l}(W_{\text{storey}} + W_{\text{cable}}) + \frac{1}{l}W_{\text{cable,BSS}}, \quad (5.17)$$

$$c = \left[25 \left(\frac{F_{\text{storey}}}{v^2} + \frac{F_{\text{cable}}}{v^2} \right) + \frac{F_{\text{buoy}}}{v^2} + \frac{F_{\text{cable,BSS}}}{v^2} \right] v^2, \quad (5.18)$$

$$d = \frac{25}{l} \left(\frac{F_{\text{storey}}}{v^2} + \frac{F_{\text{cable}}}{v^2} \right) v^2 + \frac{1}{l} \frac{F_{\text{cable,BSS}}}{v^2} v^2. \quad (5.19)$$

By integration of equation (5.15) one obtains the line shape formula for radial displacement of the line as a function of height z and sea current velocity v

$$r_v(z) = \int_0^z f(z') dz' = \frac{d}{b}z - \frac{cb-da}{b^2} \ln \left(1 - \frac{b}{a}z \right), \quad (5.20)$$

where the logarithmic term is responsible for the characteristic shape. The storey’s real z -position z_i can be obtained by calculating the curve integral

$$s = \int_0^{z_i} \sqrt{1 + r'_v(u)^2} du, \quad (5.21)$$

where s is the storey position along the line. As can be seen from formula 5.20 the total line length is needed as well and is obtained by summing up the individual lengths of cables and storeys that make up the line. The cable lengths have been measured at 1000 kg drag in the lab. The line shape formula is used to fit the data using a least square fit.

5.6 The χ^2 -fit

A χ^2 -fit is used to determine the geometrical shape of a line (ϕ_L denotes the line azimuth = direction of line inclination) from the measured tilts/headings and hydrophone positions. The χ^2 has the following contributions:

- Hydrophone positions $h_{x(y)}^*$ with errors $\Delta h_{x(y)}$. The hydrophone $h_{x(y)}$ on each storey is mounted on a 0.293 m long arm. Therefore the position is recalculated as the storey center position (stared coordinates):

$$+ \frac{(r(z) \cos(\phi_L) - h_x^*)^2}{(\Delta h_x)^2} \quad (5.22)$$

$$+ \frac{(r(z) \sin(\phi_L) - h_y^*)^2}{(\Delta h_x)^2} \quad (5.23)$$

- Storey headings ϕ_i with errors $\Delta\phi_i$ ($i = 1, \dots, 25$):

$$+ \frac{(\phi_L - \phi_i)^2}{(\Delta\phi_i)^2} \quad (5.24)$$

- For the storey tilts ϑ^i with errors $\Delta\vartheta^i$ two strategies are possible:

- Version A: Trust the individual azimuth and use the full tilt:

$$+ \frac{(r'_i(z) - \tan \vartheta_i)^2}{(\tan' \vartheta_i \Delta\vartheta_i)^2} \quad (5.25)$$

- Version B: Project the individual tilt on the current line plane ($\delta\phi_i = \phi_L - \phi_i$):

$$+ \frac{(r'_i(z) - \sin \vartheta_i \cos \delta\phi_i)^2}{(\cos \delta\phi_i \cos \vartheta_i \Delta\vartheta_i)^2 + (\sin \delta\phi_i \sin \vartheta_i \Delta\vartheta_i)^2} \quad (5.26)$$

The errors are as follows: $\Delta h_{x(y)} = 5$ cm, $\Delta\phi_i = 1^\circ$ and $\Delta\vartheta_i = 0.2^\circ$. The fit procedure returns the two components v_x and v_y and the corresponding errors. From these the sea current velocity v and direction ϕ_{current} can be obtained by:

$$v = \sqrt{v_x^2 + v_y^2}, \quad \phi_{\text{current}} = \phi_L = \arctan(v_y/v_x). \quad (5.27)$$

At the moment version B is used for alignment processing. Version B results, due to the projection step, in slightly lower velocities from the line fit. Version A gives larger inclinations and is therefore not useable for very low sea current velocities. In order to take into account for temporarily or permanently non (properly) working tiltmeters oder compasses, individual devices can be discarded in the fit.

5.7 Nominal detector geometry

Besides the real-time geometries, that are produced every two (six, see section 5.8) minutes, there are so-called nominal geometries for the PMT positions and orientations with the following properties:

- This geometry contains photomultiplier-positions instead of storey positions.
- Lines $\ell = 1 \dots 12$ are vertical and the lateral geometry of the storey is neglected (OMs $k = 1 \dots 75$ are on the line):

$$X_k^\ell = X_{\text{BSS}}^\ell, Y_k^\ell = Y_{\text{BSS}}^\ell.$$

- The photomultipliers are located in the lower part of the Optical Module. Their Z -position is 0.142 m below the plane defined by the Optical Modules. Cable lengths are taken as real values from the database.
- The photomultiplier orientation is not specified:

$$\vartheta_{x,y} = \phi = 0.$$

- Positions of LED-/Laser-beacons within the detector are included. They are placed 1.003 m above the plane defined by the centres of the Optical Modules.
- All coordinates are UTM-coordinates.

These geometries are used by the various triggers within the data acquisition software (therefore also referred as trigger geometry) and read in by the initialization routine at the run start. Both nominal geometries and real time geometries are computed using a C++ software described in the next section.

5.8 AlignReco software, data processing and data storage

AlignReco software

The alignment is computed by the software package *AlignReco* written in C++. AlignReco is used for the computation of both nominal and real-time geometries. It is independent of the standard SeaTray software framework for data analysis. An overview of the AlignReco releases and major improvements can be found in the Appendix. The software layout reflects the hardware structure of the ANTARES detector: For each element (line, storey, hydrophone, compass,...) a corresponding C++-class has been implemented. This provides good code readability and high flexibility for updates and extensions.

Data processing and storage

The frequency for taking the raw data from tiltmeters/compasses and hydrophones is once per six minutes until 27.03.2008 and once per two minutes afterwards. Therefore,

the computed geometries have two (six) minute validity periods and do always start on the full hour (for example start: 2009/09/09 09:00:00, end: 2009/09/09 09:02:00) by definition. Aligning the whole telescope for a two (six) minute timeslice follows this procedure:

1. Detector read-in: In this step all data related to the hardware of the detector (cable lengths, BSS-heights, device-product-ids,...) are obtained from the database and stored in a binary file for later use.
2. Reading tiltmeter/hydrophone data: For the processed timeslice of two minutes ($T_{\text{start}}, T_{\text{end}}$) the time-stamped data from tiltmeters and hydrophones are obtained from the database. In order to limit the parallel database access, this step is done via a single SQL command for the whole detector. In this step all data with times t_i in the particular timeslice is used: $T_{\text{start}} \leq t_i < T_{\text{end}}$.
3. Fitting the lineshape: Once the relevant data is received, the fit is performed using the MINUIT fitter from ROOT [81]. The data is saved in dedicated structures (C++ classes) for further use. The fit is done for each line separately.
4. Writing output to the database: Finally the positions and orientations including the errors, calculated by error propagation, of all storeys are written into the database. Further the fit output parameters v_x, v_y and the sea current direction ϕ_{current} for each line are stored. For the storage of positioning data and calibration parameters seven dedicated tables in the ANTARES database at computing centre Lyon are used. For detailed table design see appendix 10.8.

Concerning the performance, a single AlignReco run is able to produce the positioning data for the whole telescope of one day ($24 \cdot 30 = 720$ timeslices) within ≈ 9 hours. (real time). The performance is limited mainly by data-I/O with the ANTARES database. When using a batch system and splitting a larger time period in jobs for single days for example, positioning data can be calculated or recalculated on a manageable time scale.

5.9 Geometry reader for SeaTray

Since the position information calculated by the AlignReco software is stored in the database, track reconstruction software is able to gather this information and to use it for further calculations. The interface between the reconstruction framework SeaTray [98] and the database tables containing the real-time and trigger geometries of ANTARES can be found in the corresponding service.

This service can be configured to read both real-time geometries and nominal geometries. As nominal geometries are time-independent no update in an reconstruction process is necessary. As real-time geometries have two/six minute validities, the service provides the corresponding detector geometry valid at the time of the event to be

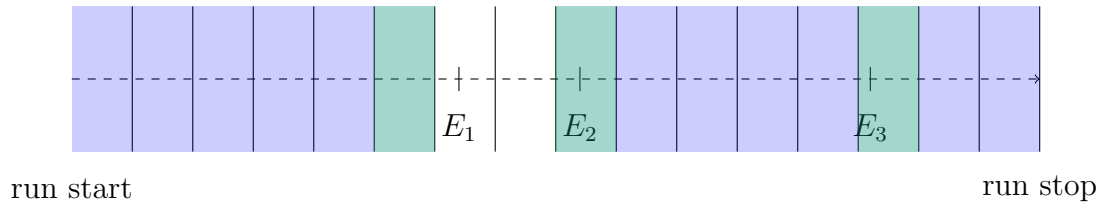


Figure 5.9: Illustration of alignment coverage with two-minute-timeslices (blue). Events might fall in non covered periods (white). The green timeslices are picked for the events $E_1 - E_3$ by the geometry service.

reconstructed. If the alignment coverage with geometries is not complete the default option is as follows: For a given (event-)time the interface tries to find the corresponding two-minute geometry timeslice in database of the specified alignment version. If this fails, the nearest timeslice is picked (see figure 5.9).

After obtaining the data, the services also handle the necessary calculations to provide the positions of the Optical Modules (for real-time geometries the database contains only storey positions). This is internally done using the Euler angles as described in section 5.2. Figure 10.6 in the appendix demonstrates that the internal conversions are done correctly.

5.10 Quality and accuracy of alignment data

Line shape

A first simple quality check is the line shape itself viewed from different directions. Figure 5.10 left shows the shape of Line 1 (as fitted by AlignReco) at different velocities. For 21 cm/s the uppermost storey is more than 15 m deflected from the vertical configuration. Figure 5.10 right shows the line shape from top. As the sea current is uniform in direction on the scale of the detector, the lines are found to be parallel.

In figure 5.11 the radial difference between fitted story position of Storey 20 Line 3 (data from March 2010) and the position of the hydrophone, corrected by the offset from the line axis, is shown. The mean of the distribution is at 0.008 m, the RMS at 0.045 m. Therefore the system is free of systematic errors and achieves the required accuracy of better than 10 cm.

Comparison with ADCP

The velocity (absolute value and direction) from the line fit procedure can also be compared to the measurement of the Acoustic Doppler Current Profiler (ADCP) on the instrumentation line: Figure 5.12 shows the time evolution of these two velocity measurements. The observed agreement demonstrates that the line shape model is correct. Further this technique provides a longterm monitoring of sea currents at the ANTARES site in addition to the ADCP. As the sea current speed is an important input parameter for detector operation under highly variable environmental condi-

5 The alignment of ANTARES

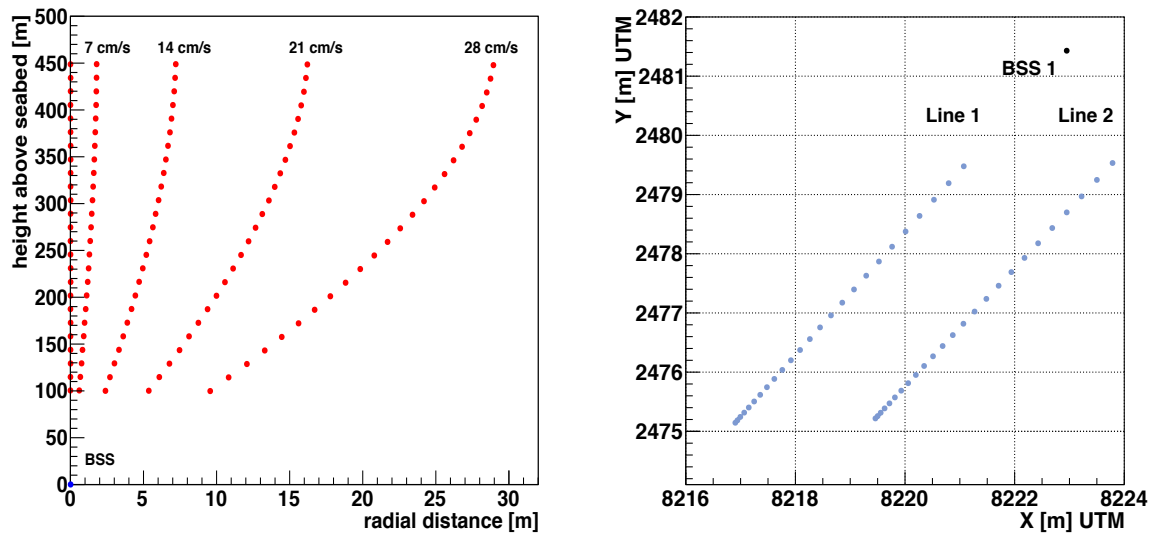


Figure 5.10: *Left:* Radial displacement (note the different scale on the two axes) of the 25 storeys of Line 5 for different sea current velocities (0.0/7.0/14.0/21.0/28.0 cm/s). The BSS coordinates have been set to (0,0). *Right:* Storey positions (blue dots) in the X-Y-plane: The lines are perfectly parallel, the projected curvature is also visible. BSS of Line 1 shown (black dot).

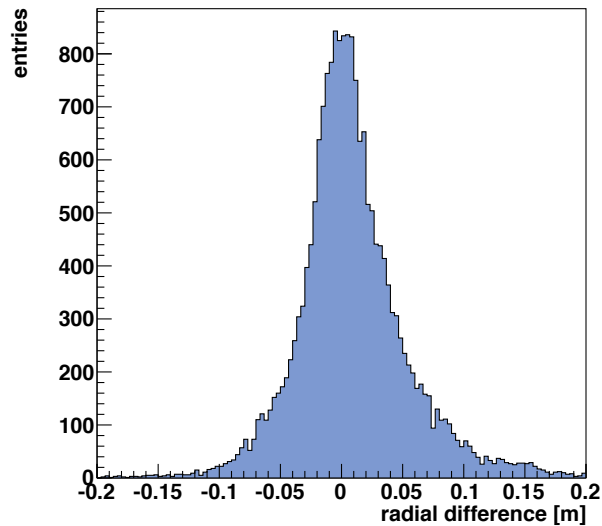


Figure 5.11: Radial difference between fitted storey position and the hydrophone position (corrected by the offset from the line axis). The mean of the distribution is at 0.008 m, the RMS at 0.045 m.

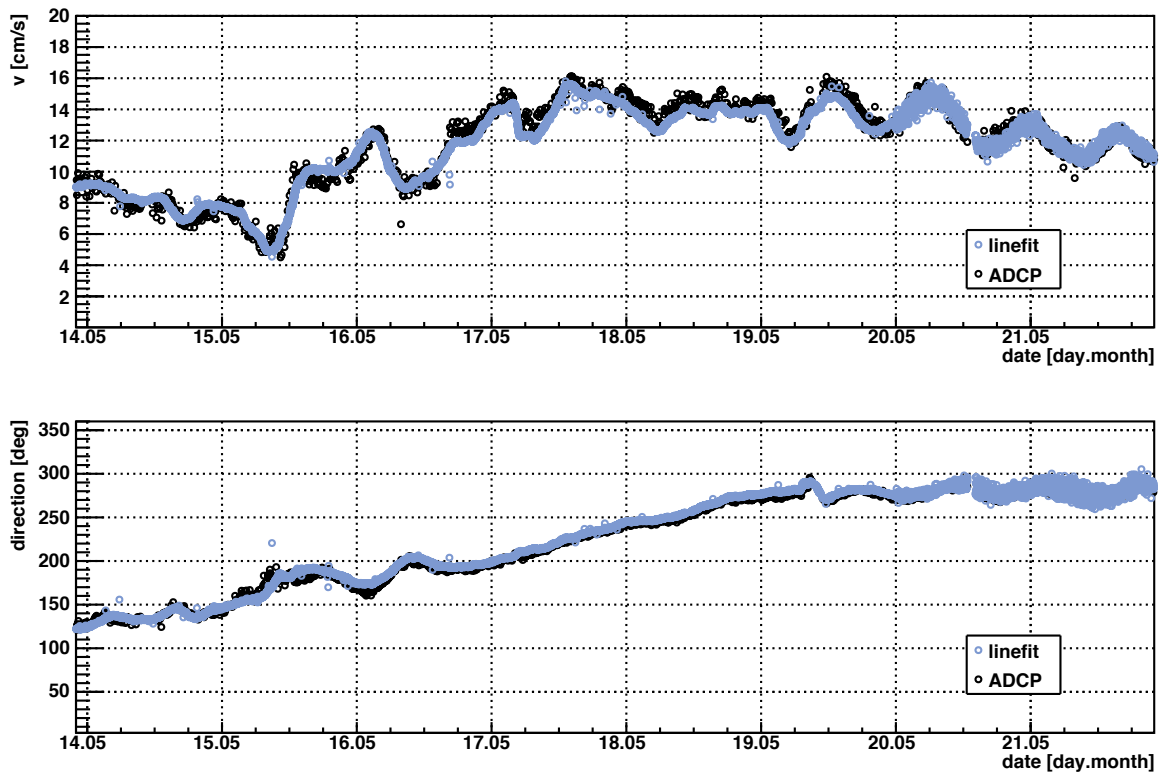


Figure 5.12: Time evolution of velocity data from ADCP and line fit in 2008. *Upper panel:* Absolute current velocity. *Lower panel:* Direction of sea current velocities (0° corresponds to North).

tions, the velocity measurement from the alignment provides redundancy in case of non available ADCP data.

Heading comparison on acoustic storeys

The prototype acoustic particle detection system AMADEUS [46] within ANTARES provides the opportunity to crosscheck both measurement and calibration of the compasses on the acoustic storeys (see figure 5.13 right). For this procedure the acoustic pinger signals of the standard ANTARES acoustic positioning system are used. By recording these pinger signals and subsequent triangulation the positions of the six hydrophones on the uppermost storey of the instrumentation line can be calculated. From the known nominal (local) hydrophone positions within the storey frame are fitted to the hydrophone positions reconstructed in situ. The resulting heading of the storey can be compared to the measurement of the compass card. For this procedure the UTM convergence angle has not been taken into account. Furthermore, there is an error introduced by interpolation, as the acoustic measurement and the compass board measurement are not performed synchronously. Nevertheless, the two procedures show a very good agreement (see figure 5.13 left). The resolution between the two measurements is 1.7° (see [99]). Especially the correct determination and appli-

5 The alignment of ANTARES

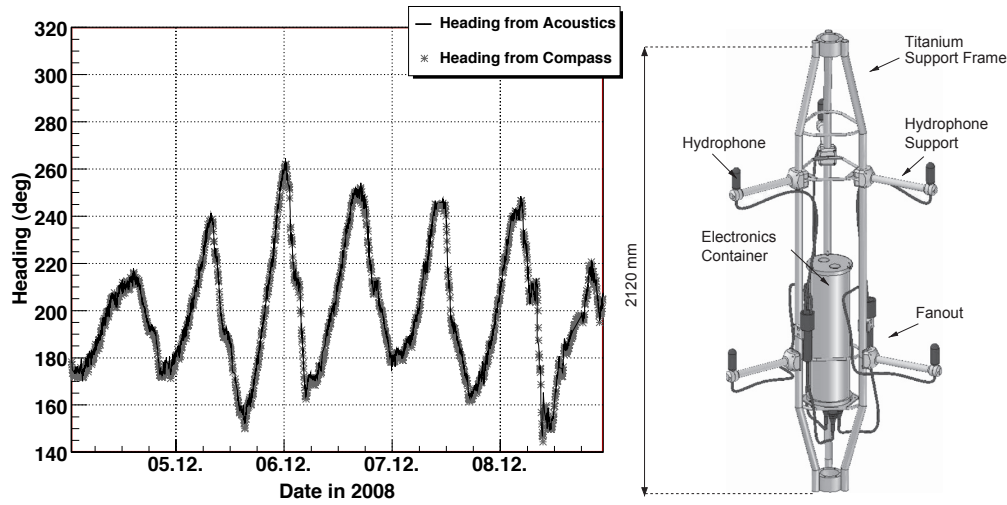


Figure 5.13: *Left*: Heading of the uppermost storey of the instrumentation line measured both with the compass board and the acoustic hydrophones (data from five days). The results from the two methods perfectly agree (figure from [99]). *Right*: Drawing of an Acoustic Storey carrying six hydrophones on a standard ANTARES storey frame (figure from [46]).

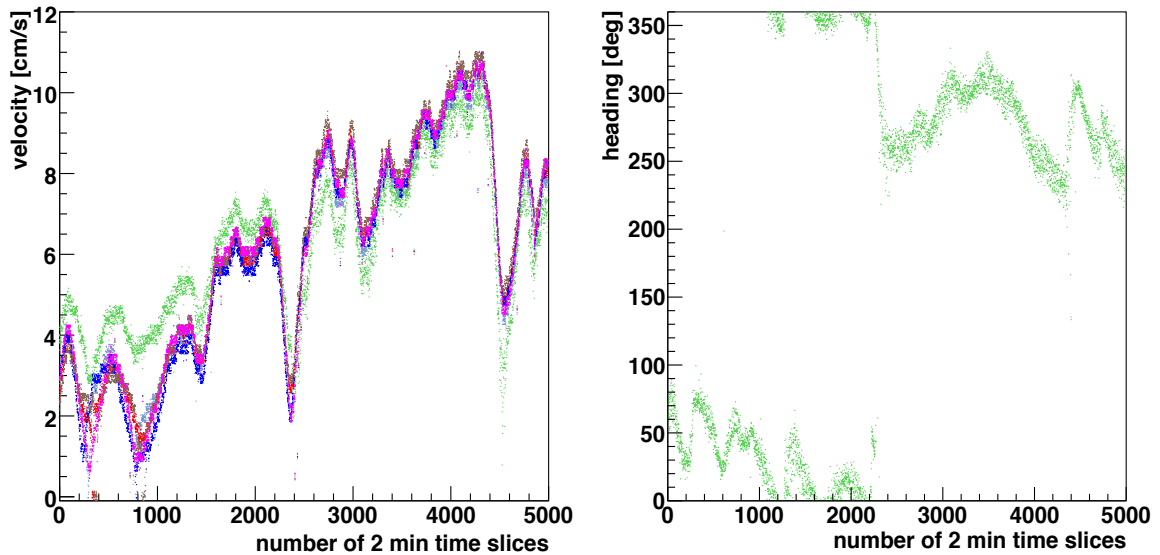


Figure 5.14: *Left*: Time evolution of the velocities derived from the Line 1-6 data (blue, green, red, dark blue, brown, purple). Line 2 shows first higher and later lower velocities than the other lines (see text). *Right*: Direction of the sea current velocity from the fits of Line 2. For explanation see text.

cation of the compass in-situ calibration is confirmed.

Interline velocities

Since the line fit is performed individually for each line we can compare the results among different lines. If we assume a homogeneous velocity of the sea current inside the detector volume, we should observe the same velocity from each single line fit. As shown in figure 5.14 left this is indeed the case. Wrong buoyancy and drag coefficients lead to offsets in such plots. As can be seen Line 2 (green dots) shows a different behavior: The velocity is first observed to be larger than the one observed by the other lines, then it is smaller. As can be seen from the right plot in figure 5.14 this change is in coincidence with a direction change of almost 180 degrees. It has been shown [100] that this is an effect of small errors on the BSS coordinates that results in azimuth dependent velocities as a fit output. Velocities of Lines 7-12 are in good agreement (not shown).

The assumption of a homogeneous sea current velocity can be checked by looking at the twelve different line azimuths from the independent fit procedures. Figure 5.15 shows the fitted azimuth of six lines versus time. An excellent agreement is observed. Figure 5.16 exhibits the distribution of the angular deviation of the ten single measurements from the average direction in May 2008. An RMS of only 1.9 degrees confirms the homogeneity assumption.

Flooded OMs

The unrequested event of a full or partial OM flooding might be detectable using the tiltmeter data of the storey in question. Once an OM is flooded with seawater the additional weight causes a new equilibrium for the pitch and roll in the time evolution as shown in figure 5.17. Observing the effect in coincidence with a breakdown of the electrical connection provides a method of finding such OMs without expensive submarine operations.

Alignment without hydrophones

In principle the alignment can be performed without using hydrophone data. Of course, this leads to with a lower precision on the final storey position. As can be seen from figure 5.18 the effect is clearly visible. At $X/Y = (-2/1)$ the alignment was computed without hydrophones, the scattering is increased.

5.11 Conclusion

The positioning system of ANTARES, combining both the acoustic part and the compass-tiltmeter system, and the interfaces to the general data analysis framework SeaTray have been fully developed and tested. All relevant input and calibration data of the measuring devices have been transferred to the central Oracle database in Lyon. The data-IO routines for the database have been tested and optimised for high access rates.

5 The alignment of ANTARES

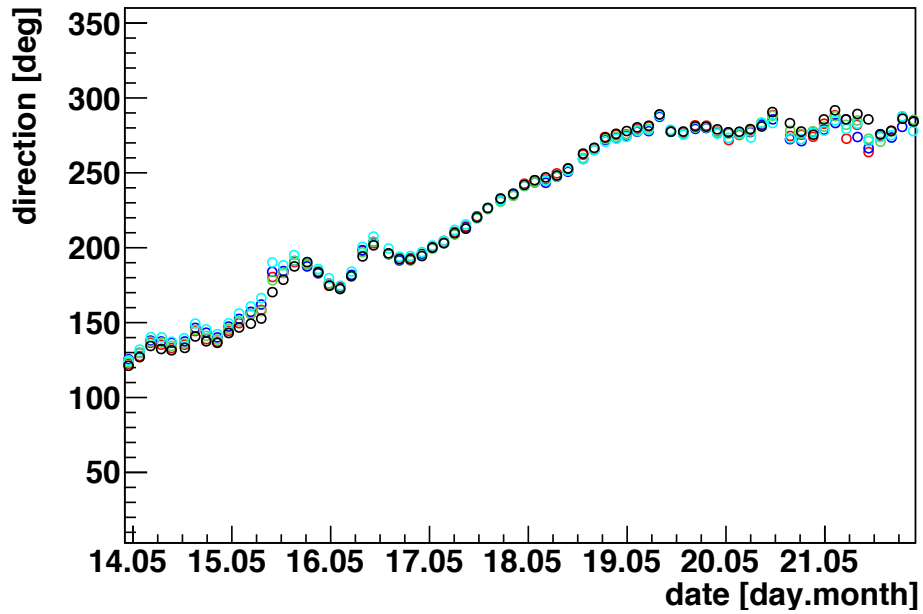


Figure 5.15: Fitted sea current directions from five lines as function of time in 2008 (Line 2 = red, Line 3 = blue, Line 4 = green, Line 5 = turquoise, Line 6 = black). A perfect agreement is observed.

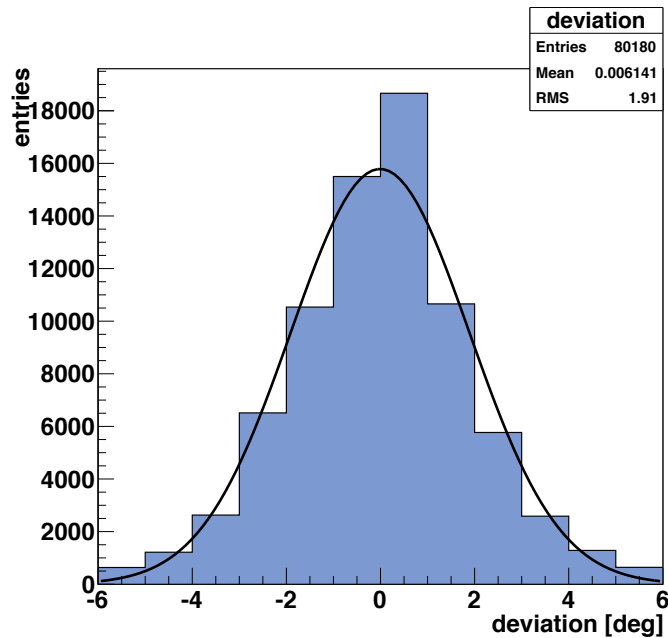


Figure 5.16: Deviation of the ten single direction measurements from the average direction. The RMS of the distribution is 1.9 degrees.

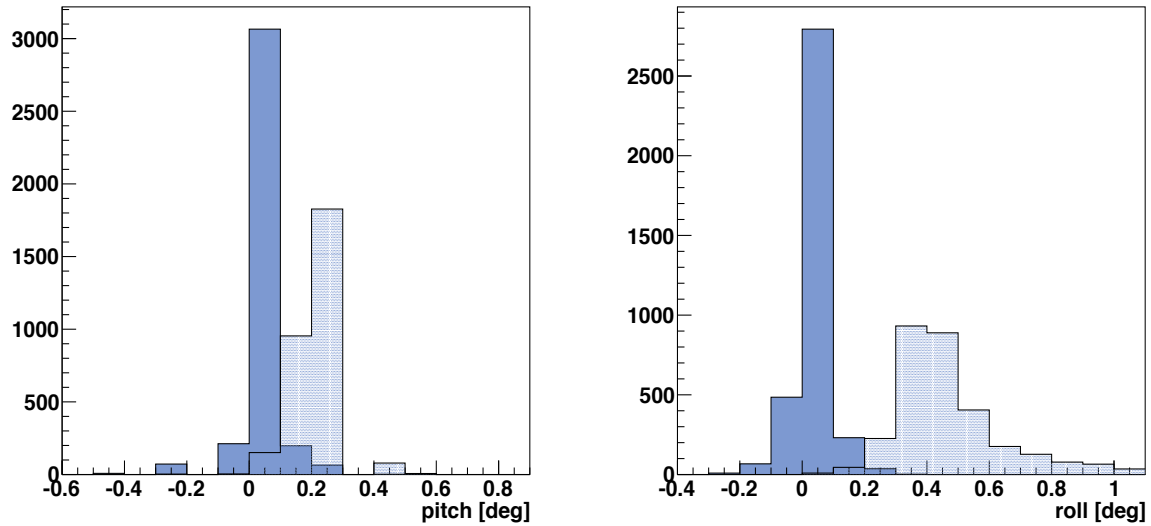


Figure 5.17: Pitch/Roll (left/right panel) distribution of Line 10 floor 23 before (solid blue) and after (dotted blue) the OM flooding on Jan 15th 2008.

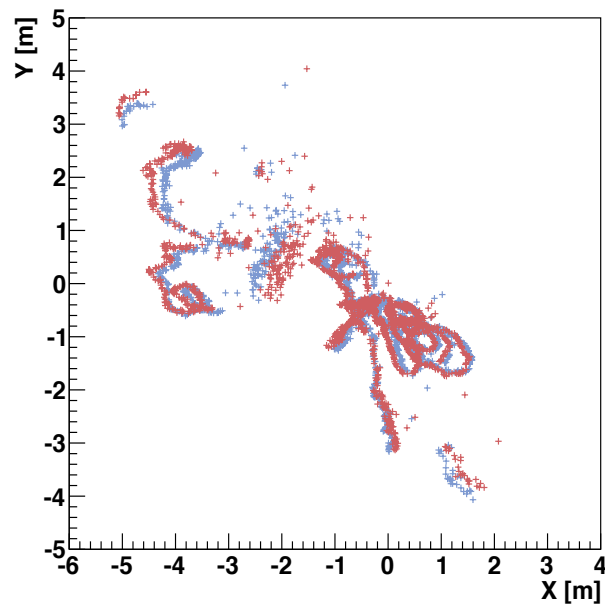


Figure 5.18: Position of the upmost storey relative to the BSS for Line 1 (blue) and 2 (red). For periods without hydrophone data there is an increased scattering of the reconstructed storey positions.

5 *The alignment of ANTARES*

The quality of the calibration data itself has been crosschecked with different measurements of other devices available at the telescope (ADCP, Acoustic Modules) and good agreement has been found. The assumption of a homogeneous sea current inside the instrumented detector volume has been confirmed.

6 Cluster search

In brief:

- Several astrophysical source types are known to have variable photon fluxes with flare durations between several minutes and several days. From hadronic models an associated neutrino emission is predicted.
- The TANAMI observation program provides radio monitoring of bright AGN south of declination -30 degrees, which is complemented by looking for neutrinos with the ANTARES neutrino telescope.
- Driven by the launch of *Fermi*, many *Fermi*/LAT-detected sources were added to the TANAMI sample. Therefore also gamma-ray observations are available for these AGN.
- In order to improve the discovery chance, time-dependent searches with the ANTARES telescope are performed.
- A new code for time-dependent searches has been developed. A search for neutrinos from eight TANAMI sources is presented.

6.1 Introduction

As already mentioned in chapter 1, AGN are promising sites for high-energy neutrino production. For neutrino observations, especially from still poorly understood acceleration processes inside AGN jets, the AGN orientation is important: The jet must be aligned towards the Earth as it is the case for quasars or BL Lac objects (see chapter 1 figure 2.6 left). AGN jets show outbursts and variabilities on a broad range of timescales, down to intraday fluctuations. The processes of formation, acceleration and collimation of these jets are, however, not yet clear. The observation of neutrino signals in general and in particular in correlation with gamma-ray or radio emission (jets have exclusively been seen for radio-loud objects) from such sources would give a deeper insight into the particles and processes involved.

From theoretical considerations (for an overview see [101,102] and references therein) the neutrino emission might be correlated with flaring emission of gamma-rays. Therefore the flaring behavior becomes one of the selection criteria for the source sample. Radio-loud sources, monitored by high-resolution VLBI programs, are of special interest since a possibly detected neutrino signal could be correlated with ejections or directional changes of jet components. As ANTARES is located in the Northern

Hemisphere and therefore observes the southern sky, the TANAMI AGN monitoring program (see section 6.2.1) provides an excellent candidate sample of bright and variable AGN in the southern sky, with VLBI radio data coverage and in addition a large range of multi-wavelength observational data, for example gamma-ray data from the *Fermi* satellite.

Analyses that also take the timing information of neutrino events from candidate sources into account can improve the discovery chance by requesting time clusters within the event sample associated to a given source. The goal of this work is to present a general analysis method that is not specifically using time information from light curve data of gamma-ray or radio observations, but looking for time-clustered events in a long observation period. To perform this search a new search method has been developed and tested.

This chapter is divided in three main parts: First the TANAMI AGN program and the selected source sub-sample is discussed, then the real data treatment and a source flux simulation is presented, finally the search method and its performance is described.

6.2 The TANAMI program and source candidate selection

6.2.1 The TANAMI program

The TANAMI program (Tracking Active Galactic Nuclei with Austral Milliarcsecond Interferometry) [5, 106] is a radio monitoring program for AGN south of declination -30 degrees. TANAMI particularly aims at the investigation of AGN jet structures. It provides simultaneous dual-frequency observations at 8.4 and 22 GHz (X- and K-band) using five telescopes of the LBA (Australia Long Baseline Array [107]) and further telescopes in South Africa, Antarctica, Chile and New Zealand (see figure 6.1). The data from these telescopes are combined to achieve a milliarcsecond resolution of the target sources using Very Long Baseline Interferometry (VLBI). Especially the morphology and dynamics of AGN jets can be observed by this technique (see figure 6.2 for the jets of Centaurus A). For examples of VLBI-images of BL Lacs and quasars see figure 6.3. VLBI imaging provides the possibility to measure jet properties like the speed, opening and inclination angle. From the 22 GHz images information from regions closer to the AGN core can be obtained. A combination of both frequencies provides spectral information.

Motivated by the launch of the *Fermi* satellite, the initial TANAMI sample is a hybrid of gamma-ray and radio motivated sources and comprises 24 quasars, 12 BL Lacs, 10 radio-galaxies and 3 unclassified sources (for the redshift distribution see figure 6.4). The optical classification was done using the Veron-Veron 12th edition catalogue (for references to catalogues see [108]). The radio-selected candidates were taken from the Stickel catalogue [109] with fluxes of $S_{5\text{GHz}} > 2$ Jy. The gamma-ray sample is made up by all EGRET (Energetic Gamma Ray Experiment Telescope, precursor of Fermi)

6.2 The TANAMI program and source candidate selection



Figure 6.1: Overview of the telescopes used for the TANAMI observations located in Australia, Antarctica, South America and South Africa (figure by M. Kadler [103] and J. Wilms [104]).

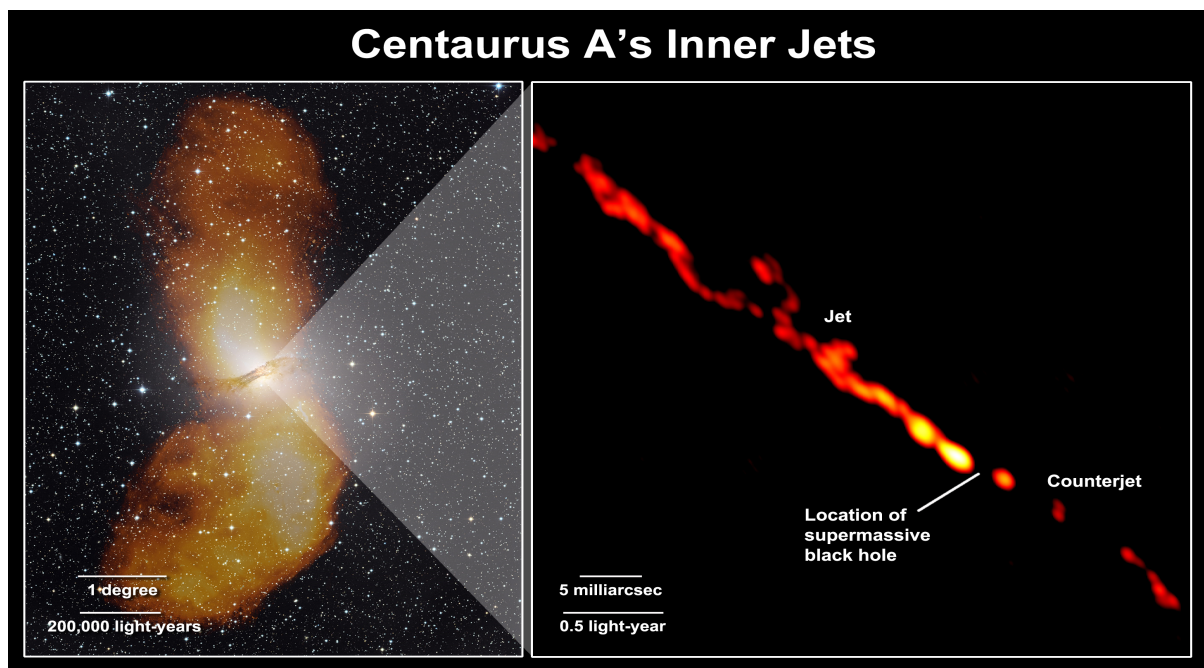


Figure 6.2: VLBI image of the inner jet structure of Centaurus A (figure from [105], [5]).

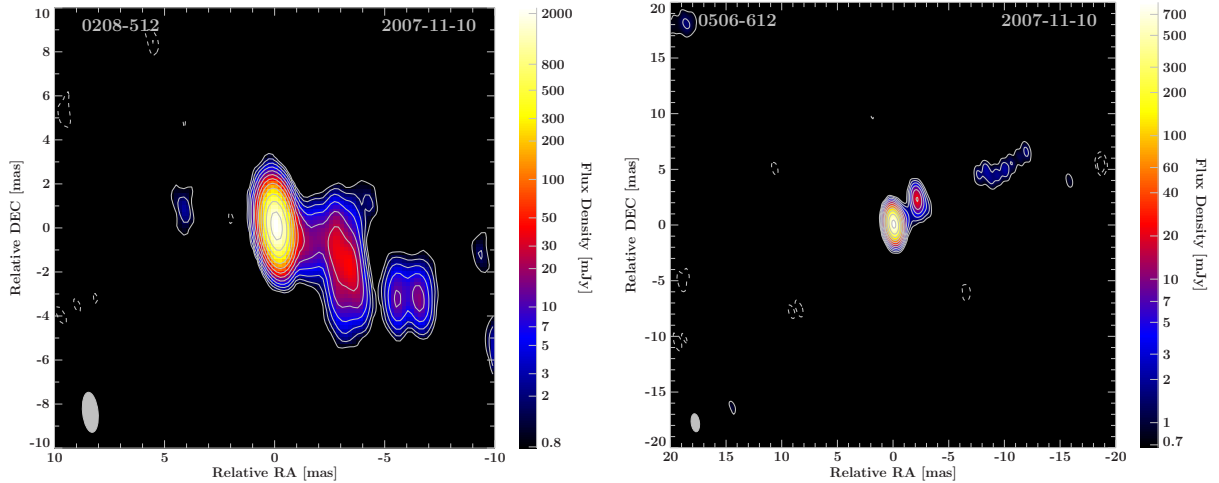


Figure 6.3: *Left:* VLBI-image of BL Lac 0208-512. *Right:* VLBI-image of quasar 0506-612. (RA/DEC)=(0,0) corresponds to the point of maximum intensity (pictures from [5], mas = milliarcseconds).

blazars in the declination range of observation. In the meantime several *Fermi*/LAT-detected sources have been added to the sample (see next section). At the moment 75 sources are under regular observation [6].

For TANAMI a multi-wavelength observation approach is used. This is done using observations of the *Swift* and *INTEGRAL* satellites in the UV/optical and X-ray regimes, respectively. Further radio observations with the Australia Telescope Compact Array (ATCA) and telescopes like Ceduna, Hobart and Effelsberg are implemented. The campaign is complemented by the search for neutrinos from TANAMI sources with the ANTARES neutrino telescope in the Mediterranean Sea (see chapter 4).

The TANAMI observation are carried out roughly every two months. The VLBI data, recorded on Long Baseline Array Disk Recorders, is correlated at the Curtin University of Perth and afterwards uploaded into a special image processing software for further analysis, fitting and calibration purposes. For further information on the TANAMI program refer to [5]. For the northern sky a similar project called MOJAVE (Monitoring Of Jets in Active galactic nuclei with VLBA Experiments) [110] is in operation.

6.2.2 Selected sources and observation period

The *Fermi* satellite (formerly known as *GLAST*) [7] was launched in June 2008 and is designed for a mission time of at least 5 years, while an operation up to 10 years is intended. Besides the Gamma-ray Burst Monitor (GBM) *Fermi* carries a powerful gamma-ray detector: The Large Area Telescope (LAT), which detects gamma-rays in the energy range from 20 MeV to 300 GeV. The field of view is large enough to scan the whole sky every three hours (20% of the sky is seen at any time). In order to reject the background from charged cosmic rays, the gamma-rays pass an anti-coincidence

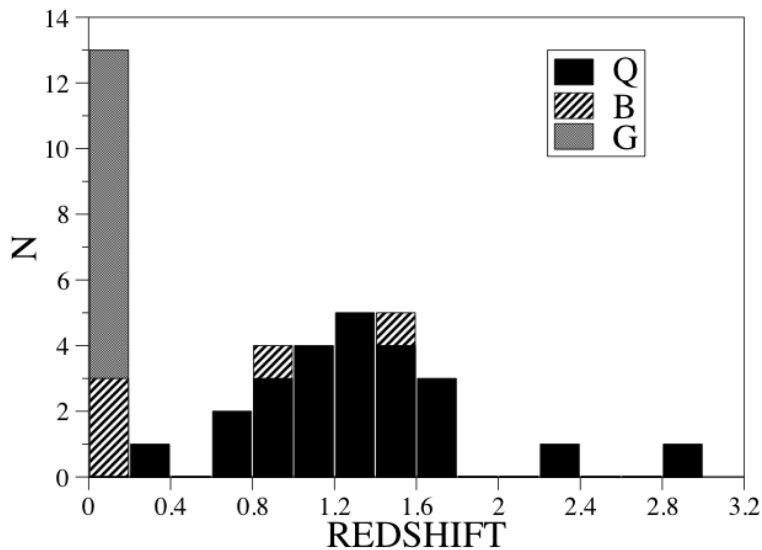


Figure 6.4: Redshift distribution of the initial TANAMI sample. Q = quasar, B = BL Lac, G = radio galaxy (figure from [106]).

detector. Gamma-rays are then detected via electron-positron pairs, which are created by interaction of the gamma-rays with conversion foils inside a silicon-strip tracker. After tracking, the electron-positron pairs enter a cesium-iodide calorimeter for energy measurement. The point-spread function for the angular reconstruction of on-axis events has a radius of 0.04 degrees at 100 GeV (1σ).

Regular *Fermi*/LAT observation started on 04.08.2008 and all-sky source catalogues have been published after 1 year (1FGL, [111]) and 2 years (2 FGL, [112]). As ANTARES was completed in summer 2008, the variability information from this list was used to select a subsample of TANAMI sources for this neutrino search. Since specific gamma-ray flare information (such as flare times and durations) is not taken into account explicitly for this neutrino analysis, the complete ANTARES data of 2009 is used. From the TANAMI sample 24 quasars and BL Lacs, which showed substantial gamma-ray variability, have been selected for this analysis. The criterion was a gamma-ray variability observed by the *Fermi*/LAT monitor. All sources shown in table 6.1 are marked as flaring (variability index) indicating a probability of below 1% being a steady source. The null hypothesis H_0 is a constant flux over the full two years. The variability index ($TS_{\text{var}} = \text{Test Statistics Variability}$) is calculated from the likelihood of flux values (from monthly binning) F_i by:

$$TS_{\text{var}} = 2[\log L(\{F_i\}) - \log L(F_{\text{const}})] = 2 \sum_i [\log L_i(F_i) - \log L_i(F_{\text{const}})]. \quad (6.1)$$

The likelihood for the full time range can be written as the sum over the individual time intervals (monthly binning). If H_0 is correct, TS is χ^2 distributed. At 99% confidence level the source is said to be variable if $TS_{\text{var}} > 41.6$ ($N_{\text{dof}} = 24 - 1$, 24

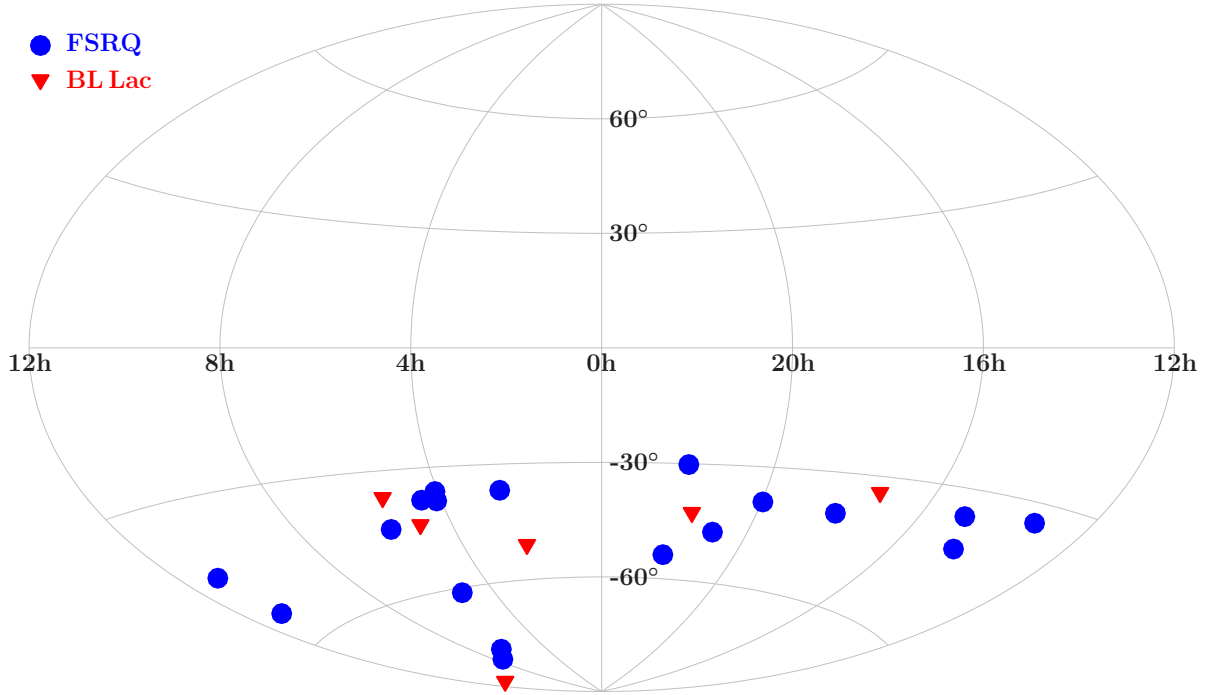


Figure 6.5: Skymap (Aitoff-projection) of the 24 selected sources: Quasars (full blue circles) and BL Lacs (full red triangles). TANAMI only observes sources below a declination of -30 degrees.

months in period, 41.6 is the 99% quantile of a χ^2 distribution for $N_{\text{dof}} = 23$). For further details on this procedure see [112]. Tables 6.1 and 6.2 contain the list of sources that have been selected for this and future analysis including all relevant information on coordinates and fluxes (see figure 6.5 for a skymap). A light curve of BL Lac object PKS0208-512 can be seen in figure 6.6. The variability index as function of the gamma flux is shown in figure 6.7.

6.3 AAFit-strategy, official data production and run selection

6.3.1 AAFit strategy and official data production

For event reconstruction two strategies are available in ANTARES: BBFit [114] and AAFit. Due to its optimization for a high angular resolution of muon track reconstruction, for this analysis the reconstructed particle tracks are obtained from the *AAFit-strategy version v0r7* throughout.

In the following the basic layout of the AAFit reconstruction chain is explained (for details see [115], figure 6.8 shows a flow chart of the AAFit-strategy.): First a linear prefit is performed based on the L1 hits of the event. It is assumed that all hits have been measured along the track. The fit is obtained by minimizing the χ^2 :

6.3 AAFit-strategy, official data production and run selection

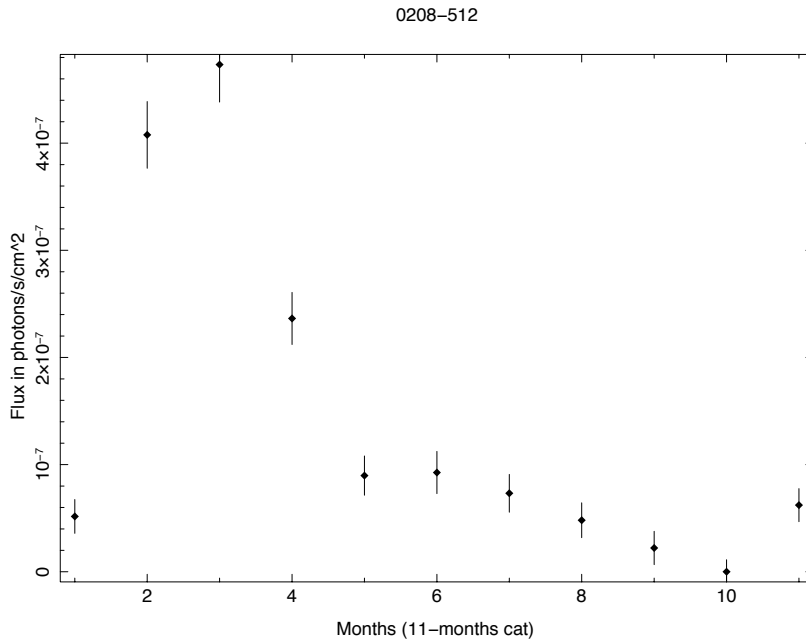


Figure 6.6: *Fermi* light curve for BL Lac object PKS0208-512 (J0210.7-5102). The observation started on 04.08.2008. As can be seen the object shows a flare in the first 2-3 months (figure from [7]).

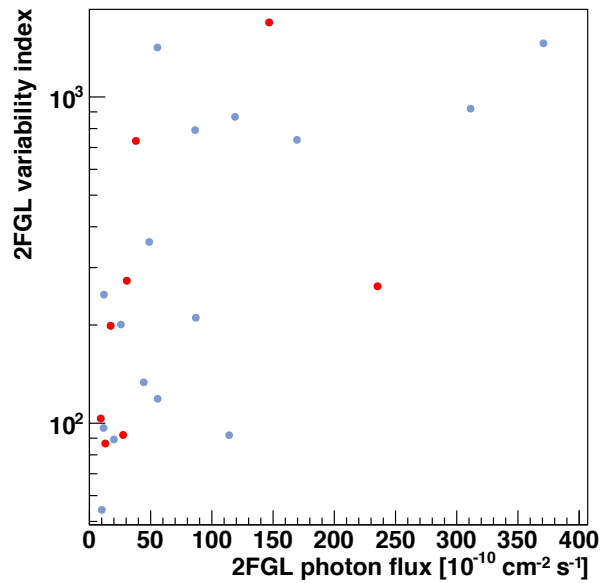


Figure 6.7: Variability versus average gamma flux for the 24 sources (see tables 6.1 and 6.2 for details). Sources marked in red are the unblinding candidates (see section 8).

6 Cluster search

id	name	LAT name	NED name	α	δ	T	$< 90^\circ$	TS_{var}
1	1714-336	J1717.7-3342	PMN J1717-3342	259.4	-33.70	BL	0.71	211
2	0521-365	J0523.0-3628	ESO 362-G021	80.74	-36.46	BL	0.74	359
3	2136-428	J2139.3-4236	PMN J2139-4235	324.85	-42.59	BL	0.82	119
4	0447-439	J0449.4-4350	PKS 0447-439	72.35	-43.84	BL	0.85	92
5*†	0208-512	J0210.7-5102	[HB89]0208-512	32.69	-51.02	BL	1.00	734
6*†	1057-797	J1057.0-8004	PKS 1057-79	164.68	-80.07	BL	1.00	92
7*†	2155-304	J2158.8-3013	[HB89] 2155-304	329.72	-30.23	Q	0.68	263
8	1313-333	J1315.9-3339	[HB89] 1313-333	199.03	-33.65	Q	0.71	201
9	1454-354	J1457.4-3540	PKS 1454-354	224.36	-35.65	Q	0.73	869
10	0402-362	J0403.9-3604	PKS 0402-362	60.97	-36.08	Q	0.74	1417
11	0227-369	J0229.3-3644	PKS 0227-369	37.37	-36.73	Q	0.74	248
12	0426-380	J0428.6-3756	PKS 0426-380	67.17	-37.94	Q	0.76	921
13	0405-385	J0407.3-3826	[HB89] 0405-385	61.75	-38.44	Q	0.76	89
14†	1954-388	J1958.2-3848	[HB89] 1954-388	299.50	-38.75	Q	0.77	273
15	1759-396	J1802.6-3940	PMN J1802-3940	270.68	-39.67	Q	0.78	739
16*†	1424-418	J1428.0-4206	[HB89] 1424-418	216.98	-42.11	Q	0.81	1692
17	0537-441	J0538.8-4405	[HB89] 0537-441	84.71	-44.09	Q	0.85	1460
18†	1104-445	J1107.2-4448	[HB89] 1104-445	166.79	-44.82	Q	0.87	103
19	2052-474	J2056.2-4715	[HB89] 2052-474	314.07	-47.25	Q	1.00	791
20	2204-540	J2208.1-5345	[HB89] 2204-540	331.93	-53.78	Q	1.00	97
21	1101-536	J1103.9-5356	PKS 1101-536	165.97	-53.95	Q	1.00	133
22*†	0506-612	J0507.5-6102	[HB89] 0506-612	76.68	-61.16	Q	1.00	87
23*†	0637-752	J0635.5-7516	[HB89] 0637-752	98.94	-75.27	Q	1.00	199
24	0736-770	J0734.2-7706	PKS 0736-770	113.68	-77.19	Q	1.00	54

Table 6.1: Source list ordered by type/declination. The next to last column (" $< 90^\circ$ ") indicates the fraction of the day the source is below the horizon (source below -47° are always visible). * = source used for simulation (6 sources). † = source used for unblinding request (8 sources). T = Type: BL = BL Lac, Q = Quasar, TS_{var} = variability index (see text), α = right ascension, δ = declination (both refer to equinox J2000). NED = NASA Extragalactic Database [113].

6.3 AAFit-strategy, official data production and run selection

id	name	a	LAT name	NED name	gamma flux	radio flux
1	1714-336	1	J1717.7-3342	PMN J1717-3342	8.689e-09	5.443e-01
2	0521-365	1	J0523.0-3628	ESO 362-G021	4.883e-09	1.517e+00
3	2136-428	1	J2139.3-4236	PMN J2139-4235	5.569e-09	0.0766e+00
4	0447-439	1	J0449.4-4350	PKS 0447-439	1.141e-08	6.868e-02
5*†	0208-512	1	J0210.7-5102	[HB89]0208-512	3.791e-09	1.385e+00
6*†	1057-797	0	J1057.1-8004	PKS 1057-79	2.754e-09	1.442e+00
7*†	2155-304	1	J2158.8-3013	[HB89] 2155-304	2.353e-08	3.826e-01
8	1313-333	1	J1315.9-3339	[HB89] 1313-333	2.568e-09	1.339e+00
9	1454-354	1	J1457.4-3540	PKS 1454-354	1.189e-08	6.981e-01
10	0402-362	1	J0403.9-3604	PKS 0402-362	5.552e-09	2.414e-01
11	0227-369	1	J0229.3-3644	PKS 0227-369	1.185e-09	3.763e-01
12	0426-380	1	J0428.6-3756	PKS 0426-380	3.113e-08	1.445e+00
13	0405-385	1	J0407.4-3826	[HB89] 0405-385	2.005e-09	1.382e+00
14†	1954-388	1	J1958.2-3848	[HB89] 1954-388	3.051e-09	1.566e+00
15	1759-396	1	J1802.6-3940	PMN J1802-3940	1.695e-08	8.931e-01
16*†	1424-418	1	J1428.0-4206	[HB89] 1424-418	1.468e-08	1.471e+00
17	0537-441	1	J0538.8-4405	[HB89] 0537-441	3.708e-08	4.706e+00
18†	1104-445	1	J1107.2-4448	[HB89] 1104-445	9.255e-10	1.410e+00
19	2052-474	1	J2056.2-4715	[HB89] 2052-474	8.630e-09	1.741e+00
20	2204-540	1	J2208.1-5345	[HB89] 2204-540	1.151e-09	7.093e-01
21	1101-536	1	J1103.9-5356	PKS 1101-536	4.440e-09	1.924e-01
22*†	0506-612	0	J0507.5-6102	[HB89] 0506-612	1.296e-09	1.120e+00
23*†	0637-752	1	J0635.5-7516	[HB89] 0637-752	1.730e-09	3.023e+00
24	0736-770	1	J0734.2-7706	PKS 0736-770	1.011e-09	0.232e+00

Table 6.2: Fluxes for sources in table 6.1. Average gamma flux (from 2FGL catalogue [112]) in photons per cm² and s in the range from 1-100 GeV. Radio flux in Jansky (1 Jy = 10⁻²⁶ W m⁻² Hz⁻¹). Source association a = 1/0: TANAMI source inside/not inside the 95% confidence region of the LAT source.

$$\chi^2 = \sum_i^N A_i (\mathbf{x}_i - \mathbf{x}_0 - \mathbf{v}t_i)^2. \quad (6.2)$$

A_i are the measured amplitudes of the N input hits. \mathbf{x}_i/t_i are the positions and times of the hits and \mathbf{x}_0 denotes the track position at $t = 0$. The track from the prefit is now shifted and tilted (nine times) and passed to the next two fits: The ‘‘M-Estimator’’ and the ‘‘original PDF-fit’’. For the M-estimator fit the function

$$M \approx \sum_i^N 2\sqrt{1 + t_{\text{res},i}^2/2} \quad (6.3)$$

is minimized, where $t_{\text{res},i}$ denotes the individual time residuals of the hits. The time residual is the difference between measured and expected time in nanoseconds: $t_{\text{res}} = t_{\text{measured}} - t_{\text{exp}}$. The expected time is calculated under the assumption of photon emission at the Cherenkov angle θ_C with respect to the track (for detailed derivation of this function see [115]).

The M-estimator is followed by a likelihood fit (original PDF-fit) using a probability density function (PDF), which only depends on time residuals. After repeating these two fits for all transformed pre-fits, the best one is taken and passed to the final PDF-fit that uses both amplitude information and information from background hits (obtained from Monte Carlo simulations). For the final PDF-fit all hits with time residuals in the range of ± 250 ns are added. The maximized likelihood L , the number of degrees of freedom n_{dof} and the number of prefits N_{prefit} closer than one degree to the final fit are used to calculate an empirical quality parameter Λ :

$$\Lambda = \frac{\log(L)}{n_{\text{dof}} - 0.1(N_{\text{prefit}} - 1)}. \quad (6.4)$$

Down-going atmospheric neutrinos, which are sometimes reconstructed as upward-going (for quantitative numbers see section on data-MC comparison), on average have a smaller value of Λ than true neutrino events and can therefore be discriminated (for illustration see figure 6.9).

In order to provide comparable sets of data for different ANTARES analyses, the raw data files are passed through a standard calibration and reconstruction chain implemented in the software framework SeaTray [98]. These so-called *data productions* are well documented and labeled and provide the reconstructed particle tracks from several reconstruction packages.

For this analysis the official ANTARES data production *exp reco_2011-05* based on the SeaTray release *searec 11-02-01* was used. The following summarizes some key facts of this production:

- For the detector positioning the alignment version *0.994* (see chapter 5 and appendix 10.8) was forced to be used throughout the production. No fallback to the trigger geometry is applied (see section 5.7). The latest PMT angular acceptance (*spring09*) is used [116].

6.3 AAFit-strategy, official data production and run selection

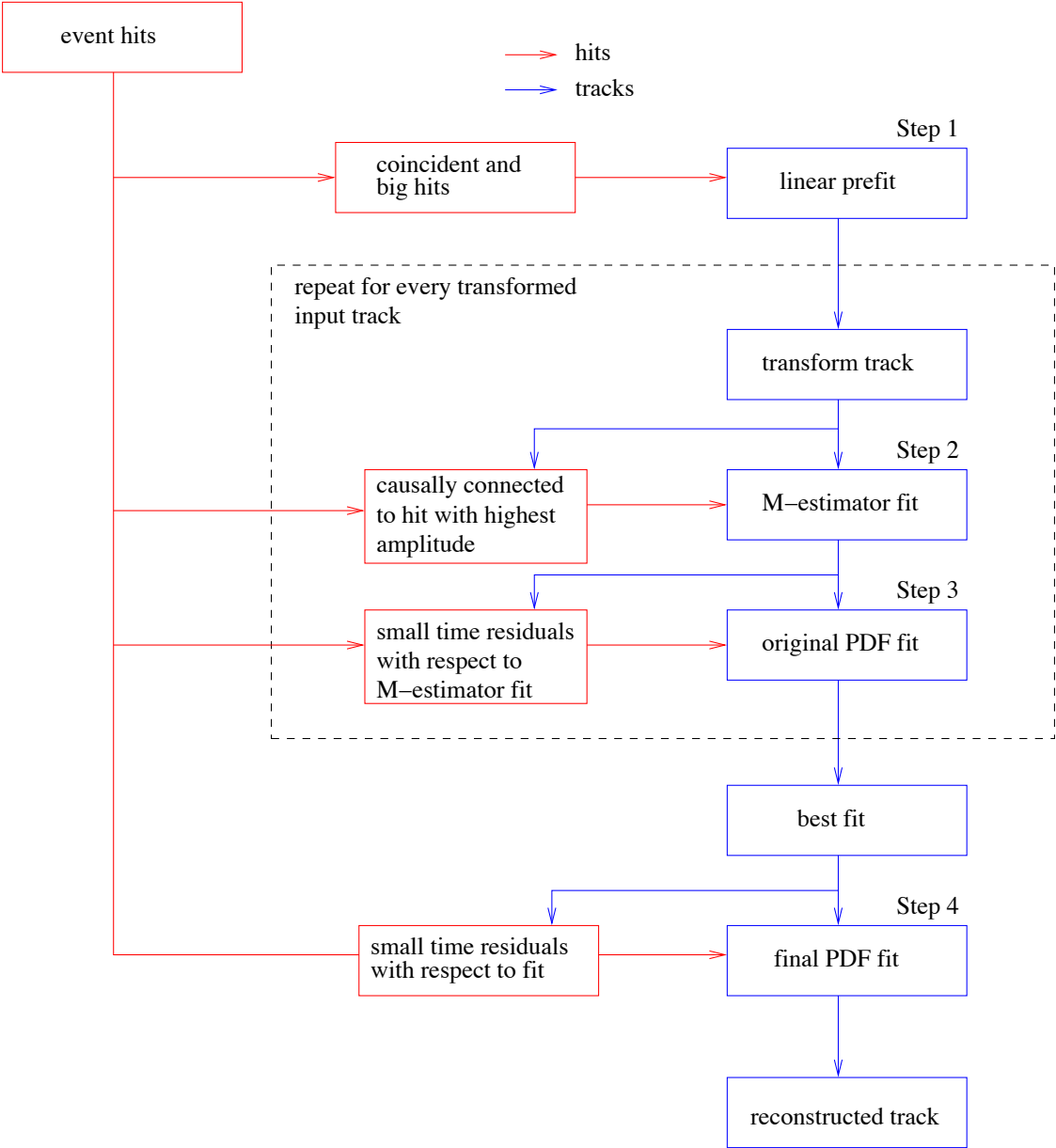


Figure 6.8: Flow chart of the “AAFit-strategy” (figure by Felix Fehr [117]).

- Calibration: The run-by-run offline-calibration was applied.
- Reconstructed events: The events used for this analysis have been reconstructed using the AAFit-strategy.
- In order to correlate events measured in the ANTARES local detector frame with astrophysical sources, the absolute event time of each track is necessary. This is computed from the run start time and the number of frames that have passed until the event in question. Therefore an exact knowledge of the run start time is needed (see appendix 10.4). The runs start time is obtained via the DAQ by a dedicated GPS-card. If this time is not available, the internal time of the Oracle database is used. The coordinate conversions from the ANTARES local system to the equatorial system are done with the *Astro* package (see appendix 10.6). *Astro* provides easy readable interface functions based on SLALIB-routines [118].

6.3.2 Run selection

The runs for this data production were selected via an official run list. The run list is generated by the use of a quality parameter $qb \in [1, 2, 3, 4]$. It is based on the number of Optical Modules operational, the average photomultiplier baseline rate and the number of bioluminescence bursts (burst-fraction, see section 3.5.2 for explanation):

- $qb = 1$: Basic selection, minimum requirement for a run to be included in an analysis.
- $qb = 2$: At least 80% of the OMs present at the time of the run, are operational.
- $qb = 3$: Baseline rate ≤ 120 kHz and burst fraction $\leq 40\%$.
- $qb = 4$: Baseline rate ≤ 120 kHz and burst fraction $\leq 20\%$.

The distribution of the maximum qb -flag of each run for this analysis can be seen in figure 6.10. For 2009 18 so-called “sparking runs” are excluded from the analysis. Within these runs at least one Optical Module shows a sparking behavior: Due to temporary failures in the PMT amplification chain, a PMT produces large numbers of unphysical hits (for illustration see figures in the Appendix). The excluded runs have a lifetime of 1.52 days (for run numbers see appendix).

To use the maximum amount of data is used, the runs were required to fulfill at least $qb = 1$. In order to exclude special runs for testing and calibration, the selection is based on a physics flag ($=1$); runs with setup comment “Saclay”, “OFF”, “PRELIM”, “SCAN” and “LED” were excluded. Following this selection 1587 runs with a total lifetime of 202.985 days were taken into account (a complete list of run numbers can be found in the appendix 10.1).

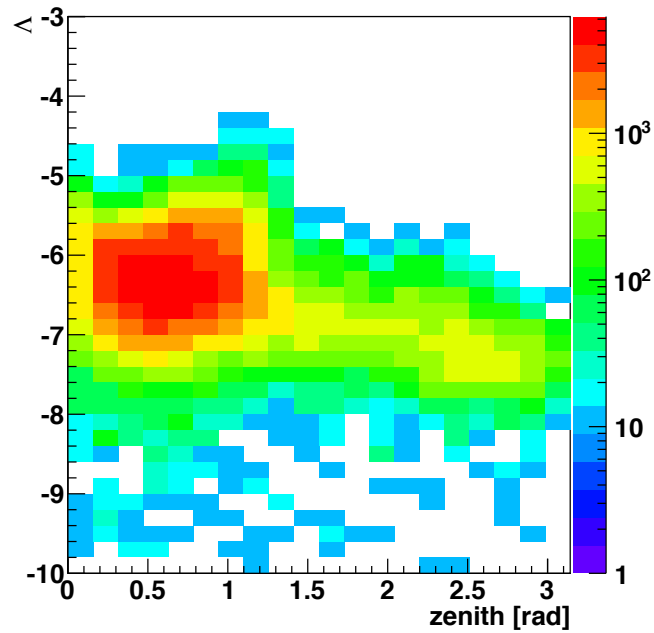


Figure 6.9: Quality parameter Λ as function of reconstructed zenith angle for down-going MC-muons. As can be seen these muons are sometimes mis-reconstructed as upward-going (zenith $> \frac{\pi}{2}$), but have small values of Λ in these cases.

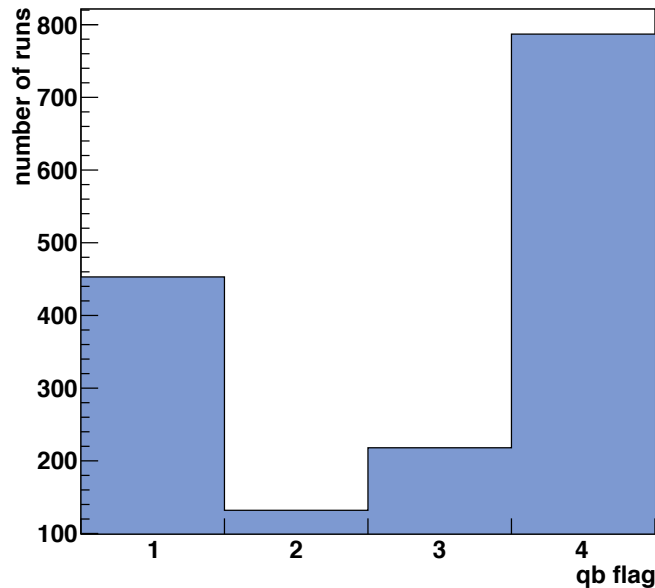


Figure 6.10: Distribution of maximum quality flag $qb \in [1, 2, 3, 4]$ for the selected sample of runs in 2009. For details see text.

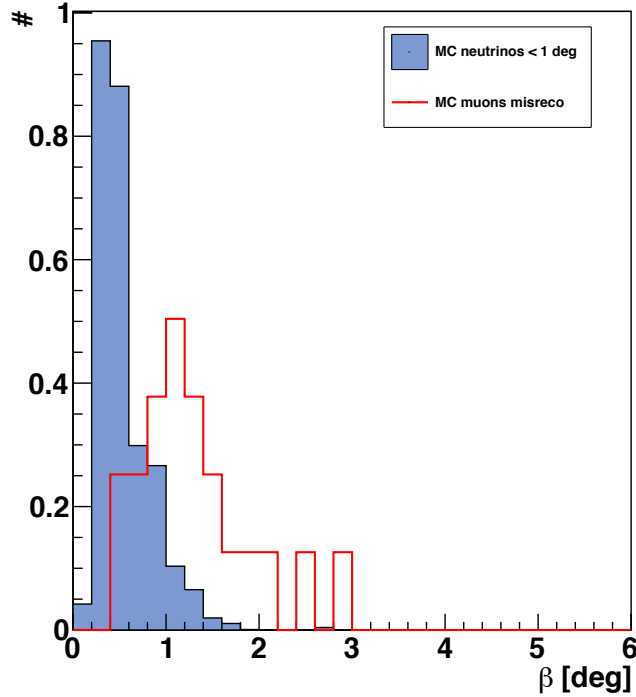


Figure 6.11: β -Distribution of both MC atmospheric neutrinos reconstructed better than one degree from the source (blue) and mis-reconstructed atmospheric muons (red). Cut $\beta < 1^\circ$: loose 18% of ν , get rid of 81% of mis-reconstructed muons. Cut $\beta < 0.8^\circ$: loose 29% of ν , get rid of 90% of mis-reconstructed muons.

6.4 Selection of signal events

The events from the data production are selected using both cuts on track fit quality parameters (Λ , β , for explanation see below) and on the reconstructed zenith angle θ . The following cuts were applied:

- *Track fit quality*: The cut on the quality parameter Λ from the AAFit-strategy is optimized: $\Lambda > \Lambda_{\text{cut}}$, $\Lambda_{\text{cut}} \in \{-5.4, -5.2, -5.0\}$.
- *Track fit quality*: In order to get rid of mis-reconstructed (a particle traveling downwards through the detector and is reconstructed as upward-going is called mis-reconstructed) atmospheric muons a cut on the direction error β can be applied:

$$\beta = \sqrt{\sigma_\theta^2 + \sigma_\phi^2 \sin^2(\theta)}.$$

β is composed from the fitted zenith angle θ and the errors on zenith and azimuth σ_θ , σ_ϕ . Figure 6.11 shows the effect of a β -cut on the number of mis-reconstructed

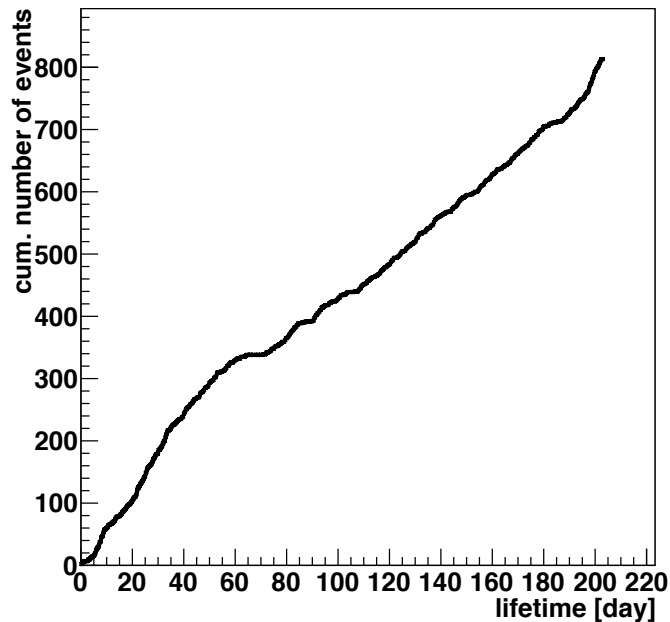


Figure 6.12: Cumulative number of up-going events ($\Lambda > -5.2$) as function of lifetime in 2009 (total lifetime: 202.985 days). As can be seen there are rate variation within the observation range.

muons and signal events. Throughout this analysis a cut on $\beta < 1^\circ$ has been chosen.

- *Reconstructed zenith angle:* Up-going events are selected by cutting on the zenith angle: $\theta > \frac{\pi}{2}$.

Table 6.3 shows the number of events selected from the data of 2009 as function of the Λ -cut ($\theta > \frac{\pi}{2}$, $\beta < 1^\circ$). Figure 6.12 shows the cumulative number of up-going events as function of lifetime. As can be seen rate variations are observed.

Λ -cut	events
-5.4	1451
-5.2	822
-5.0	534

Table 6.3: Number of up-going events (AAFit-tracks) as function of Λ -cut.

6.5 Scrambled skymaps from data

For the evaluation of analysis and search method a Monte Carlo simulation of a source in the sky and the background measured by the telescope are needed. For this anal-

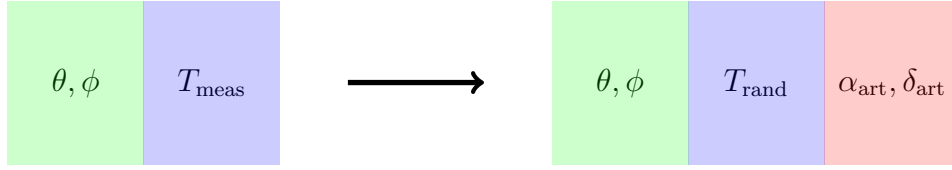


Figure 6.13: Generation of scrambled artificial background maps ($\alpha_{\text{art}}, \delta_{\text{art}}$) from events measured in the local ANTARES frame (θ, ϕ) by replacing the measured event time T_{meas} by a random time T_{rand} .

ysis the latter information is directly taken from the data by scrambling the events. Scrambled background-only skymaps are generated by assigning new random times to the events measured in data (see figure 6.13). The times are chosen to be within the observation time, i.e. during one of the selected runs, since the time information of these events is used for the clustering algorithm later. As the actually measured event times are discarded, this provides a fully blinded event sample. From the local coordinates and the new event times, right ascension and declination are calculated using the Astro coordinate conversion package (for an example of scrambled skymap see figure 6.14). The new times are uniformly generated and later correlated with the run structure (see appendix 10.5). For cross-checks of the applied scrambling method, figure 6.15 shows the distribution of the right ascension of the events in 100 scrambled skymaps. As can be seen its shape is flat.

6.6 Comparison of data and Monte Carlo

Since for this analysis the background estimation is done using real data, quantitative crosschecks with Monte Carlo simulations are necessary.

6.6.1 Run-by-run Monte Carlo

In order to reproduce the current detector status (i.e. disconnected lines, inoperational Optical Modules, HV- and threshold-settings at the PMTs) and the background conditions from ^{40}K -events and bioluminescence at the time of data taking, a *run-by-run Monte Carlo simulation* is available in ANTARES. For this purpose, the required information on the detector status and the environmental conditions are extracted from the data file of the given run. For each ANTARES run three dedicated files for the corresponding Monte Carlo simulation are produced: One for down-going atmospheric muon events and two for neutrino and anti-neutrino events. For this analysis run-by-run Monte Carlo version *v0.1.1* has been used.

6.6.2 Monte Carlo simulation chain

In this section the simulation chain including the various parameters that were used for the production of atmospheric muons and neutrinos for the run-by-run Monte Carlo

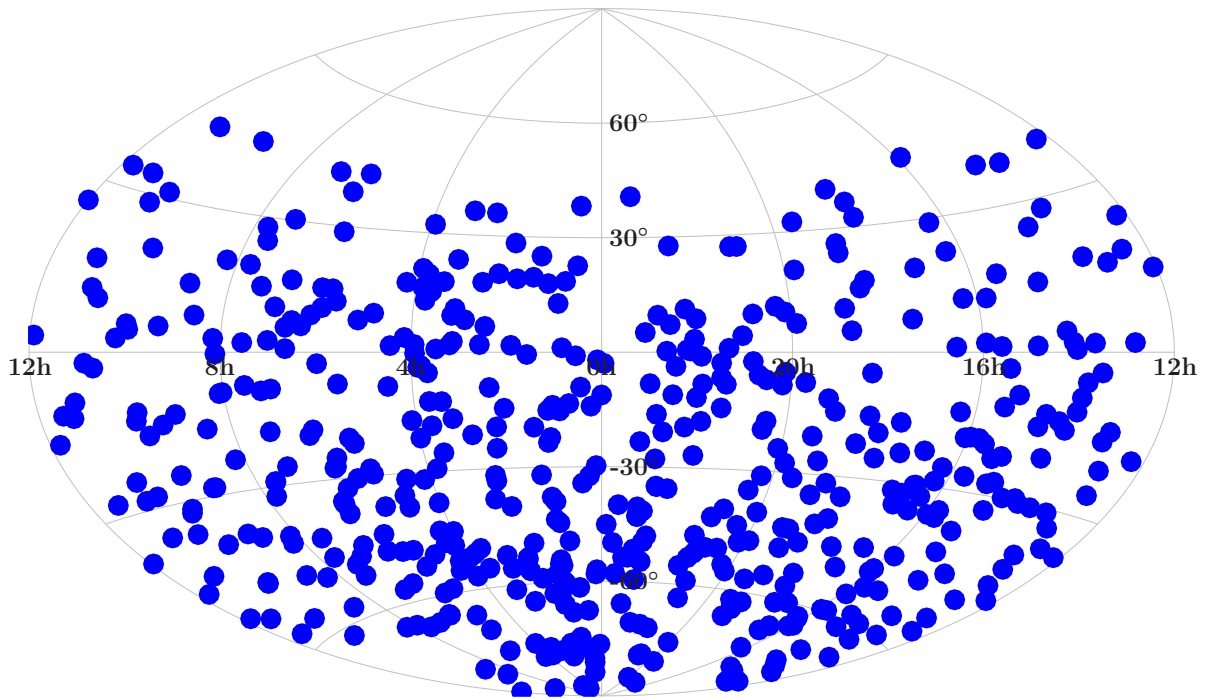


Figure 6.14: Example of a scrambled skymap (Aitoff-projection) of 534 time-scrambled real data events (see table 6.3).

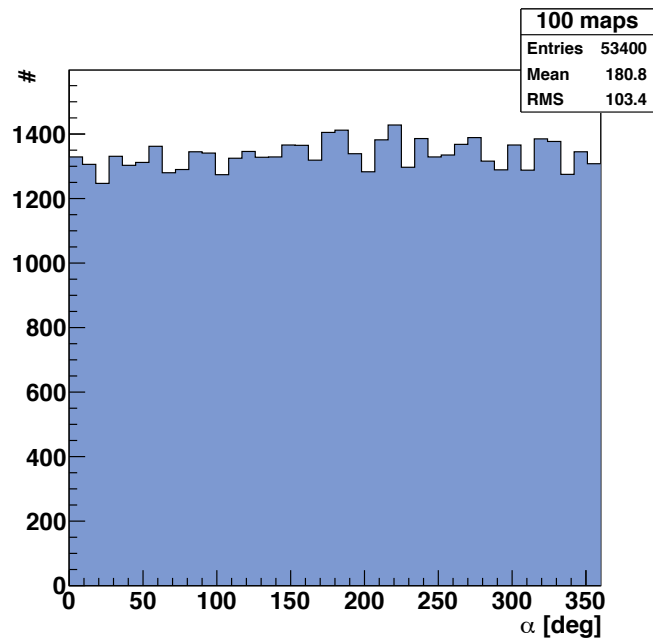


Figure 6.15: Right ascension (α) distribution for 100 scrambled skymaps of 534 events each.

is described. The simulation of dedicated point sources in the sky is explained in section 6.8.1. The simulation chain is composed of the following components (in order of application):

1. *Simulation of atmospheric muons:* For this topic *mupage* (atmospheric muons from parametric formulas: a fast generator for neutrino telescopes) v3r5 [119] has been developed, which is able to simulate not only single muons but also muon bundles from cosmic ray interactions. The maximum muon multiplicity is 200. The scaling to the correct lifetime of the run in question is obtained from an external file, where the effective lifetimes of all runs have been calculated via the number of frames N_F and the frame duration T_F (typically $104 \mu s$): $N_F \cdot T_F$. The output of *mupage* contains the kinematics of the simulated particle on the surface of an imaginary volume (called “can”) around the detector. The code is able to simulate muons and muon bundles up to $\theta = 85^\circ$ at depths in the range of 1.5 to 5.0 km w.e (kilometre water equivalent). For ANTARES the can (a cylinder) has the dimensions of $R_{\text{can}} = 238.611 \text{ m}$ and $H_{\text{can}} = 592.122 \text{ m}$. The minimum muon energy is 0.02 TeV. The mean density of the detection medium water is 1.03 g/cm^{-3} .
2. *Simulation of atmospheric neutrinos:* For this topic *genhen* v6r3 [120] is used. The neutrinos ($5 \cdot 10^8$) are simulated in an energy range from 100 - 10^8 GeV with a spectral index of $\alpha = 1.4$. Only muon neutrinos and CC interactions are simulated. The muon propagation including multiple scattering is done by the *mum* code.
3. *Simulation of ANTARES response to high energy muons:* For this topic *km3* [121] is has been developed. As tracking of large numbers of single Cherenkov photons is not possible on reasonable time scales, *km3* uses so-called “photon tables”, where the information on PMT hits from muon tracks at different distance and angles with respect to the detector have been saved. The L0-threshold is fixed and set to 0.4 photo-electrons. The L1-threshold is obtained from the database for each run separately.
4. *Simulation of showers:* For this topic *geasim* v4r10 [122] based on GEANT 3.21 [123] is used.
5. *Generation of MC events:* The MonteCarloEventWriter builds MC events from the detector simulation output of the previous steps and stores the information in ROOT-format for triggering.
6. *Trigger events/electronics smearing/background simulation:* For this topic the software *Trigger Efficiency* (TE) is used [124]. TE can run several triggers simultaneously, ARS setting and photomultiplier specifications can be set individually. TE is further able to take into account the current detector status (e.g. non working OMs, XOFFs and missing frames for example). Background hits from K40 and bioluminescence are generated using the measured single rates of

the PMTs. Afterpulses are also simulated. The functionality of TE is essential for producing a run-by-run MC and reproducing the detector status at the time of data taking.

After these steps the events are passed through the standard ANTARES reconstruction chain as described in the previous sections. In order to improve the data-MC agreement, the MC hit time gain a time smearing of 2 ns (for further details see [125]). From then on real data and Monte Carlo data can be treated on equal footing.

6.6.3 Event weighting

In order to compare measured data and data from Monte Carlo simulations, the MC events both for atmospheric muons and neutrinos have to be weighted correctly. In order to save computing time, atmospheric muons events have been generated with 1/10 of the whole statistics in version v0.1.1 of the run-by-run MC, therefore a weight w_μ of 10 must be applied for each MC-muon:

$$w_\mu = 10. \quad (6.5)$$

For atmospheric neutrinos the weight w_ν is calculated as follows:

$$w_\nu = (w3/N_{\text{gen}}) \cdot T_{\text{run}}, \quad (6.6)$$

$$w3 = w2 \cdot \Phi, \quad (6.7)$$

$$w2 = S \cdot I_\theta \cdot I_E \cdot E^\gamma \cdot F, \quad (6.8)$$

where N_{gen} is the number of generated events and T_{run} is the run duration (irradiation time, expressed as a fraction of a year). γ is the spectral index. The run duration has been computed from the number of frames and the frame duration. $w3$ is the so-called global weight, $w2$ the generation weight and Φ the differential flux of muons at the detector in $\text{GeV}^{-1} \cdot \text{m}^{-2} \cdot \text{sr}^{-1} \cdot \text{s}^{-1}$. I_θ is the angular phase-space factor, I_E the energy phase-space factor $(E_{\text{max}}^{1-\gamma} - E_{\text{min}}^{1-\gamma})/(1-\gamma)$, E^γ takes into account the flat energy generation and F is the number of seconds per year. S is the effective can surface. Further information can be found in [126, 127]. For the plots shown in the next section the weights (w_μ , w_ν) are applied.

6.6.4 Results and conclusion

For comparison a sample of ≈ 1560 runs from the run-by-run Monte Carlo production has been used. Due to software incompatibilities some runs of the 2009 real data runs have no corresponding Monte Carlo simulation and have been discarded.

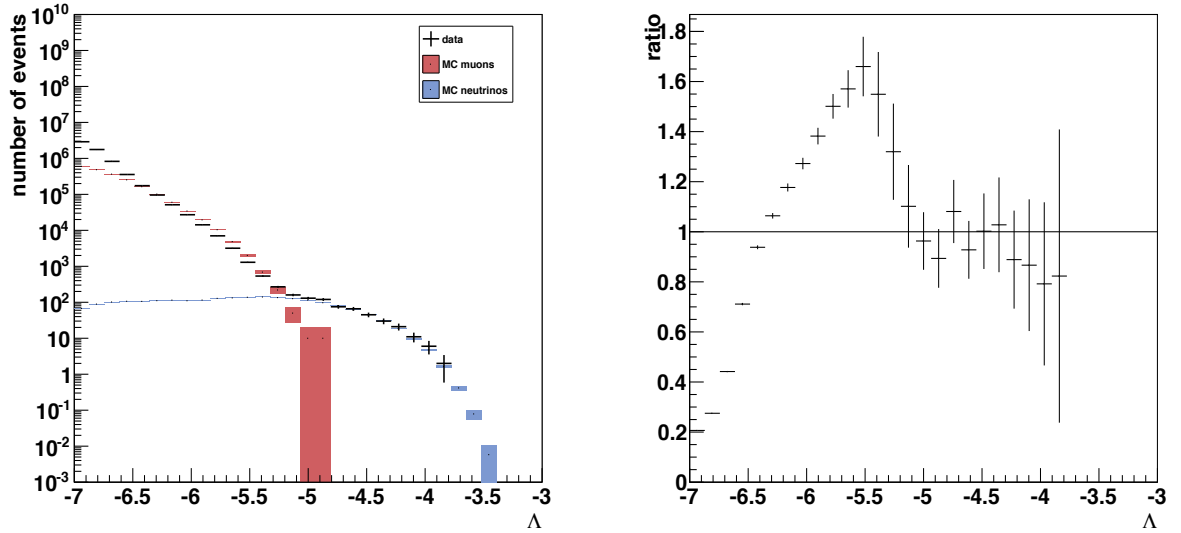


Figure 6.16: *Left*: Lambda distribution of up-going events (cut at 90°). *Right*: Ratio plot of $(\text{MC-muon} + \text{MC-neutrino})/\text{data}$.

Distribution of quality parameter Λ

The total number of selected events from the data is mainly determined by the cut on the reconstruction quality parameter Λ . The distribution of the quality parameter Λ for up-going events with a cut on zenith angle at 90° can be seen in figure 6.16. There is large disagreement for small values of $\Lambda \lesssim -6.5$, where the events are mainly dominated by down-going muons mis-reconstructed as upward-going (see figure 6.9). For the final event selection a cut on $\Lambda > -5.4$ or tighter are applied. In this regime data and Monte Carlo agrees well within the statistical errors. However there is not 100% agreement even at large values of Λ .

Angular distribution of events

For the angular distributions of events both effects from the Earth's atmosphere and from the special detector geometry are crucial inputs. Figures 6.17, 6.18 and 6.19 show the azimuth and zenith distributions of up-going events after applying different quality cuts. From these plots the fraction of mis-reconstructed muons can be obtained. For a cut of $\Lambda > -5.4$ 40% mis-reconstructed muons are still present. At $\Lambda > -5.2$ a 10% fraction of mis-reconstructed muons survives.

Conclusion

As can be seen from the given plots, data and Monte Carlo agree quite well. Taking into account the variable status of the over 800 photomultiplier by taking care of environmental conditions improved the situation a lot. However there are still improvements possible and on the way to be implemented (OM angular acceptance (see [116]),

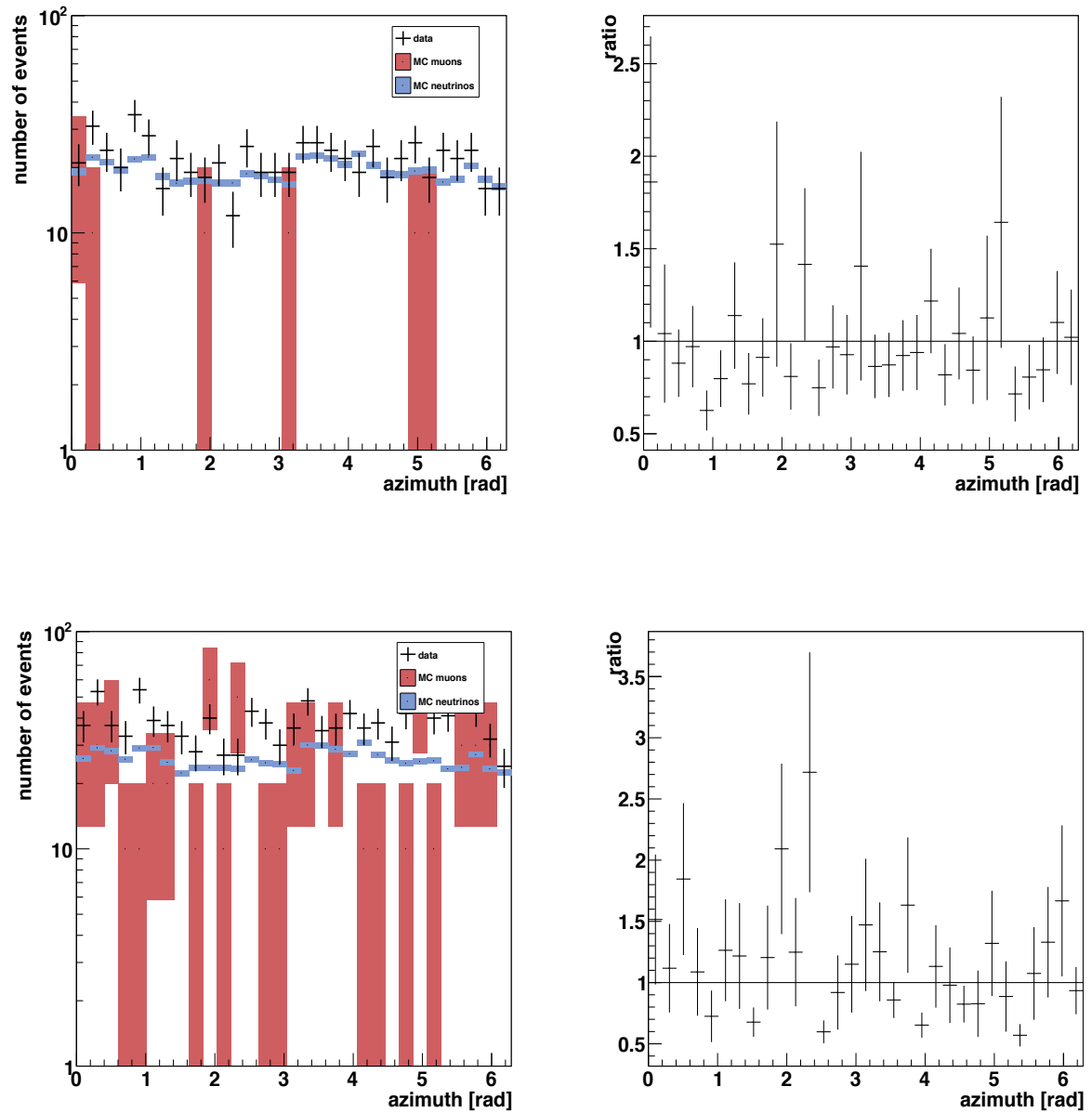


Figure 6.17: *Left:* Azimuth distribution of events with $\Lambda > -5.2$ (upper panel), $\Lambda > -5.4$ (lower panel). *Right:* Ratio plot of (MC-muon + MC-neutrino)/data.

6 Cluster search

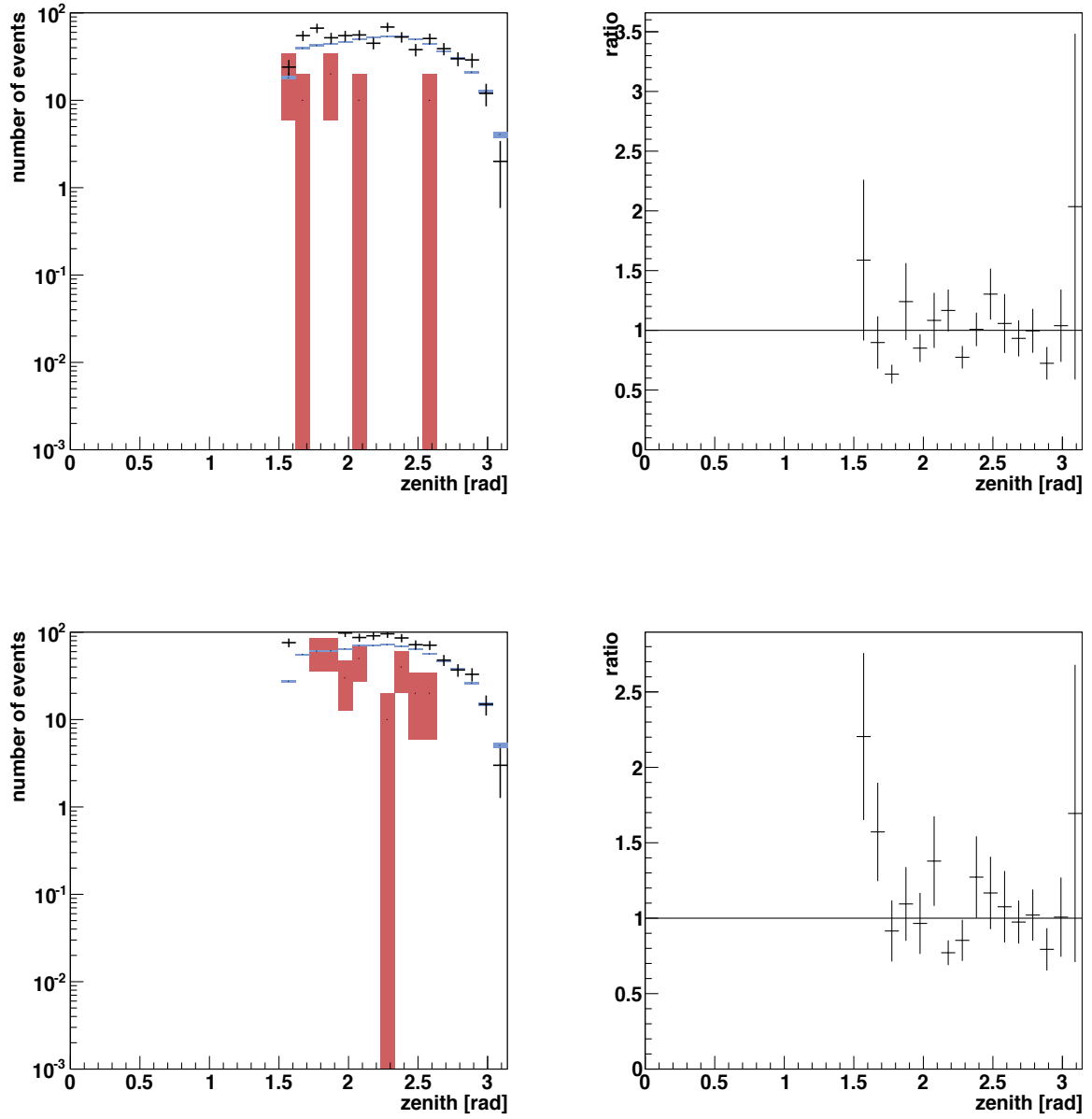


Figure 6.18: *Left:* Zenith distribution of events with $\Lambda > -5.2$ (upper panel), $\Lambda > -5.4$ (lower panel). *Right:* Ratio plot of (MC-muon + MC-neutrino)/data.

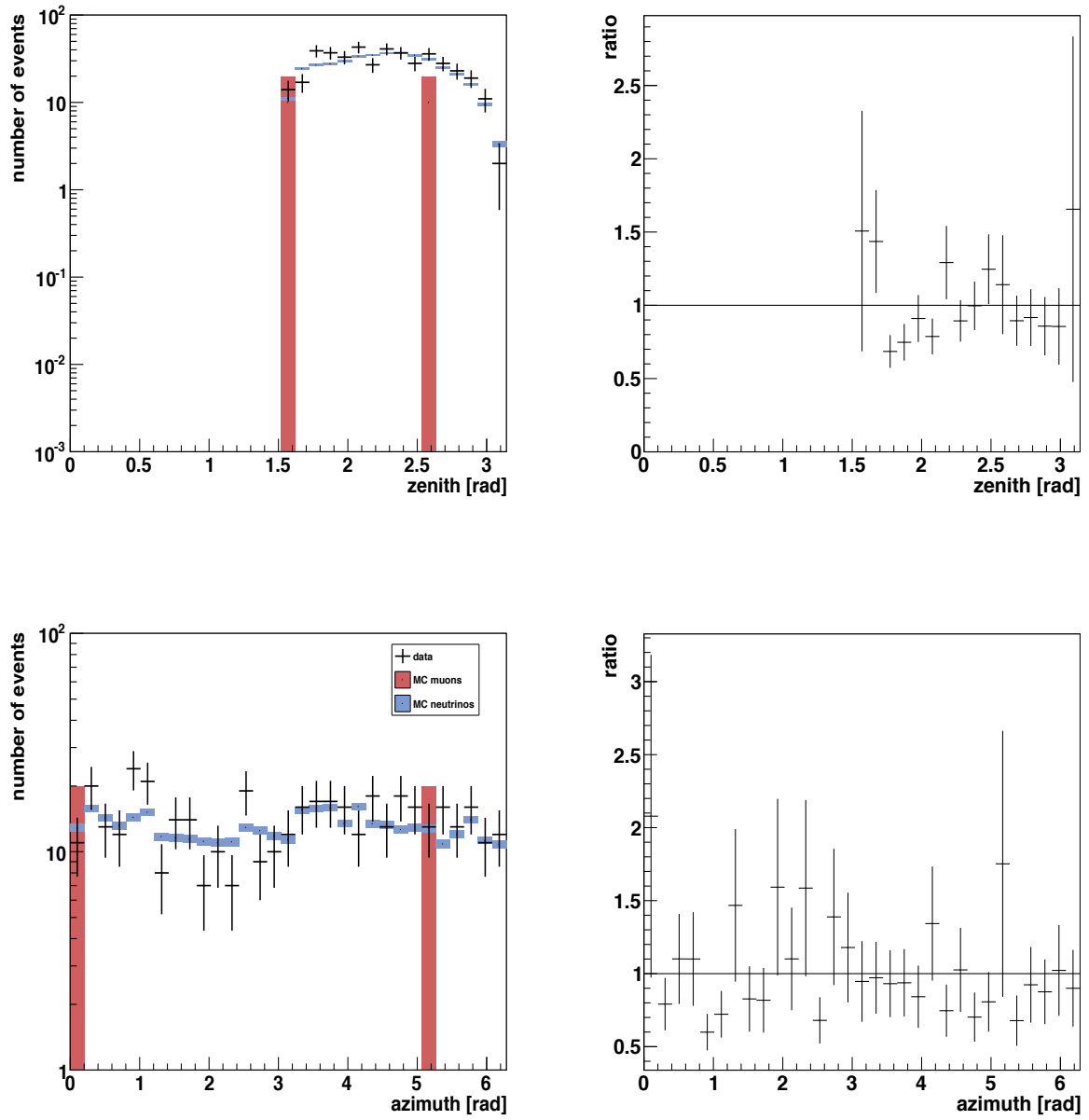


Figure 6.19: *Left: Left:* Zenith distribution of events with $\Lambda > -5.0$ (upper panel), azimuth distribution $\Lambda > -5.0$ (lower panel). *Right:* Ratio plot of (MC-muon + MC-neutrino)/data.

thresholds, higher statistics for MUPAGE and software updates on the different simulation programs) in order to transfer the real detector conditions during data taking to the Monte Carlo simulation chain. For this reason the estimate of the background (see next section) will be based on real data rather than Monte Carlo events.

6.7 Background estimation

To quantify the probability and the significance of a possible detection, the combined rate of up-going background events from atmospheric neutrinos and from misreconstructed atmospheric muons (originally down-going) is required. This background rate is obtained from real data for this analysis. Two different approaches are possible:

1. Assume a constant rate over the whole year;
2. Take into account rate variations as function of time (see figure 6.12). Such variations can have different origins: variable ambient conditions (e.g. bioluminescence), variable detector sensitivity as a consequence of temporarily inoperational lines or sectors, seasonal variations in the atmospheric muon and neutrino flux [128].

In the following, a constant rate is assumed initially. The modifications resulting from taking account rate variations are elaborated subsequently.

6.7.1 Assuming a constant background rate

When assuming a constant rate for background events in time, the number of recorded events still depends on the local zenith and azimuth. Figure 6.20 shows the measured azimuth and zenith angle for up-going AAFit-events with $\Lambda > -5.4$. Further the source zenith and azimuth range depends on the source declination (see figures 6.21). To estimate the rate a large number of scrambled skymaps is generated. The number of events in cones of 0.25, 0.5, 1 and 2 degrees (half cone angle) around the source position are averaged. From the true visibility time of the source, taking into account the run coverage and the visibility below the horizon, the corresponding background rate is calculated.

6.8 Source flux simulation

6.8.1 Introduction and procedure

Before applying the analysis code to the data, it is essential to quantify the outcome by Monte Carlo simulation of an assumed source and test the code on blinded data. For this purpose, events coming from a source subsample of the full source list of the analysis have been simulated. The subsample has been chosen to be homogeneously

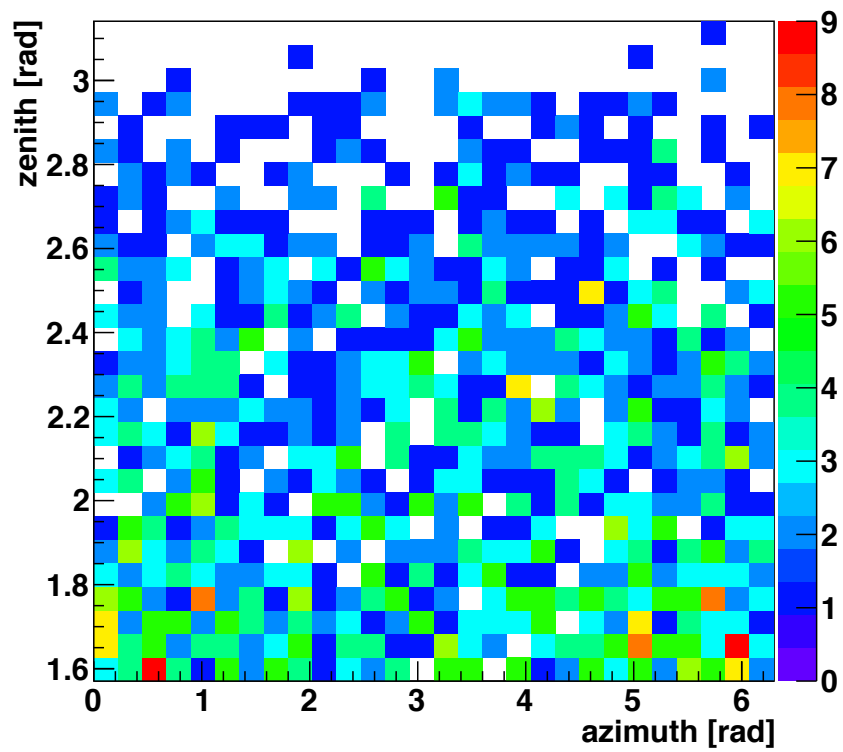


Figure 6.20: Zenith vs. azimuth of AAFit-tracks in 2009 reconstructed as up-going with $\Lambda > -5.4$.

6 Cluster search

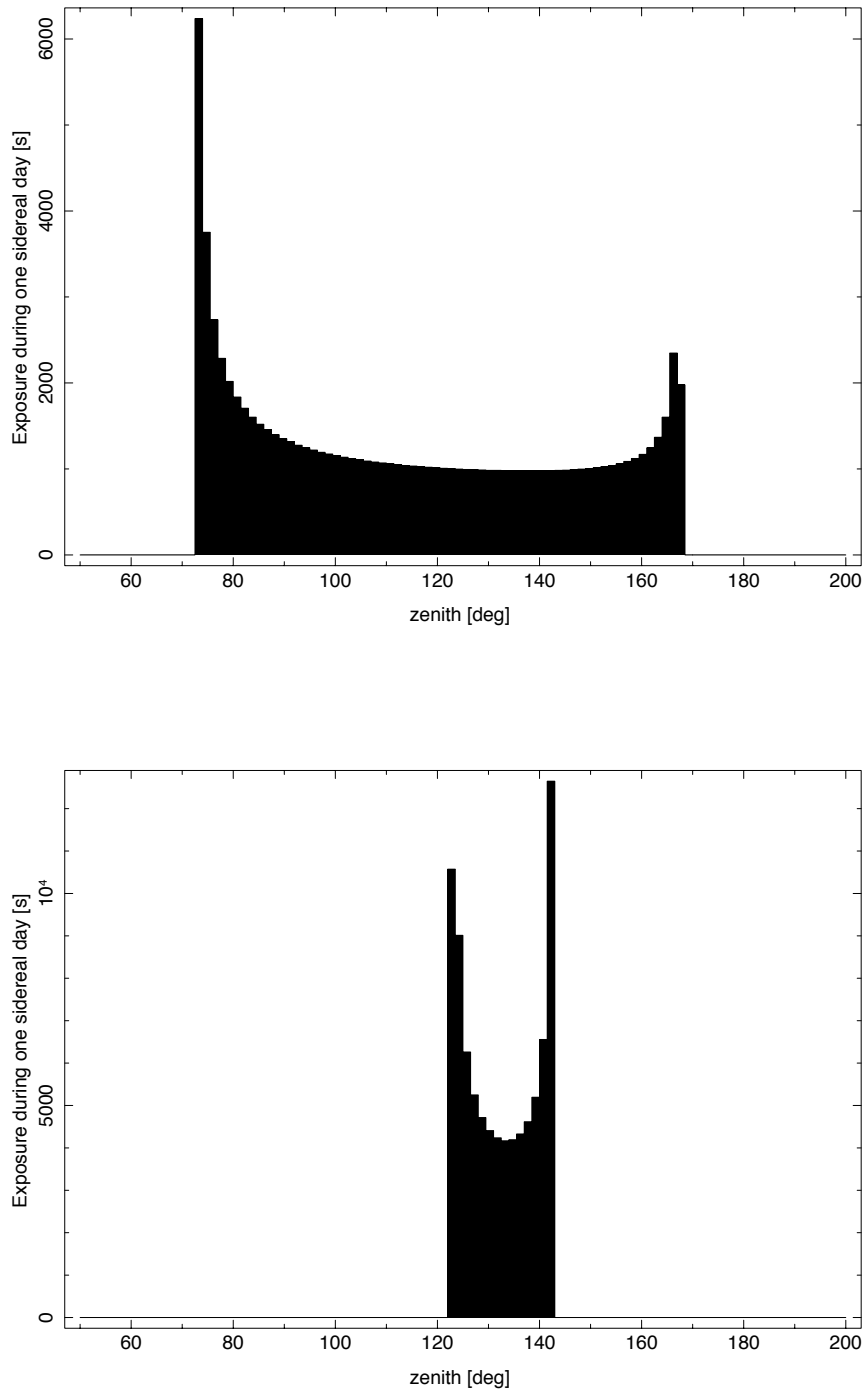


Figure 6.21: Distribution of source zenith angle at the ANTARES site. *Upper plot:* Zenith histogram of PKS2155-304 (declination -30 degrees) for one sidereal day. *Lower plot:* Zenith histogram of PKS1057-79 (declination -80 degrees) for one sidereal day. As can be seen, the zenith range for a particular source highly depends on the source declination. PKS2155-304 is invisible for parts of the day (zenith $< 90^\circ$).

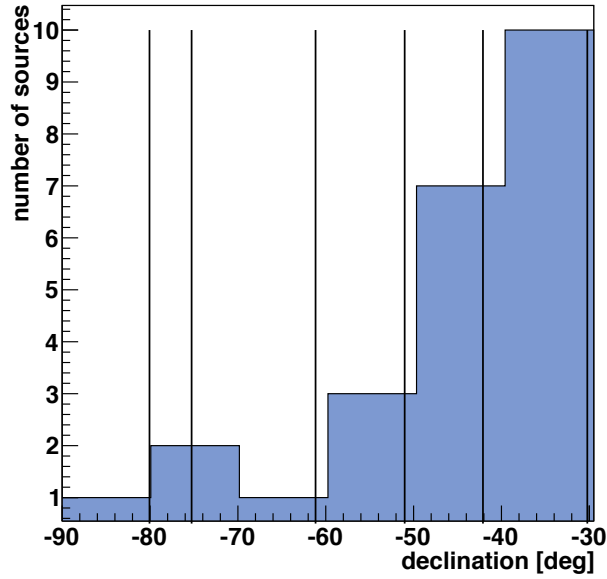


Figure 6.22: Distribution of the 24 source declinations from table 6.1 (blue histogram). The declinations of the six sources used for the simulation are marked by the black vertical lines.

spread over the declination range from -30 to -90 degrees (see figure 6.22 for distribution of source declinations). The six sources that have been chosen are listed in table 6.4. The neutrino fluxes are simulated according to a power law ($E^{-\alpha}$) neutrino flux with index $\alpha = 2$. All sensitivities, quoted in the following, correspond to this shape of the primary flux.

name	δ [deg]
2155-304	-30.23
1424-418	-42.11
0208-512	-51.02
0506-612	-61.16
0637-752	-75.27
1057-797	-80.07

Table 6.4: Subsample of sources for simulation (ordered by declination δ). For full source names and detailed information see table 6.1.

The source simulation procedure is divided into the following steps (for detailed information on the simulation programs see section on comparison between data and Monte Carlo):

1. Initially simulate events with an E^{-1} -spectrum from the source position using the neutrino simulator *genhen* in order to increase the statistics a high energies.

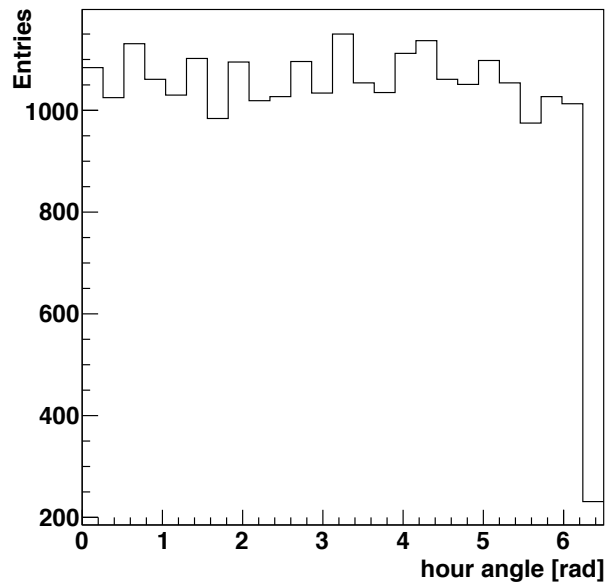


Figure 6.23: Distribution of the hour angle after running km3. A flat distribution can be seen.

2. Create the detector response (*km3*).
3. Reweight the events to an E^{-2} spectrum and assign an absolute event time according to the assumed flare duration and time (flare duration and time are discussed later in the results chapter).
4. Calculate the expected number of events (not necessarily an integer) in the detector as a function of the neutrino flux and the flare duration.
5. Use Poisson statistics to sample an integer number of signal events from the simulation proportional to the flare duration.
6. Run the reconstruction and apply cuts.
7. Repeat from step 5 and thus create multiple sets of source simulations.

These steps are discussed in more detail in the following.

6.8.2 Generating events, absolute event times and weights

Generating events

For the generation of events from a given source the standard ANTARES neutrino generator *genhen* was used. For the simulation of a point-source in the sky it can be operated in a so-called *point-source mode*, where the declination δ of the source can be specified by the user in the steering script by setting the appropriate parameters.

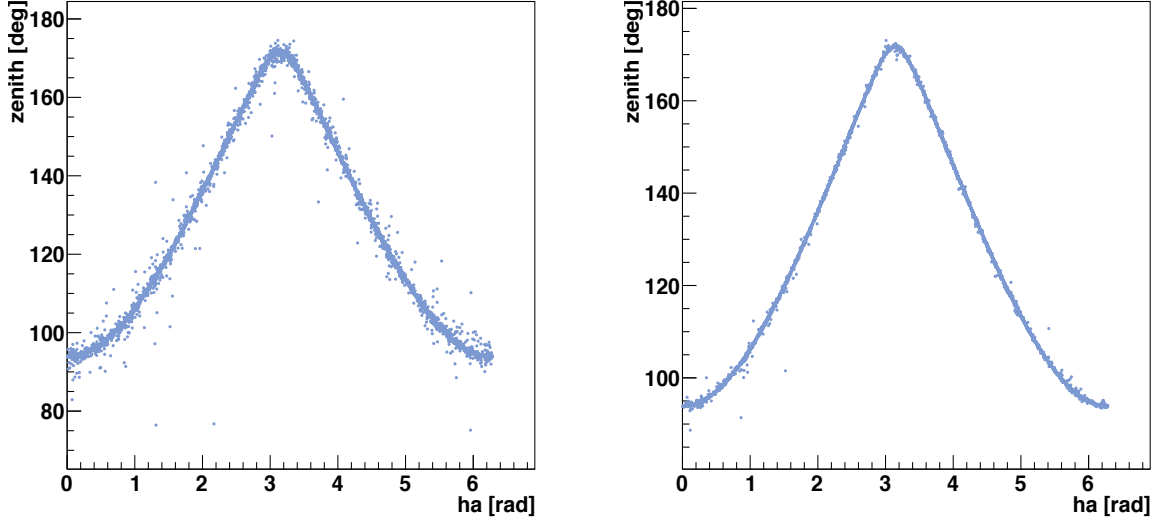


Figure 6.24: Simulation of events from PKS0208-512. *Left:* Zenith angle as function of hour angle (ha). *Right:* Zenith angle as function of hour angle with a muon energy cut of $E > 10^3$ GeV. As expected the spread of the curve decreases.

Absolute event times

Genhen generates a flat-distributed hour angle $ha \in [0; 2\pi]$ (see figure 6.23) or equivalently $ha \in [0; 24 h]$ for each event, which has the following connection to the right ascension α of the source:

$$ha = LST - \alpha. \quad (6.9)$$

LST is the local sidereal time. The hour angle indicates how much sidereal time has passed since the source was above the local meridian. From figure 6.24 the zenith as function of the hour angle can be seen. From the LST and the detector longitude (West) l_W one can obtain the Greenwich Standard Time (GST) using

$$GST = LST + \frac{l_W}{15^\circ/h}. \quad (6.10)$$

ANTARES is located at $l_W = -6.1657^\circ$. The GST is related to UT by

$$GST = G + 0.0657098244 \cdot d + 1.00273791 \cdot t, \quad (6.11)$$

where G is a year-dependent constant ($G_{2009} = 6.6527125$), d the day of the year and t the hour. Using all this, it is possible to calculate a UT for each event. For the simulation the day d is generated with a flat distribution within the corresponding time period of simulation.

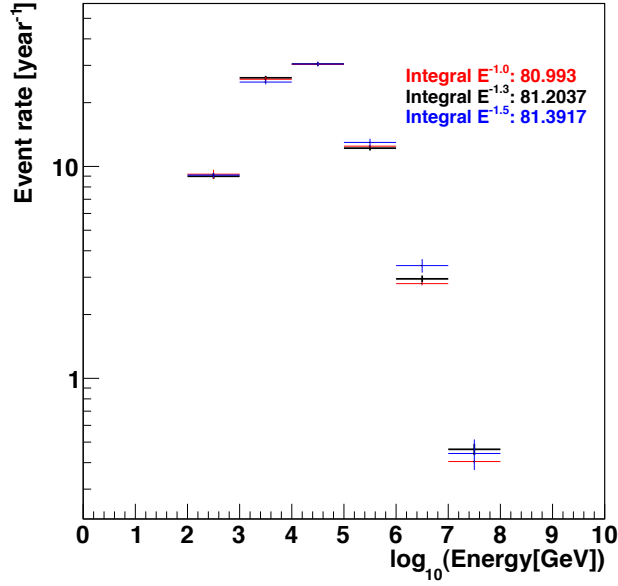


Figure 6.25: Energy distribution of simulated events re-weighted to a E^{-2} flux shape from different generation spectra with spectral indices $\alpha = 1.0, 1.3, 1.5$. As expected the statistical error is correlated with the spectral index.

Event weighting

In order to increase the statistics at high energies, the event generation is performed at a different spectral index than for the assumed true source spectrum. The generated events are reweighted afterwards. For checking self-consistency events with different spectral indices $\alpha = 1.0, 1.3, 1.5$ have been generated. After generation the events are reweighted (weight w) corresponding to an E^{-2} -flux as follows:

$$w = w_2 \cdot \Phi_{\text{new}} \cdot T_{\text{irr}} / N_{\text{gen}}. \quad (6.12)$$

w_2 is the generation weight (see equation 6.8), Φ_{new} the new flux, T_{irr} the irradiation time and N_{gen} the number of generated events. Φ_{new} has the following form:

$$E^2 \Phi_{\text{new}} = \mathcal{K} \quad [\mathcal{K}] = \text{GeV s}^{-1} \text{cm}^{-2}, \quad (6.13)$$

where \mathcal{K} is the flux normalization constant. The expected number of events as function of energy from a flux with $\mathcal{K} = 10^{-7} \text{GeV s}^{-1} \text{cm}^{-2}$ within one year lifetime in the ANTARES detector can be seen in figure 6.25. As expected the number of events is independent of the spectral index of the generation spectrum. For further purposes events generated with an spectral index of $\alpha = 1.0$ were used.

Figure 6.26 shows the zenith versus azimuth for simulated events (muons without reconstruction) from the source PKS0208-512 in local coordinates and a reference line for coordinate conversion checks (for cross-checks with Astro see appendix 10.6). As

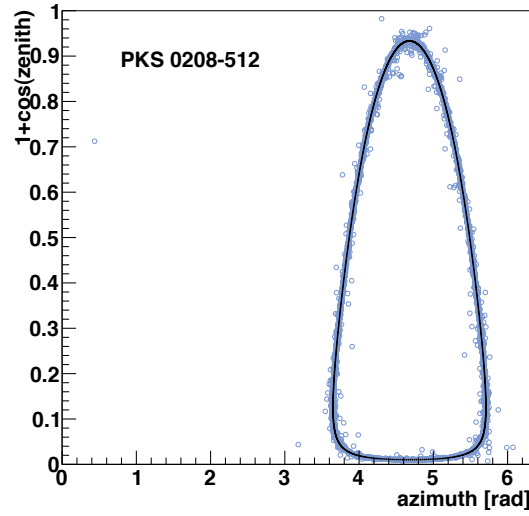


Figure 6.26: $(1+\cos(\theta))$ as function of azimuth for simulated events from PKS0208-512 (without reconstruction). The black curve shows the expectation from the ISIS coordination transformation tool. Both curves agree quite well. The spread of the events around the curve arises from the kinematic angle between neutrino and muon.

can be seen the events are perfectly arranged on or next to the black line. In local coordinates the source travels around this line once per sidereal day.

name	δ [deg]	events per year
2155	-30.22556	78.967
1424	-42.10528	80.929
0208	-51.01722	80.993
0506	-61.16139	82.787
0637	-75.27139	82.982
1057	-80.06504	84.230

Table 6.5: Number of expected events per year as function of source declination for flux constant $\mathcal{K} = 10^{-7}$. Due to the sensitivity zenith-dependence the number of expected events rises for sources at lower declinations.

6.8.3 Sampling events

From the generated MC-events a subsample of N events is taken in such a way that the probability for picking an event is proportional to its weight w . In order to quantify and evaluate different signal strength, the simulation has been performed for each

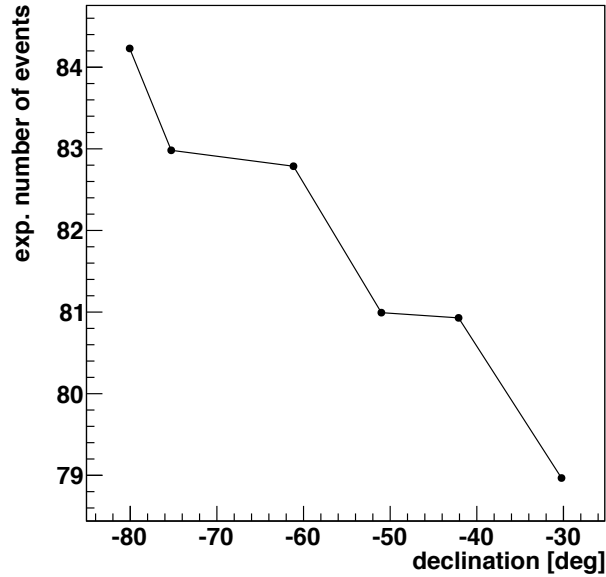


Figure 6.27: Number of expected events per year in ANTARES as function of source declination (6 sources) for a flux constant of 10^{-7} .

source using a set of flux constants \mathcal{K} . The mean number of sampled events N is obtained by Poisson statistics from the number of expected events. Table 6.5 contains the expected event numbers as function of source declination for the flux constant 10^{-7} (see also figure 6.27).

6.8.4 Reconstruction, injection and source association

In order to be able to insert the events from the source simulation into scrambled background maps, they are reconstructed using the AAFit-strategy (see Section 6.3). After applying cuts on the reconstruction quality parameters β and Λ and the zenith angle of the event, they can be merged with scrambled background skymaps from real data. As the goal of this work is the evaluation of time clustered event detection, the assignment of an absolute event time ensures an equal treatment of Monte Carlo and data events. The events are associate with a source, if the angle between the source and the reconstructed track is below a given threshold (typically around 1 degree).

6.9 Clustering

As the goal of this work is to search for time-clustered events from a given source, a dedicated piece of software has been developed that provides full event handling, from reading the eventfile up to the calculation of statistical parameters attributed

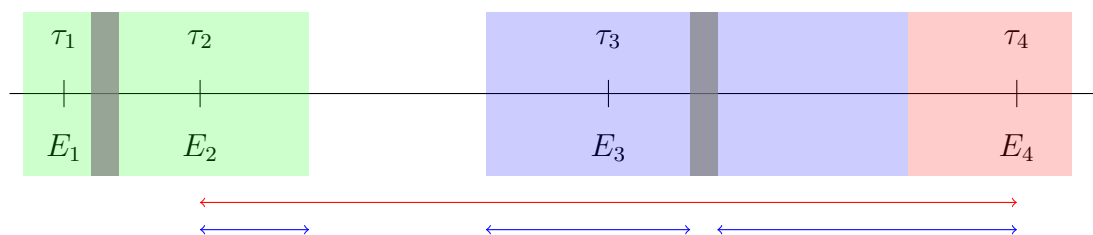


Figure 6.28: Cluster example: For four events E_1 - E_4 at times τ_1 - τ_4 $6 = \frac{4}{2}(4-1)$ clusters can be built: $[1,2],[1,3],[1,4],[2,3],[2,4]$ (red arrow), $[3,4]$. They contain 2, 3, 4, 2, 3 and 2 events. An example run coverage is indicated by the coloured areas (green, blue, red). The grey areas mark possible time periods where the source is above the horizon and thus not visible. The duration for cluster $[2,4]$ is the sum of time periods marked with the blue arrows.

to potential clusters of events. Before going into details on method and software, the definition of a cluster is given.

6.9.1 Cluster definition

Assuming a set M of n events with absolute event times τ_i :

$$M = \{E_1^{\tau_1} \dots E_n^{\tau_n}\}.$$

Any subset of successional events is called a *cluster of events*. Therefore for n events

$$N_c = \sum_{i=1}^{n-1} (n-i) = \frac{n}{2}(n-1) \quad (6.14)$$

clusters in time can be defined. The number of clusters with k events is $n-k+1$. Two different time periods are attributed to each cluster of events:

- The total elapsed time between the first and the last event of the cluster. This time is needed for correlating the detected neutrino signal with astrophysical phenomena.
- The time between the first and the last event, counting only times where the detector was taking data (runs) and where the source was below the horizon (see section on visibility below). In the following this is called the cluster duration. For evaluating the significance of the cluster, the cluster duration is need, since it represents the time period where the telescope was measuring background events.

Figure 6.28 illustrated the definition of clusters including an example of run coverage and source visibility for $n = 4$.

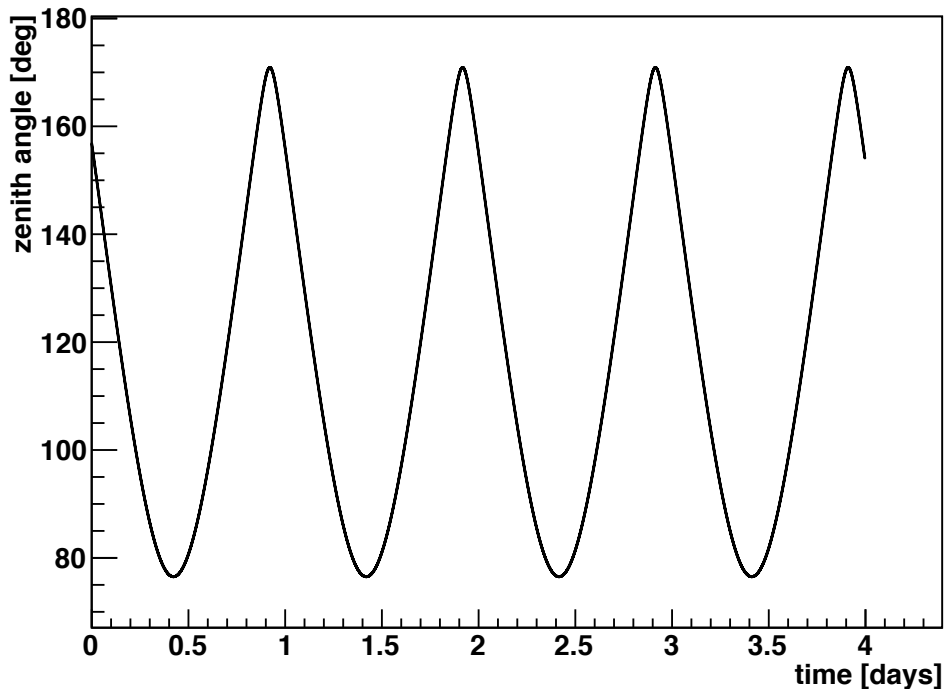


Figure 6.29: Zenith angle of a source at declination $\delta = -34^\circ$ (right ascension $\alpha = 259.4^\circ$) in the ANTARES local frame as function of time starting 2009. As can be seen this source is above the horizon (zenith angle $< 90^\circ$ indicated by the horizontal line) for some part of the day.

6.9.2 Software and procedure

To run the analysis a SeaTray [98] module has been developed that provides the event handling, the cluster generation and the p -value calculation. In the following the main features are explained in detail.

Source visibility

As this analysis searches for neutrinos that have crossed the Earth and therefore for up-going events, sources are called “visible”, if they are below the horizon (source visibility). To determine the source visibility, first the so-called source transit times are calculated. These are the absolute times where the source transverses the horizon in the local detector frame (see figure 6.29). For sources above a declination of -47° this is the case twice per sidereal day, i.e. 732 times for a whole year. Since the sidereal day only has 23.93 hours, the transit times are shifted on a day-by-day basis. The year is sampled with a one minute resolution. See the following lines for an example output of transit times:

```
2009-01-01 06:41:00 UTC
2009-01-01 13:35:00 UTC
```

id	visib.	id	visib.	id	visib.	id	visib.
1	0.7196	2	0.7318	3	0.8240	4	0.8421
5	1.0	6	1.0	7	0.6804	8	0.7186
9	0.7366	10	0.7260	11	0.7319	12	0.7480
13	0.7535	14	0.7707	15	0.7852	16	0.8204
17	0.8488	18	0.8751	19	1.0	20	1.0
21	1.0	22	1.0	23	1.0	24	1.0

Table 6.6: Source visibility fraction for the 24 selected TANAMI sources. The id corresponds to table 6.1.

2009-01-02 06:38:00 UTC
2009-01-02 13:31:00 UTC
2009-01-03 06:34:00 UTC

In a second step these times are correlated with the run structure of the observation period. As runs usually take about 3 hours, there can be 0, 1 or 2 source transit times between run start and run stop. Furthermore the source zenith at run start and run stop are known. Using this combined information, the total source visibility time can be calculated via the following procedure:

- Run with 0 transit times: If at run start and run stop time the source is above the horizon, the run will not be counted. If at both times the source is below the horizon, the run will fully be added to the total visibility time.
- Run with 1 transit time: In this case there are two different possibilities. The source is below the horizon at run start and above at run stop, the visibility period ends at the transit time. In the other case, the visibility period starts at the transit time.
- Run with 2 transit times: In this case the only possible scenario is, that at both run start time and run stop time the source is below the horizon and the time between the two transit times must be cut out. The other theoretical case is not possible due to the typical run length.

After summing up all contributions, the visibilities can be calculated: For 2009 they can be found in table 6.6 (the total lifetime of the sample is 202.985 days):

Generation of scrambled sky maps from data

As already explained in section 6.5 scrambled background-only maps from data are generated from the input events list and a set of randomized times (during one of the runs within the observation period of the analysis). To speed up the procedure 1000 sets of scrambled times have been produced and stored for further use.

Generation of clusters

For a given set of events all clusters according to the definition given in 6.9.1 are generated. For each cluster the following parameters are calculated:

- *ID*: An ID for each cluster. This is also used as internal check for the number of generated clusters.
- *Multiplicity*: Number of events within the cluster. This number is an input for the calculation of the p -value (see below).
- *Duration*: Time difference between the first and the last event of the cluster taking into account times not covered by data-taking runs and source-invisibility periods. This number is an input for the calculation of the p -value.
- *p-value*: see below.
- *List of runs*: List of runs the events were taken from including intermediate runs where no events were taken from.

Cluster p -value calculation

A p -value for observing a given cluster with n events, a duration T and at a background rate r is calculated in the end of the procedure. This is described in detail in the following sections.

6.10 Calculation of p -values

In order to determine if an observed cluster is a statistically significant evidence for neutrino emission from a cosmic source, the p -value is calculated. The p -value is the probability of getting a result (on the chosen test statistic) at least as extreme as the observation in question. For this analysis for each observed cluster of $n \geq 2$ events a p -value is calculated. The important parameter is the cluster length: a result (an observed cluster) is called more extreme than another, if its total cluster length is smaller for clusters with the same number of events and the same background rate. The observation is said to be statistically significant, if the p -value falls below a certain significance level α (for example $\alpha = 5.7 \times 10^{-7} \hat{=} 5\sigma$).

6.10.1 Expected number of clusters

The p -value can be obtained via the expected number of clusters with n events (at times τ_i , $i = 1 \dots n$) within a time window of length $T + dT$ at a given background rate r embedded in an observation period T_{obs} . The rate r is number of observed background events within a given angular search bin around the source. For the events forming the cluster the following time pattern is assumed:

1. The first event is right at the beginning of the time window.

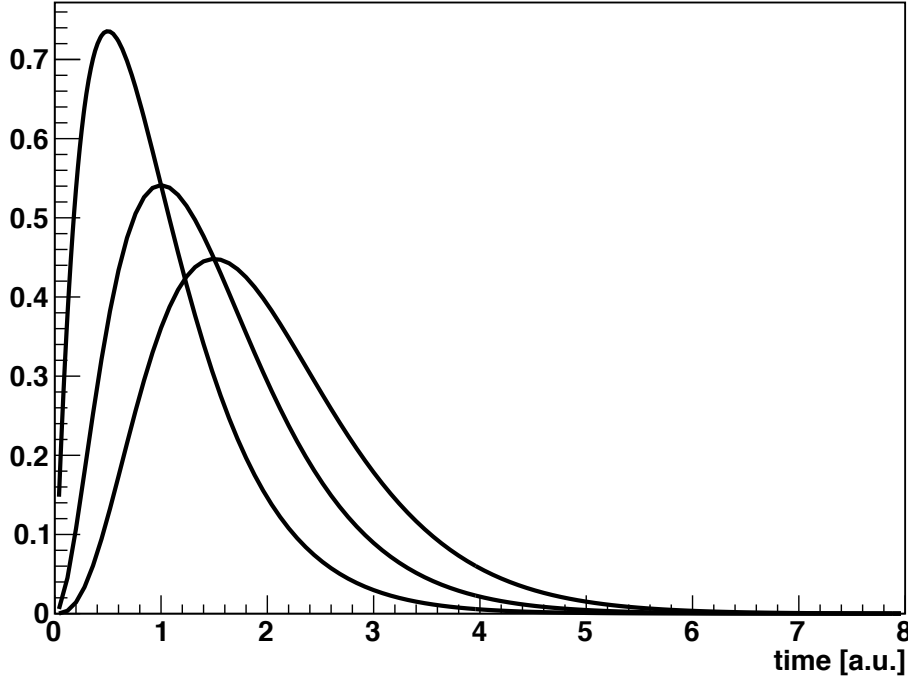


Figure 6.30: Function $\frac{(rt)^{n-2}}{(n-2)!}e^{-rt}r$ (y-axis, see equation 6.15) for three different event numbers $n = 3, 4, 5$ increasing from left to right at constant rate $r = 2$.

2. The last is in the interval $[T, T + dT]$. Since the probability of finding an event at a certain time t_0 is zero, the last event must be located in a finite time interval with length dT .
3. In between there are $n - 2$ events.

In following formulas apply for $n \geq 2$. The probability of observing $n - 2$ events in a time window of length T and one event in a time window of length dT (distributed as stated above) at a rate of r is given by Poisson statistics (see figure 6.30):

$$P(T + dT, n, r) = \text{Poisson}_{\lambda=rT}(n-2) \times rdT = \frac{(rT)^{n-2}}{(n-2)!}e^{-rT}rdT. \quad (6.15)$$

Now it is assumed that this time window of length $T + dT$ is embedded in an observation period with length T_{obs} (see figure 6.31 for illustration). The observation period corresponds to the lifetime of the detector in a given epoch (for example one year). The expected number of clusters of length $T + dT$ to find in this observation period is:

$$\langle N_{\text{cluster}} \rangle = \int_0^{T_{\text{obs}}-T} P(T + dT, n, r)r dt = P(T + dT, n, r)r \cdot (T_{\text{obs}} - T), \quad (6.16)$$

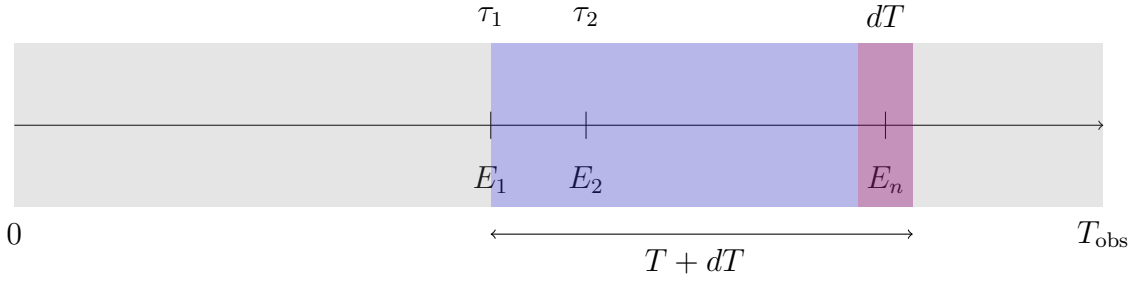


Figure 6.31: Embedded time window of length $T + dT$ for n events $E_1 \dots E_n$ in an observation period with length T_{obs} . The red interval has a length of dT . E_1 is located right at the beginning of the time window, E_n is located in the interval dT and $n - 2$ events are in between.

since the start of the time window can be at any time in the interval $[0, T_{\text{obs}} - T]$. The cumulative distribution $cd(t, N_{\text{cluster}})$ of this expected number of clusters is:

$$cd(r, n, T, T_{\text{obs}}) = \int_0^T \frac{(rt)^{n-2}}{(n-2)!} e^{-rt} r^2 (T_{\text{obs}} - t) dt. \quad (6.17)$$

From equation 6.17 one can calculate the expected number of clusters of multiplicity n at background rate r with a cluster length smaller or as large as T within an observation time T_{obs} . See the following example: For the parameters $n = 5$, $rT_{\text{obs}} = 10$ the cumulative distribution approaches 6 as $T \rightarrow T_{\text{obs}}$ since the maximum number N_{limit} of 5-clusters (clusters with 5 events) in 10 events is six:

$$N_{\text{limit}} = 10 - 5 + 1 = 6. \quad (6.18)$$

Examples for $n = 3, 4, 5$ are shown in figure 6.32.

6.10.2 p -values

From the cumulative distribution $cd(r, n, T, T_{\text{obs}})$ a p -value can be obtained by normalizing this distribution from $[0, N_{\text{limit}}]$ to the interval $[0, 1]$. After normalization the p -value as a function of cluster length is available (see figure 6.33). In other words the p -value of an observed cluster is obtained from these normalized graphs for a given set of n , r and T_{obs} .

As one is interested in very small p -values for a discovery the exponential of equation 6.17 can be expanded like:

$$e^{-rt} \approx 1 - rt + \frac{1}{2}(rt)^2. \quad (6.19)$$

Using this expansion the integral can be performed analytically. This avoids any numerical problems while reading the p -value as function of cluster length:

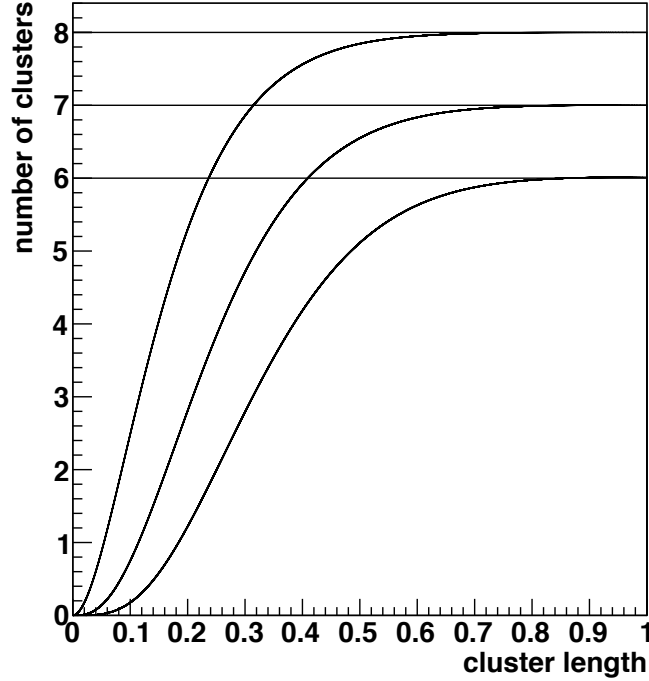


Figure 6.32: Cumulative distribution $cd(r, n, T, T_{\text{obs}})$ of the expected number of clusters (see equation 6.17). Curves for $rT_{\text{obs}} = 10$ and $n = 3, 4, 5$ (top to bottom). As expected the curves approach $N_{\text{limit}} = 10 - n + 1 = 8, 7, 6$ for $T \rightarrow T_{\text{obs}}$. The cluster length is expressed in units of T_{obs} .

$$\begin{aligned}
 cd(r, n, T, T_{\text{obs}}) &= \int_0^T \frac{(rt)^{n-2}}{(n-2)!} e^{-rt} r^2 (T_{\text{obs}} - t) dt & (6.20) \\
 &\approx \frac{1}{(n-2)!} r^n T_{\text{obs}} \frac{1}{n-1} T^{n-1} - \frac{1}{(n-2)!} (r^{n+1} T_{\text{obs}} + r^n) \frac{1}{n} T^n \\
 &+ \frac{1}{(n-2)!} \left(\frac{1}{2} r^{n+2} T_{\text{obs}} + r^{n+1} \right) \frac{1}{n+1} T^{n+1} - \frac{1}{(n-2)!} \frac{1}{2} r^{n+2} \frac{1}{n+2} T^{n+2}.
 \end{aligned}$$

As explained above the p -value is obtained by normalizing the cumulative distribution to the interval $[0, 1]$. An example of the relative difference between the numeric and analytic calculation is plotted in figure 6.35. For larger cluster lengths the approximation by expanding the exponential breaks down.

Figure 6.34 shows the comparison between the prediction and the data for a cone of 5 degrees and $n = 2$ and a background rate of 0.029 per day. The data is obtained from scrambled background maps and scaled by the number of maps processed. As can be seen both match quite well.

6 Cluster search

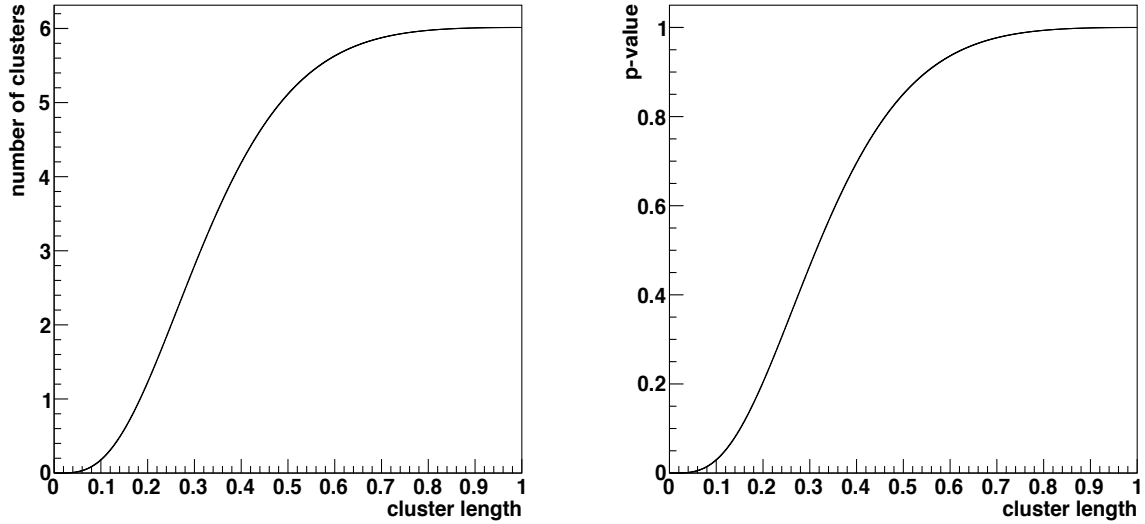


Figure 6.33: *Left:* $cd(r, n, T, T_{\text{obs}})$ for parameters $n = 5$, $rT_{\text{obs}} = 10$. *Right:* p -value as function of cluster length from normalization of left plot.

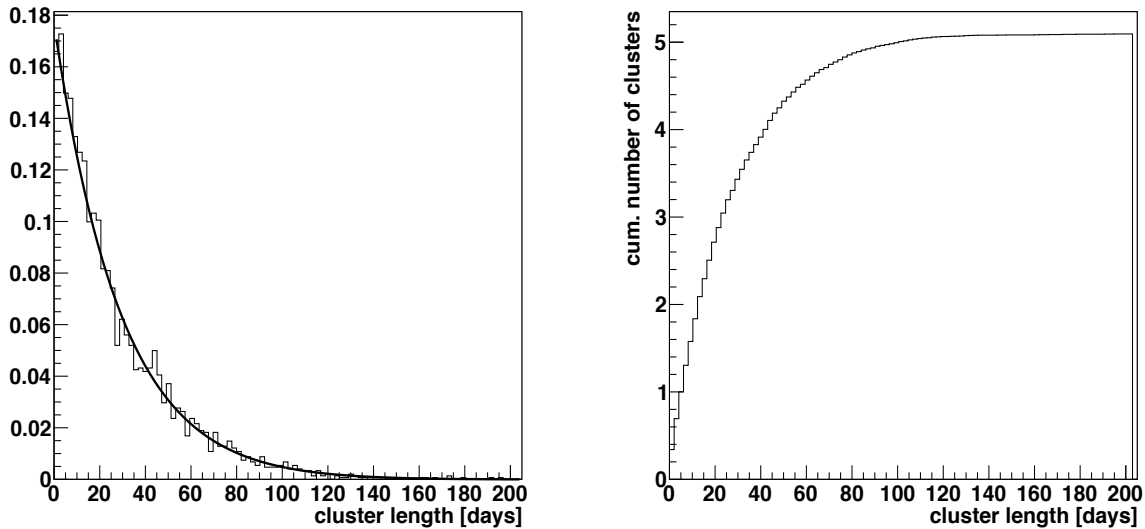


Figure 6.34: *Left:* $\frac{(rt)^{n-2}}{(n-2)!} e^{-rt} r^2 (T_{\text{obs}} - t)$ (y -axis) as function of t (solid curve) for a background rate of 0.029 events per day and an observation time of 204.789 days. The histogram is the data from scrambled background maps. *Right:* Cumulative distribution of data.

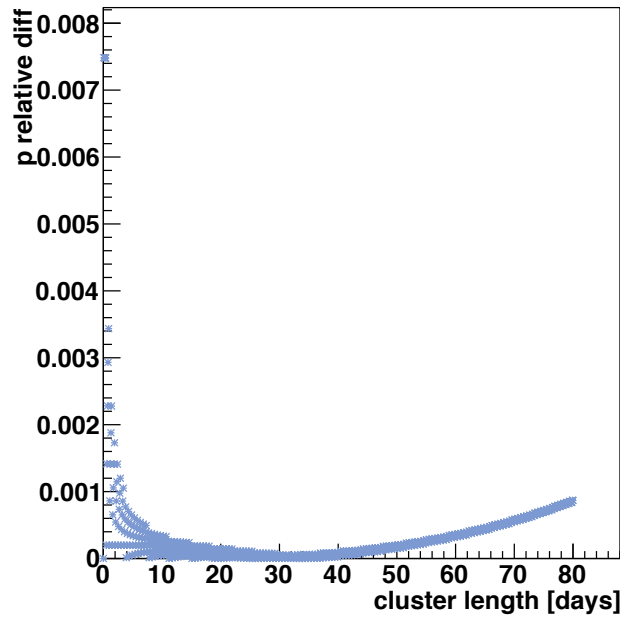


Figure 6.35: Relative difference between analytic and numeric p -values: $2(p_{\text{analytic}} - p_{\text{numeric}})/(p_{\text{analytic}} + p_{\text{numeric}})$.

6.11 Discovery scenario and trail correction

In this section possible discovery scenarios and the corresponding trail correction of the p -values are explained for illustration purposes. If more than one significant detection was found on a single source by observing a primary p -value below a given threshold, one has to define a weighting scheme for these p -values. In principle one can think of many different ways of weighting different searches on a single source (trails) and correcting the p -values accordingly. In the following two of them are explained in more detail.

Equal weighting: Placing the same weight on each search regardless of the cluster size.

- Suppose one detects $N = 4$ events in a given cone around a source.
- Using this $N = 4$ events one can build $N_c = \frac{4}{2} \cdot 3 = 6$ clusters: 1x $n = 4$, 2x $n = 3$, 3x $n = 2$.
- For each cluster a p -value is calculated as described in the previous sections.
- Assuming the following p -values have been calculated for the six trails:
 - $n = 4$: $p_1 = 0.5$,
 - $n = 3$: $p_2 = 0.4$, $p_3 = 0.6$,
 - $n = 2$: $p_4 = 0.2$, $p_5 = 0.7$, $p_6 = 0.9$.

6 Cluster search

- Placing equal weight means that each search on the source is treated in the same manner regardless of the number of events observed in the single trial. Therefore each p -value is multiplied by 6.

Equal weighting for each n : Placing the same weight on each search with the same cluster size.

- Assume the same p -values as in the example above have been calculated.
- Since one generates $N - n + 1$ clusters of size n , there are more of them for low n . In order to account for this, one first puts weights on p -values according to the number of clusters with the corresponding size:

$$p'_k = p_k \cdot w_k \quad k \in \{1, \dots, 6\}.$$

As an example one can choose the weights to be proportional to number of clusters for each n . As there are three different cluster sizes, one gets three weights with the following relative sizes: $w_1 : w_2 : w_3 = 1 : 2 : 3$. Further it is required: $1 \frac{1}{w_1} + 2 \frac{1}{w_2} + 3 \frac{1}{w_3} = 1$. Solving these equations gives: $w_1 = 3$, $w_2 = 6$, $w_3 = 9$. The p -values are then corrected using these weights:

$$\begin{aligned} n = 4: p'_1 &= 0.5 \cdot 3, \\ n = 3: p'_2 &= 0.4 \cdot 6, p'_3 = 0.6 \cdot 6, \\ n = 2: p'_4 &= 0.2 \cdot 9, p'_5 = 0.7 \cdot 9, p'_6 = 0.9 \cdot 9. \end{aligned}$$

- Finally one obtains the minimum of the corrected p -values: $p_{\min} = \min(p'_k)$.

For this analysis the first solution of equal weighting is applied.

6.12 Errors on p -values from rate variations

For this analysis errors on p -values are not considered for the optimization process. However an error on the p -value can be estimated from the remaining fluctuations of the background rate after taking into account the correction for the bioluminescence rate as described below. Using formula 6.20 one can estimate the effect of a remaining uncertainty of the background rate (Δr) on the calculated p -values analytically:

$$\Delta cd = \frac{\partial cd}{\partial r} \cdot \Delta r. \quad (6.22)$$

with

$$\begin{aligned} \frac{\partial cd}{\partial r} &= \frac{1}{(n-2)!} n r^{n-1} T_{\text{obs}} \frac{1}{n-1} T^{n-1} \\ &- \frac{1}{(n-2)!} ((n+1)r^n T_{\text{obs}} + n r^{n-1}) \frac{1}{n} T^n \end{aligned} \quad (6.23)$$

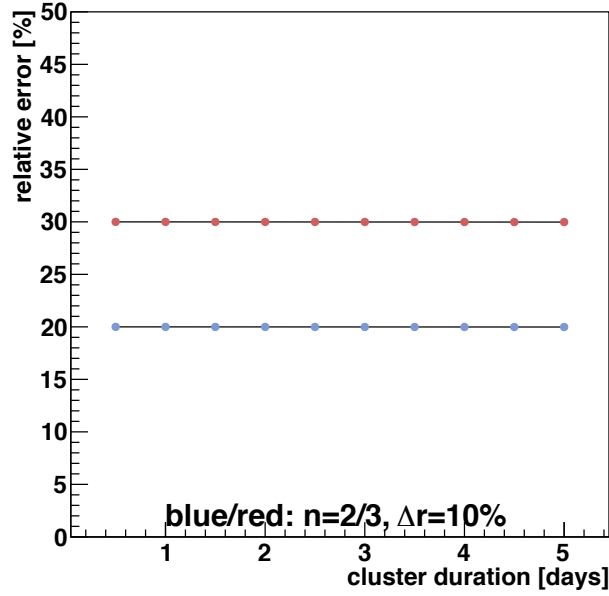


Figure 6.36: Relative error on the p -value as function of cluster duration for a fixed background rate r of 0.0006 per day and different numbers of events n in the cluster.

$$\begin{aligned}
& + \frac{1}{(n-2)!} \left(\frac{1}{2} (n+2) r^{n+1} T_{\text{obs}} + (n+1) r^n \right) \frac{1}{n+1} T^{n+1} \\
& - \frac{1}{(n-2)!} \frac{1}{2} (n+2) r^{n+1} \frac{1}{n+2} T^{n+2}.
\end{aligned}$$

Figure 6.36 shows the expected relative error on the p -value for a typical background rate of 0.0006 events per day (source at low declination) and the two cases $n = 2$ and $n = 3$. A relative error on the p -value $\frac{\partial p}{\partial r}/p \cdot \Delta r$ of roughly 20 (30) percent is observed. For low cluster durations T , where the analytic approximation of equation 6.20 is valid, the error is independent of T (leading terms of cd and $\frac{\partial cd}{\partial r}$ show the same T -dependence).

7 Results from simulation

For the following plots a source flare with a duration of 31 days has been simulated (long-duration flare) for each of the six unblinding candidate sources of this analysis. The events are generated flat in time within this period. This simulation is used to maximize the discovery potential as function of the applied cuts.

7.1 Discovery potential and sensitivity

The discovery potential is meant to be the probability of having a discovery at a pre-defined significance level (here 5σ). The sensitivity is the flux for which the discovery potential crosses the 50% line by definition. The discovery potentials for the 6 sources is presented in figures 7.1 to 7.3. The cone sizes are indicated by different colours. The Λ -cut is indicated by “L52” for example, which means $\Lambda > -5.2$ (see section 6.3.1). The source name (for example S0637 for PKS 0637-752, for full names see table 6.1) and the source declination δ are also shown. The zenith cut of $\theta > 90^\circ$ is indicated by “90”. The error bars are computed according to binomial distribution:

$$\frac{\sqrt{kP(1-P)}}{k} = \sqrt{\frac{P(1-P)}{k}}, \quad (7.1)$$

k is the number of source simulation repetitions (here $k = 100$) and P the detection probability. In order to optimize the search for a maximum sensitivity, the optimal search cone and the Λ -cut are obtained from these plots.

7.1.1 Cone size for $\Lambda > -5.2$

Figures 7.1 to 7.3 show the discovery potential as function of cone size and source declination for $\Lambda > -5.2$. As can be seen from these plots the 2 degree cone yields the best result for all source declinations.

7.1.2 Λ -cut

Figure 7.4 shows the discovery potential for a 2 degree cone and different Λ -cuts for both a source at high (upper plot) and low (lower plot) declination. As can be see there is a small dependence on the lambda-cut for the discovery potential.

7 Results from simulation

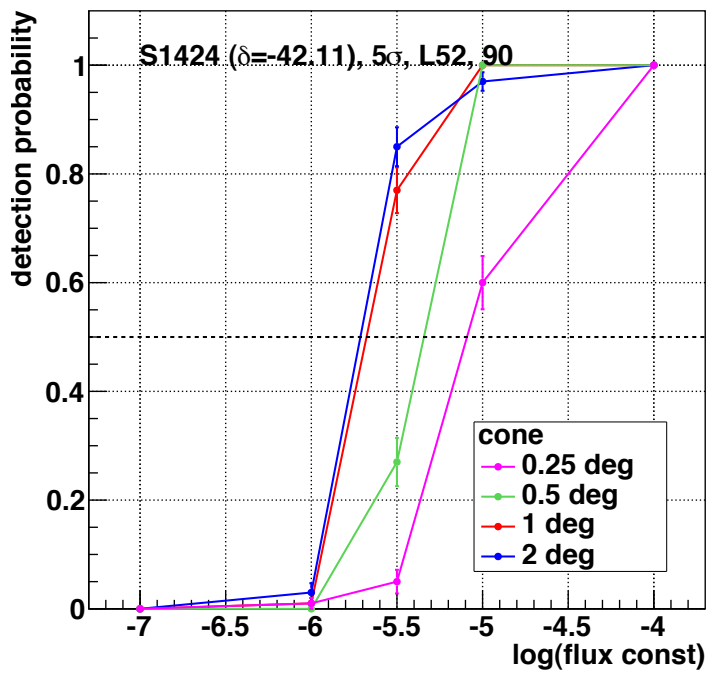
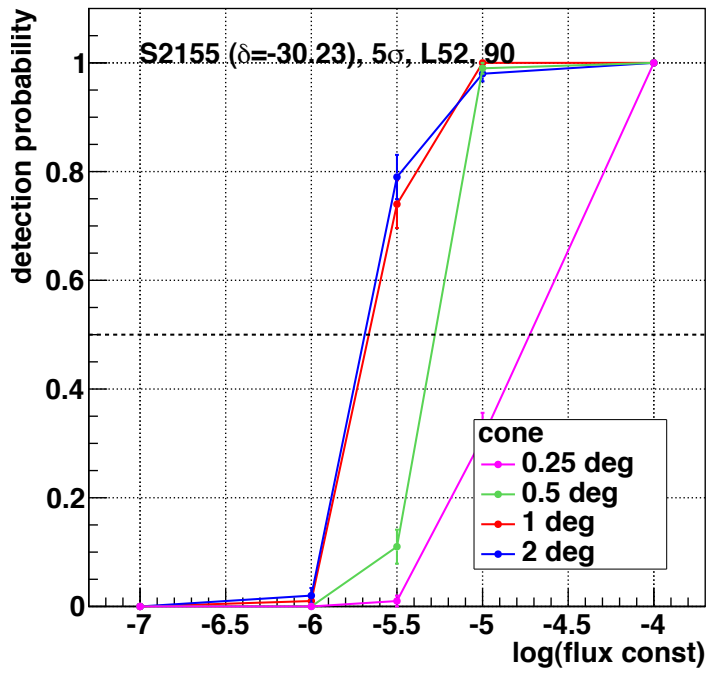


Figure 7.1: *Upper*: Discovery potential for source 2155-304. *Lower*: Discovery potential for source 1424-418.

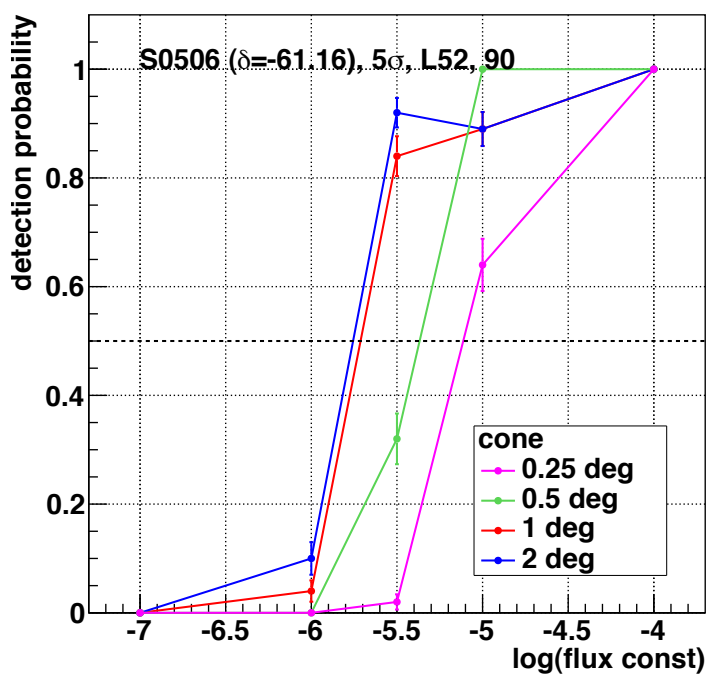
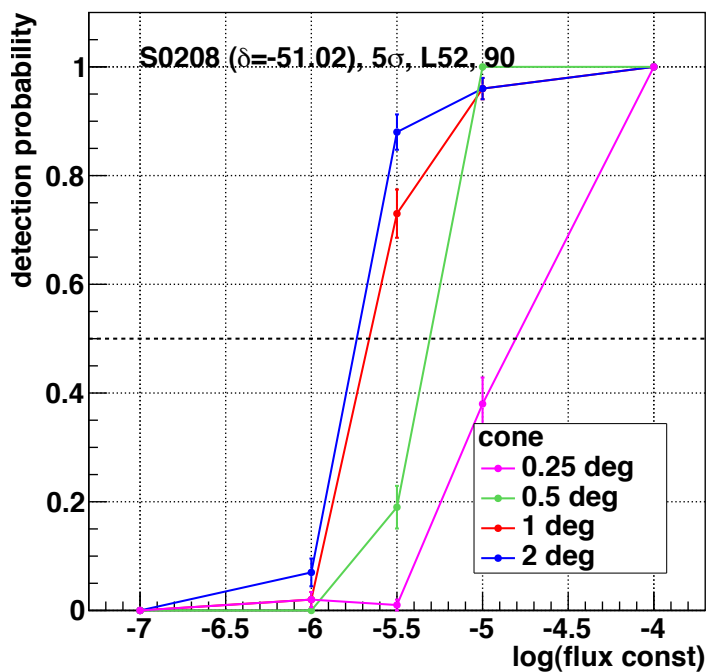


Figure 7.2: *Upper*: Discovery potential for source 0208-512. *Lower*: Discovery potential for source 0506-612.

7 Results from simulation

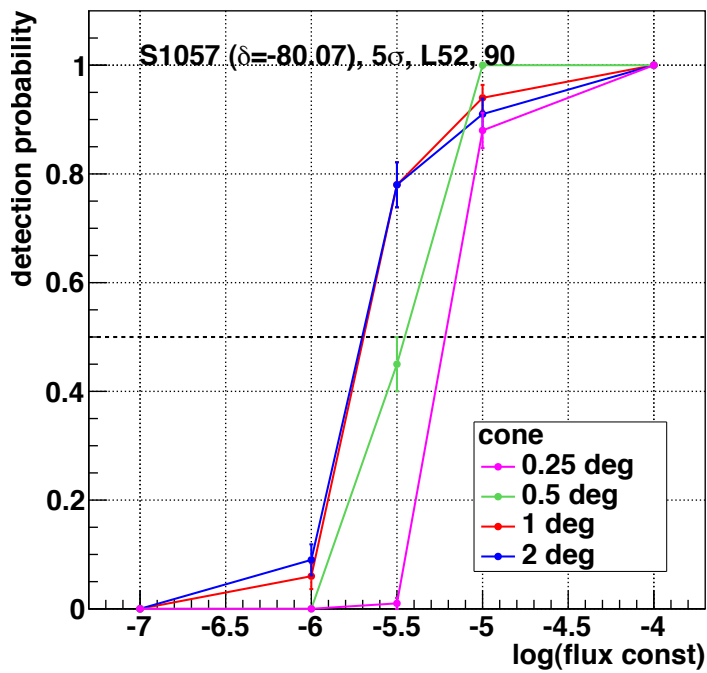
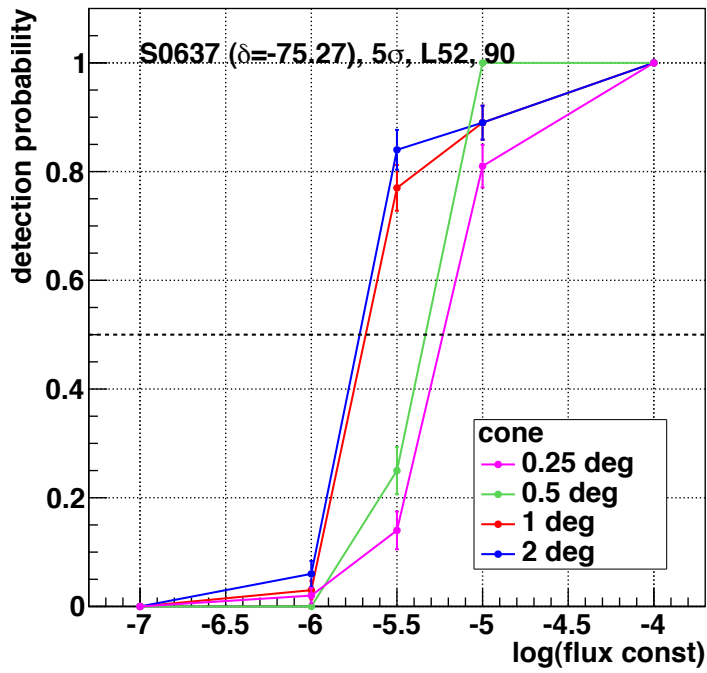


Figure 7.3: *Upper*: Discovery potential for source 0637-752. *Lower*: Discovery potential for source 1057-797.

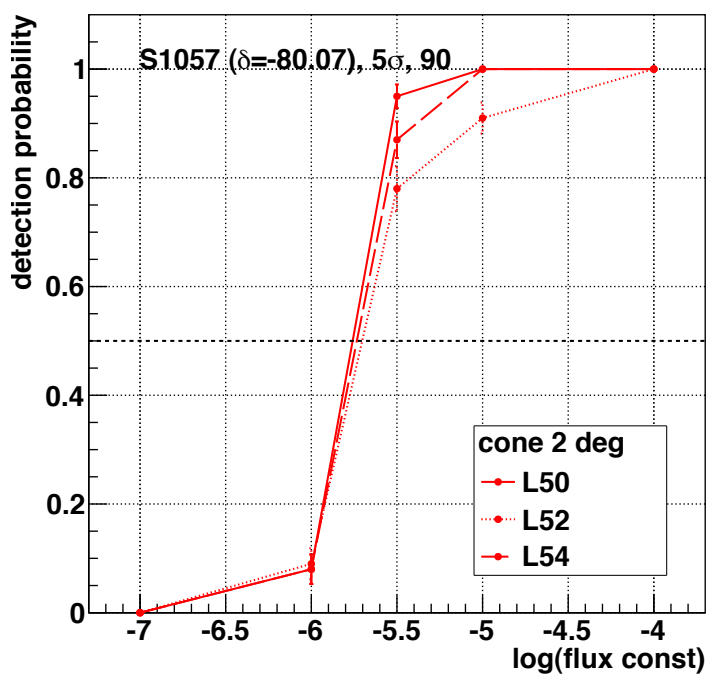
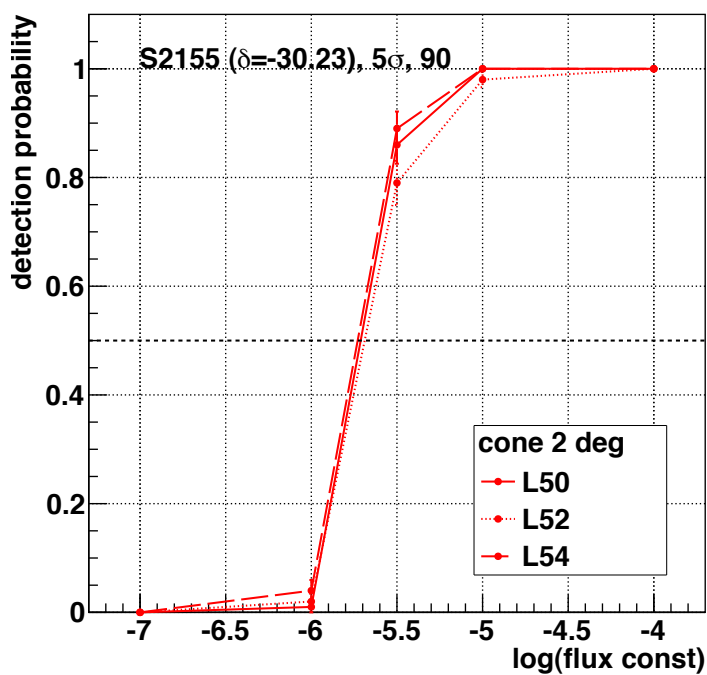


Figure 7.4: *Upper*: Discovery potential for source 2155-304 for different lambda-cuts. *Lower*: Discovery potential for source 1057-797 for different lambda cuts.

Property	Value
Duration	3 days ($\approx 10\%$ of the long-duration flare)
Time	15.01.2009
Source	PKS0208-512

Table 7.1: Properties of the simulated short-term flare. For source information see table 6.1.

7.2 Simulation of a short-duration flare

For completeness and further plausibility tests of the analysis code, also a short-duration flare for one source has been simulated. With $\approx 10\%$ in duration of the long-duration flare it has been chosen significantly shorter than this. Table 7.2 summarizes its properties. The results are discussed below.

Figure 7.5 and 7.6 show the discovery potential for simulated flares of source PKS0208-512 both for the short-duration and long-duration flare respectively. As expected the sensitivity decreases for the for the short-duration flare.

7.3 Time variable background

In this section the effects of a variable background rate are elaborated. As can be seen from figure 7.7 the background rate shows variability during the period of observation. There are several reasons for this behavior: First of all the environmental conditions around the detector vary within the year; this causes variations in the baseline rates and therefore a time-dependent efficiency of triggering on real events. Further the detector availability shows fluctuations: Lines are recovered and later reconnected, single OMs or sectors are temporarily non working (for further details recall section 6.7). Figure 7.8 shows the number of recorded events r_{10} per 10 days from each bin of figure 7.7 as a function of the inverse baseline rate ($1/b$) in this time bin. There is a clear correlation between both quantities (correlation factor 0.82):

$$r_{10} = 3346 \cdot \left(\frac{1 \text{ kHz}}{b} \right) - 9.325. \quad (7.2)$$

To quantify if the remaining fluctuations are consistent with Poissonian statistics, the relative residuals $(\text{data-fit})/\sqrt{\text{data}}$ are shown in figure 7.9. The width of this distribution of the order of 1. The correlation from equation 7.2 is used to adjust the background (later used for the p -value computation) rates as function of time as follows:

The baseline-rates b_i of all runs contributing to an observed cluster with duration d are recorded (also intermediate runs without events are contributing). The adjustment factor is given by

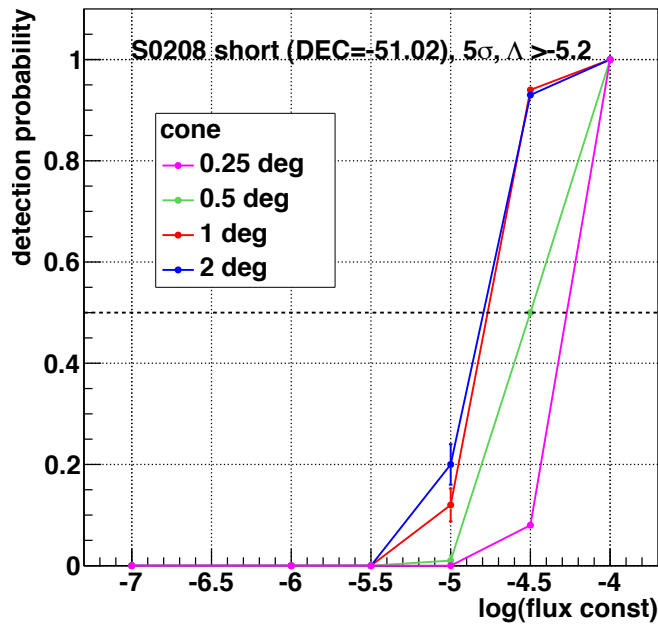


Figure 7.5: Discovery potential for short-duration flare of PKS0208-512.

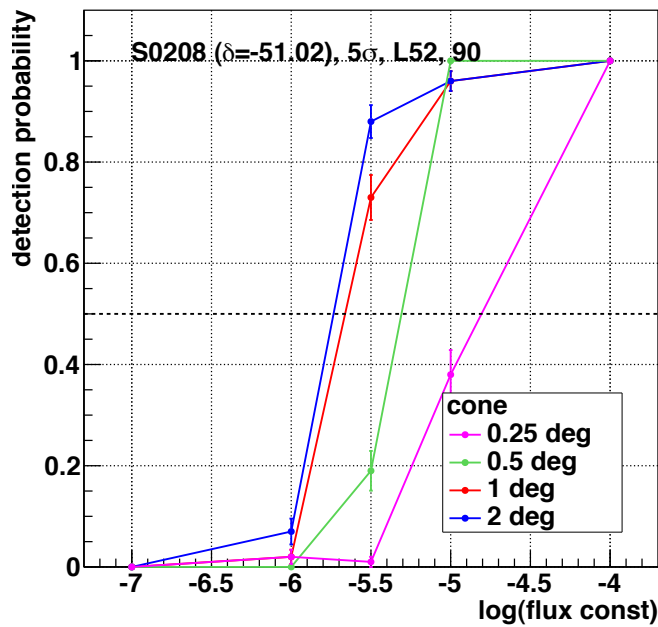


Figure 7.6: Discovery potential for long-duration flare of PKS0208-512.

7 Results from simulation

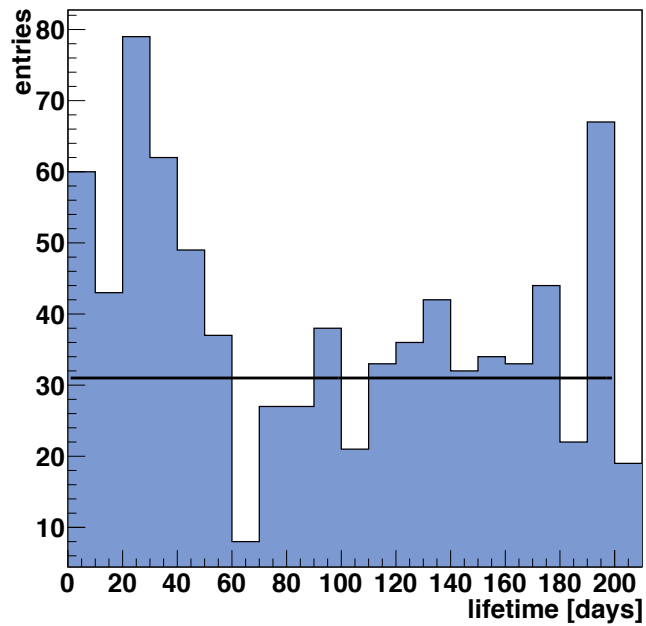


Figure 7.7: Up-going events per 10 days of lifetime for cut parameters $\Lambda > -5.2$ and $\beta < 1^\circ$.

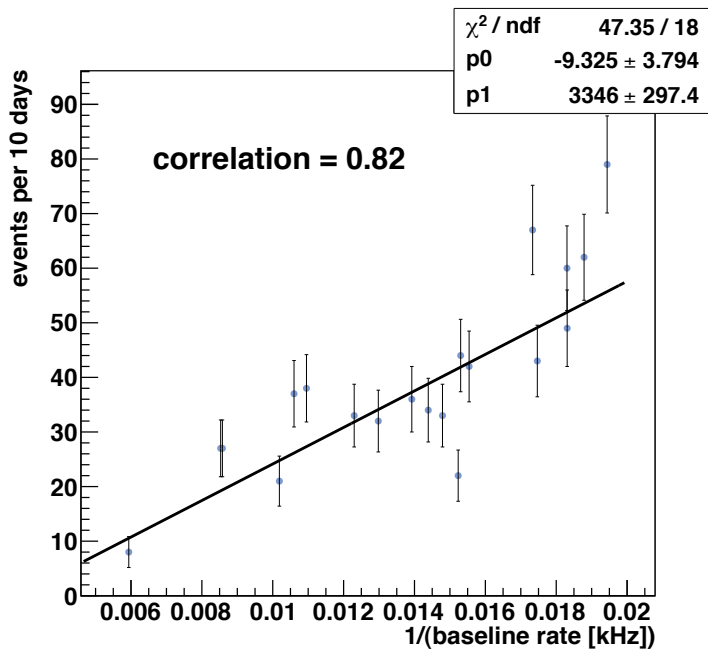


Figure 7.8: Event numbers per 10 days (see figure 7.7) as a function of inverse baseline rate. A clear correlation is found.

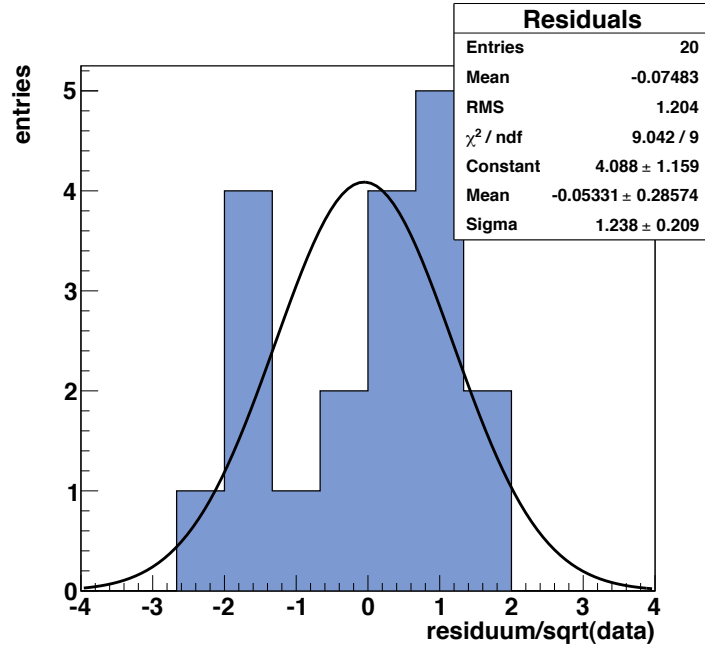


Figure 7.9: Relative residuals from fit in figure 7.8 (normalize by $\sqrt{r_{10}}$). The width of ≈ 1 indicates that the remaining fluctuations are poissonian.

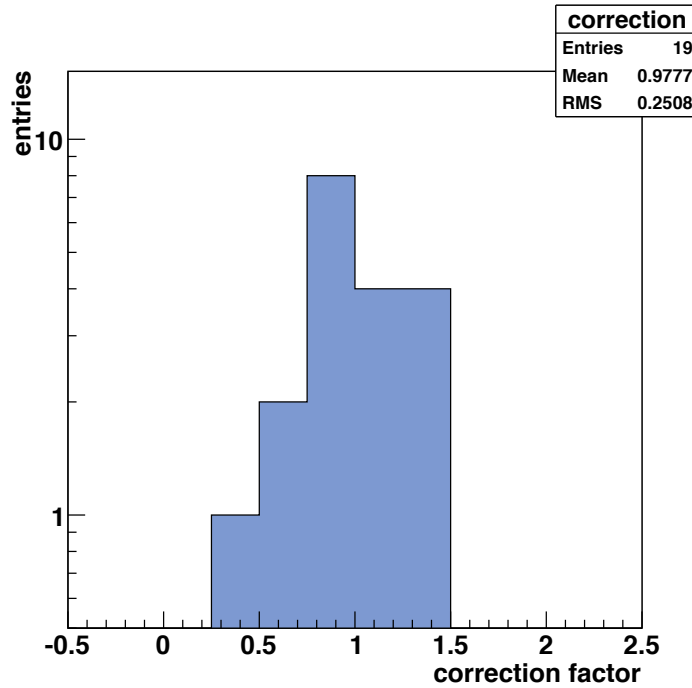


Figure 7.10: Distribution of the correction factor f (see equation 7.3) for the 19 10-day bins of lifetime in 2009. As expected the distribution is centered at 1.

$$f = \frac{\sum_i (T_{\text{run},i} \cdot r_{10}(b_i))}{d} \cdot \frac{1}{R_0}, \quad (7.3)$$

7 Results from simulation

$T_{\text{run},i}$ are the run durations, R_0 is the rate expected from constant background conditions over the whole observation period (for r_{10} see equation 7.2). This factor f gives the correction to be applied to the measured rate for constant background conditions as function of cone size and source declination. A distribution of f for the 19 10-day intervals in 2009 is shown in figure 7.10.

Taking into account rate variations during the observation period means further a adaption of the scrambling method for the generation of blinded background maps from data (see section 6.5 for comparison): the randomly generated event times are now generated according to the measured rate variations.

7.4 Conclusion from simulation

As can be seen from the presented plots on the discovery potential as function of cone size, source declination and Lambda-parameter, it is conclusive to fix the cuts at

$$\Lambda > -5.2, \text{ cone} = 2^\circ, (\beta < 1^\circ, \theta > 90^\circ).$$

7.5 Limit setting procedure

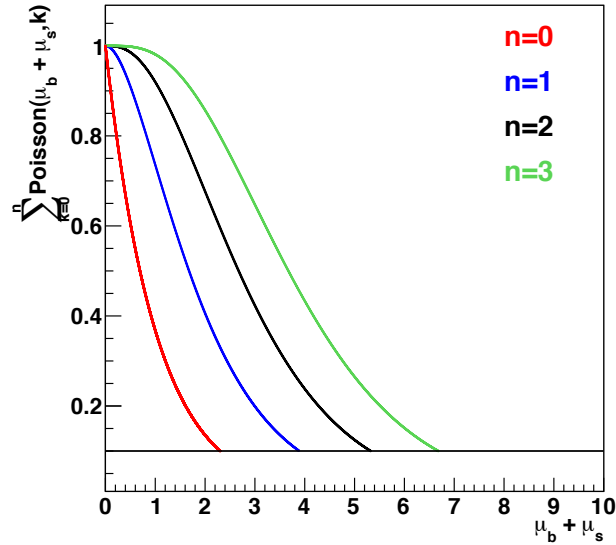


Figure 7.11: Illustration of formula 7.4 for $n = 0$ (red), $n = 1$ (blue), $n = 2$ (black) and $n = 3$ (green). The intersections with the black horizontal line (10%) are at 2.31, 3.89, 5.33 and 6.69. For details see text.

Once no or a single event or a non-significant cluster (2 or more events) have been observed, there is no detection made in this context and one can set limits on the source flux. For the limit setting the following cases of observed events/clusters are considered:

1. A cluster with ≥ 2 events in a time range T with a *significant* p -value is observed: This is called a detection.
2. A cluster with $n \geq 2$ events in a time range T with a *non-significant* p -value is observed: In this case the flux limit is the source flux (normalization constant \mathcal{K}), that produces $k > n$ observed events in the time window T at 90% confidence level. The value of \mathcal{K} is obtained by solving the following equation:

$$\sum_{k=0}^n \text{Poisson}(\mu_b + \mu_s(\mathcal{K}), k) = 0.1, \quad (7.4)$$

where μ_b and μ_s are the expectation values for background and signal events in T (see figure 7.11 for illustration).

3. *No cluster (this means no or one event, $n = 0 \vee n = 1$)* is observed: In this case the (flux-)limit is the source flux, that produces $k > n$ observed events in 31 days at 90% confidence level, again obtained by equation 7.4.

As the observation period for this analysis is one full year (effective ANTARES lifetime is smaller), for case number 3 one might think of using this period as the reference for the corresponding limit. As this time referencing has been done by various other analysis, the method described above is used here.

7 *Results from simulation*

8 Results after unblinding

8.1 Unblinding request

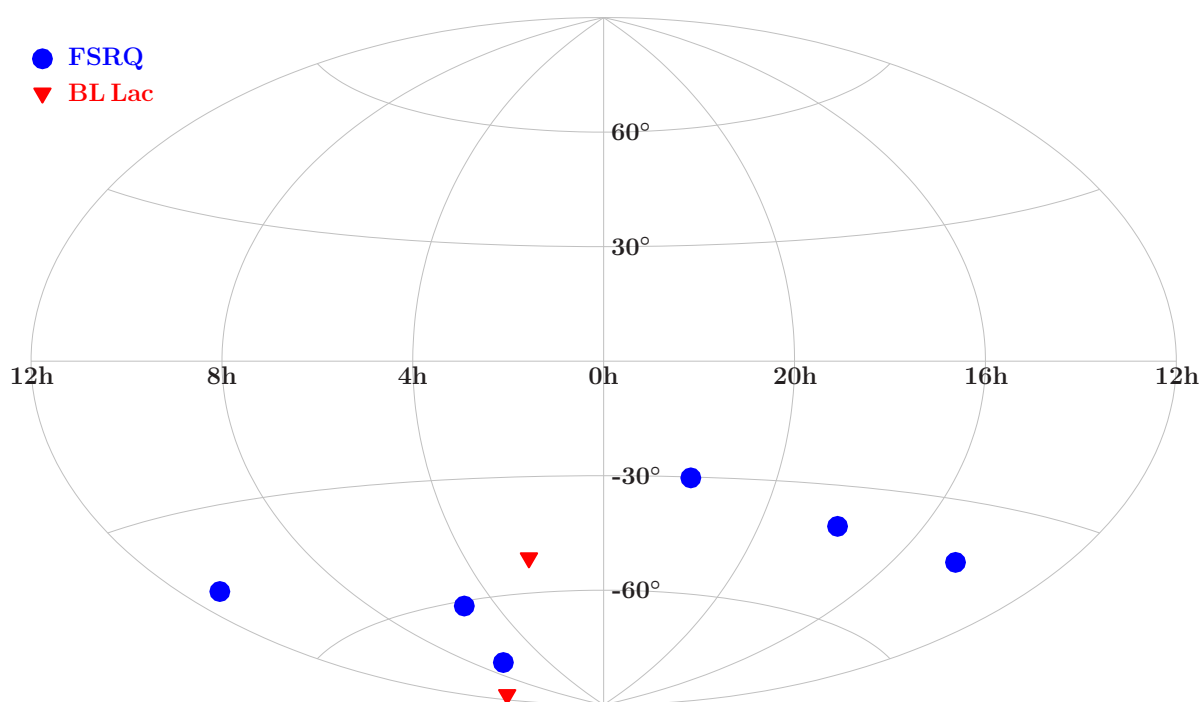


Figure 8.1: Skymap (Aitoff projection) of the eight sources chosen for the unblinding request.

For unblinding a subsample of eight sources has been chosen. The sources have been selected to obtain a reasonable sky coverage in both right ascension and declination (see figure 8.1 and figure 6.7 for flux and variability informations). For full 2009 data have been requested and endorsed for unblinding. Choosing 8 sources out of the 24 primary candidates and the full 2009 data, this represents a fraction of roughly 8% of the possible range (data/sources) at that time. The sources are: 0208-512, 1057-797, 2155-304, 1954-388, 1424-418, 1104-445, 0506-612, 0637-752 (see table 6.1 for details and coordinates).

8.2 Results after unblinding

From the eight sources no significant cluster of events was observed in the data. The numbers of events found per source are listed in table 8.1. Further the source flux limit as described in section 7.5 is given in the last column of table 8.1 for a flare of one month. It is obtained from figures 8.3 to 8.6 (see next pages). The timestamps of the three events observed are:

- 0208-512: 2009-05-23 07:51:18, 2009-12-14 18:36:09,
- 1954-388: 2009-11-03 21:16:45.

Even though the two events from PKS0208-512 do not form a significant cluster, they can be individually superimposed with the gammy-ray lightcurve of the source. As can be seen in figure 8.2 there is no overlap in time with a significant flaring activity of PKS0208-512.

Source	Events	$\mu_b + \mu_s$ for limit	Limit (90% CL)
0208-512	2	5.33	$10^{-5.85} \text{ GeV s}^{-1} \text{ cm}^{-2}$
1057-797	0	2.31	$10^{-6.26} \text{ GeV s}^{-1} \text{ cm}^{-2}$
2155-304	0	2.31	$10^{-6.20} \text{ GeV s}^{-1} \text{ cm}^{-2}$
1954-388	1	3.89	$10^{-5.97} \text{ GeV s}^{-1} \text{ cm}^{-2}$
1424-418	0	2.31	$10^{-6.23} \text{ GeV s}^{-1} \text{ cm}^{-2}$
1104-445	0	2.31	$10^{-6.25} \text{ GeV s}^{-1} \text{ cm}^{-2}$
0506-612	0	2.31	$10^{-6.23} \text{ GeV s}^{-1} \text{ cm}^{-2}$
0637-752	0	2.31	$10^{-6.25} \text{ GeV s}^{-1} \text{ cm}^{-2}$

Table 8.1: Events found for the eight unblinding candidates. In two cases a non-significant cluster was found (see case 2 in section 7.5). For $\mu_b + \mu_s$ -thresholds see figure 7.11. The last column shows the limit as explained in section 7.5 case 3. For source 0208-512 the corresponding limit for the real duration between the two observed events (120.26 days of lifetime) is: $10^{-5.87} \text{ GeV s}^{-1} \text{ cm}^{-2}$.

As can be seen from [129] for sources at declinations below $\delta < -30^\circ$ similar flux limits were observed (note the factor or ≈ 40 between the lifetimes of the data samples).

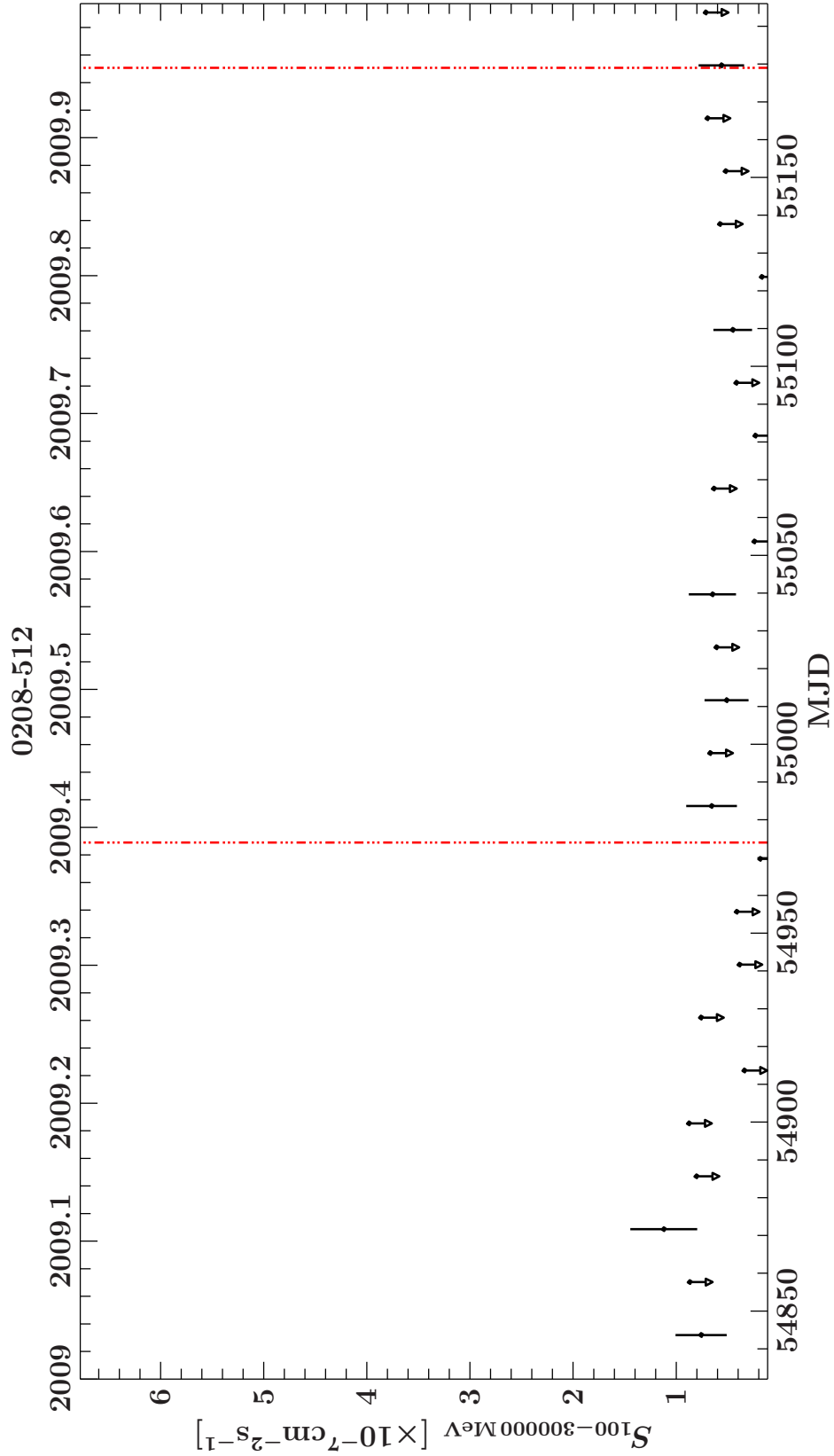


Figure 8.2: *Fermi*-Lightcurve of 0208-512 in 2009. The dashed red lines indicate the timestamps (exact values see text) of the two events found for this source in May and December 2009.

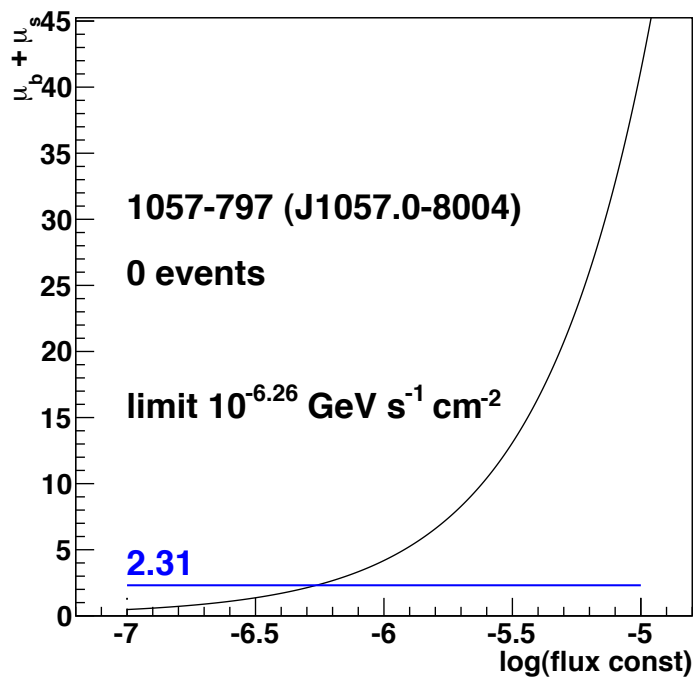
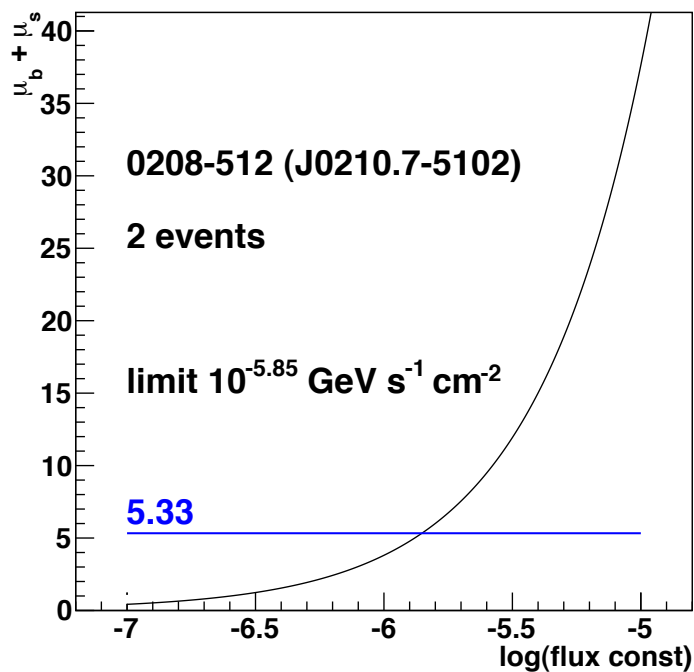


Figure 8.3: *Upper*: Limit determination for 0208-512. *Lower*: Limit determination for source 1057-797.

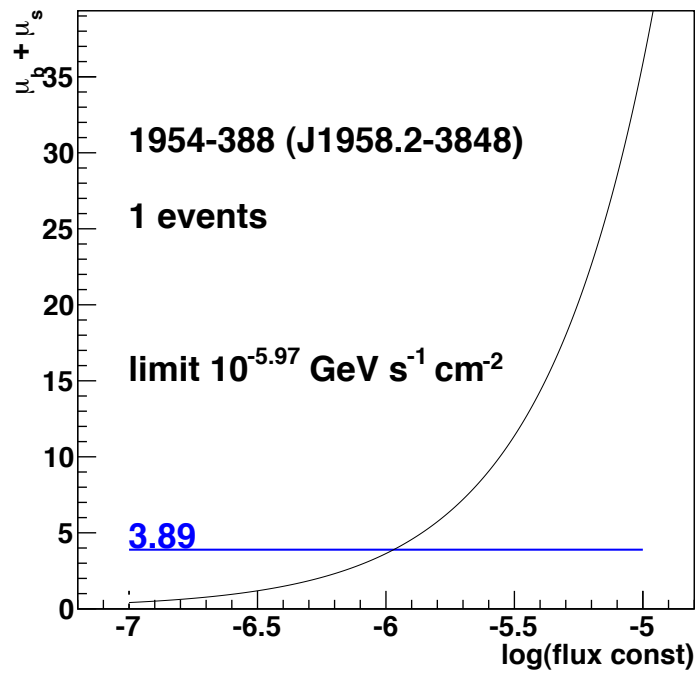
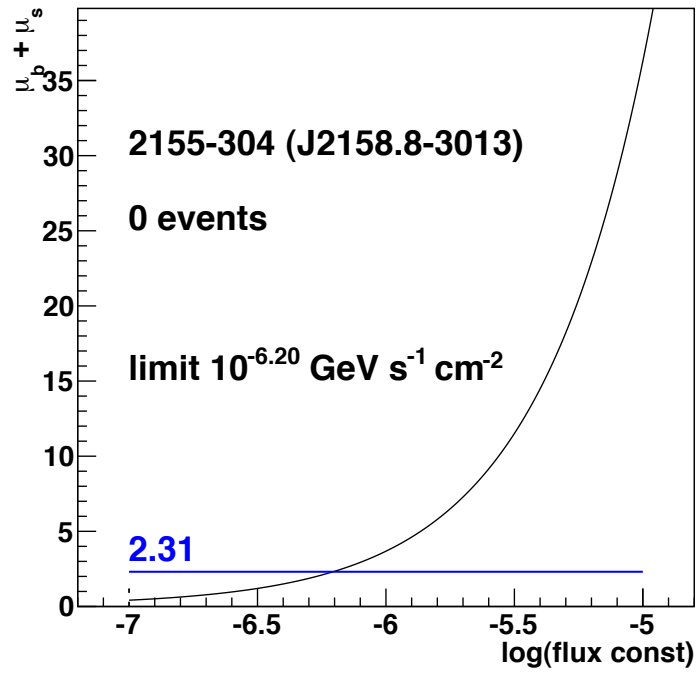


Figure 8.4: *Upper*: Limit determination for 2155-304. *Lower*: Limit determination for source 1954-388.

8 Results after unblinding

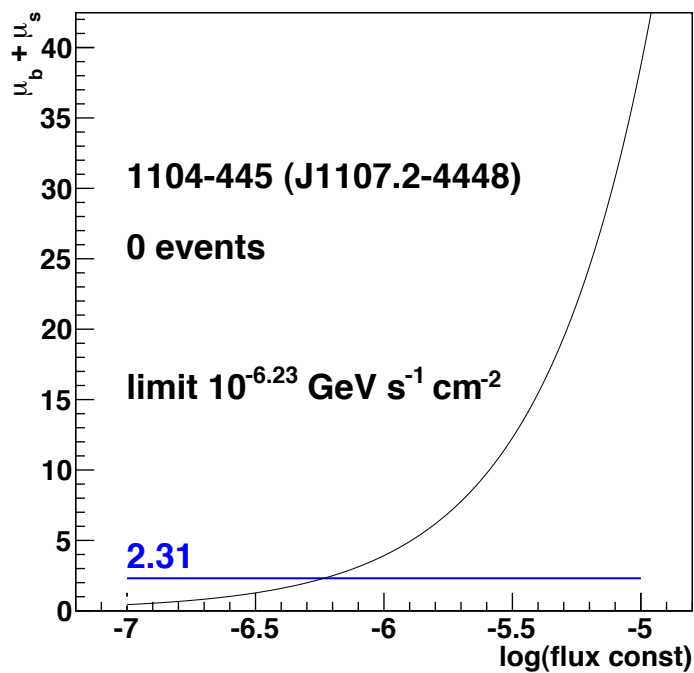
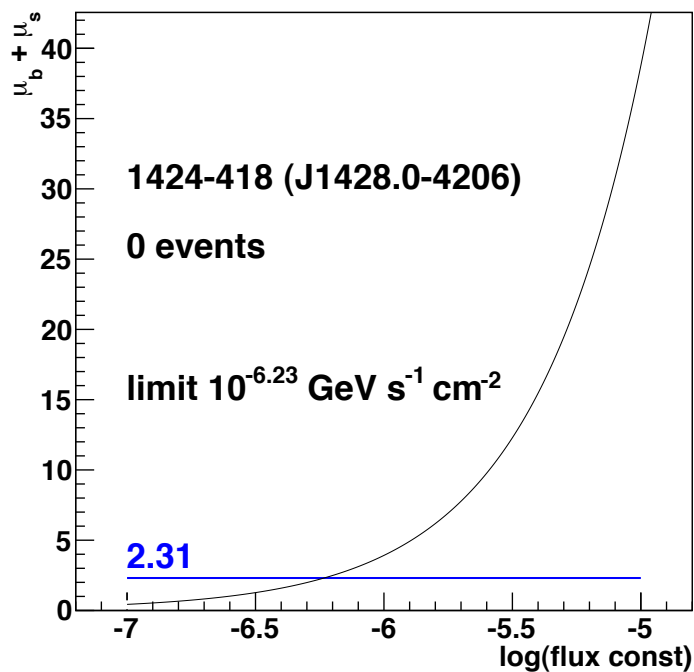


Figure 8.5: *Upper*: Limit determination for 1424-418. *Lower*: Limit determination for source 1104-445.

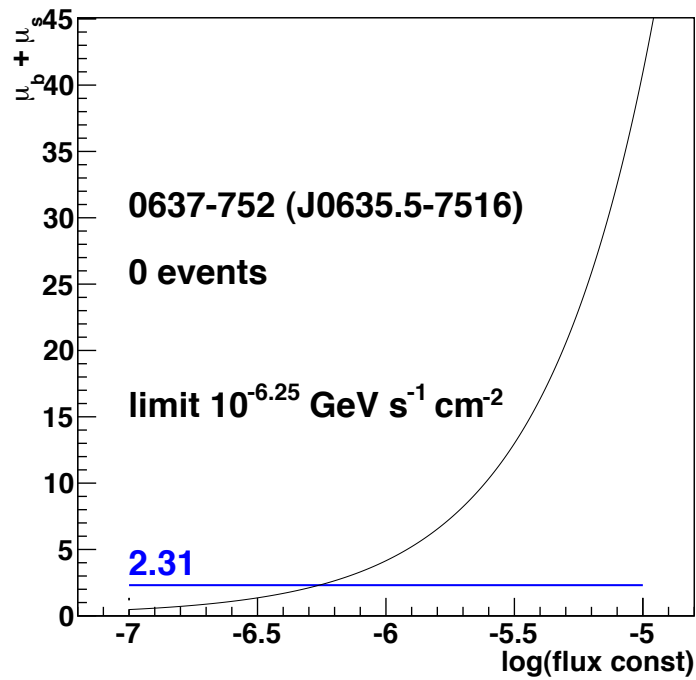
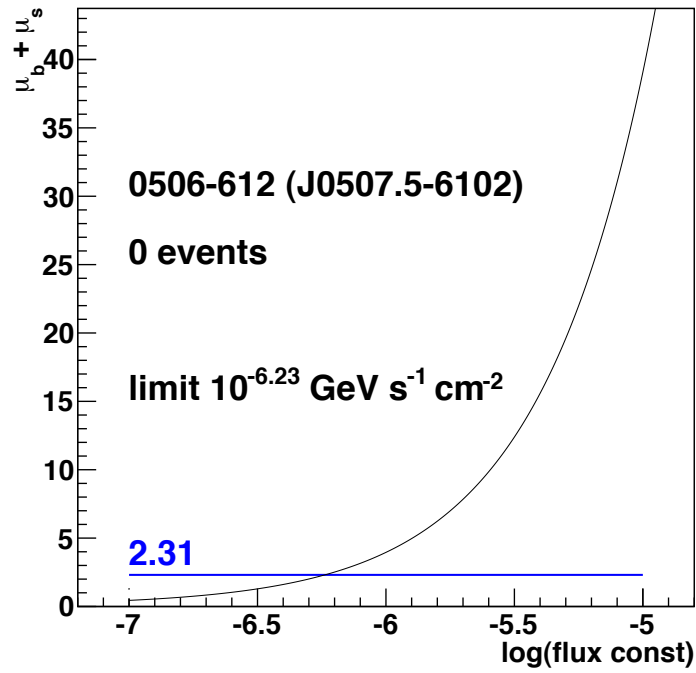


Figure 8.6: *Upper*: Limit determination for 0506-612. *Lower*: Limit determination for source 0637-752.

8 *Results after unblinding*

9 Conclusion and outlook

After several years of planning, construction and commissioning including both positive and negative experimental experiences, the operation of the ANTARES neutrino telescope has brought a deeper insight in deep-sea underwater neutrino telescoping. As has been shown in the first part of this work, despite environmental obstacles like high bioluminescence and an underwater sea currents, a technology - in this case especially for the positioning - has been proven to provide the necessary data for a precise offline positioning. The combination of acoustic and conventional positioning techniques can therefore be used in future underwater detector projects.

Once all calibration data is available and the necessary interfaces to the software framework for event reconstruction have been tested successfully, one can look for neutrino emission for various sources in the sky. For this work I have chosen a sample of AGN at the southern sky, where neutrino data can complement a multi-messenger spectrum of particle information: The TANAMI sources. As AGN show variabilities on a broad range of time-scales the goal of this analysis was to be not restrictive on certain time windows or to use external triggers.

In the 2009 data no significant cluster of events was observed from the sub-sample of eight TANAMI sources. The corresponding limits on the source flux have been calculated. However it is worth to look at all TANAMI sources in a larger amount of ANTARES data. Eventually in a several years long observations period clustered neutrino events can be found from one of the sources, ideally in coincidence with a prominent jet phenomenon (derived from observations of high-energy gamma rays or a time-series of VLBI-observations).

These kind of analysis can be further improved by a more precise modeling of the detector sensitivity as function of time. As the effective detector configuration and the environmental conditions (bioluminescence and sea currents) change on an event by event basis, in a next step various parameters need to be studied and evaluated for a realistic sensitivity estimation and event qualification.

In contrary to this analysis one might think of specifically taking into account gamma-ray flaring information and only pick times where sources were in an active state. However I propose for ANTARES and future projects to apply both kinds of analyses in parallel.

9 *Conclusion and outlook*

10 Appendix

10.1 List of run numbers

This is the complete list of run numbers selected for the analysis (in total 1597). Runs marked with “s” are sparking runs (see section 10.2). Runs marked with “e” do have a file corruption. Both are excluded from the data-selection.

38233 38241 38242 38244 38249 38251 38252 38253 38255 38257 38258 38260 38261
38263 38264 38265 38285 38287 38289 38290 38292 38293 38294 38296 38298 38299
38329 38331 38332 38347^s 38348^s 38349^s 38351^s 38352^s 38353^s 38355^s 38357^s 38363
38365 38391 38397 38398 38400 38402 38403 38404 38406 38407 38410 38421 38423
38424 38426 38427 38429 38431 38432 38435 38438 38440 38442 38443 38445 38447
38448 38450 38451 38461 38463 38465 38466 38467 38470 38472 38474 38475 38477
38478 38480 38481 38482^s 38485 38486 38488 38489 38491 38492 38493 38495 38496
38500 38502 38503 38504 38506 38511 38512 38515 38517 38518 38519 38520 38521
38523 38524 38526 38527 38529 38533 38534 38536 38537 38539 38540 38542 38543
38546 38548 38549 38551 38552 38554 38555 38557 38558 38560 38562 38569 38571
38572 38574 38575 38577 38578 38581 38582 38583 38585 38586 38588 38589 38590
38592 38593 38596 38597 38599 38600 38601 38603 38604 38606 38607 38610 38611
38612 38614 38615 38617 38618 38620 38621 38623 38625 38626 38628 38629 38631
38632 38634 38635 38636 38639 38640 38641 38643 38645 38646 38647 38649 38650
38652 38654 38656 38658 38659 38661 38663 38664 38665 38667 38668 38671 38672
38674 38685 38687 38688 38690 38691 38692 38695 38696 38697 38699 38700 38702
38703 38711 38712 38716 38717 38719 38720 38722 38723 38724^e 38726 38727 38738
38739 38741 38742 38744 38745 38747 38748 38750 38752 38753 38755 38756 38757
38759 38760 38762 38765 38766 38770 38771 38773 38774 38780 38783 38784 38787
38788 38790 38791 38793 38795 38796 38799 38800 38801 38803 38805 38806 38807
38809 38810 38813 38814 38823 38824 38826 38827 38829 38830 38833 38834 38835
38837 38838 38840 38841 38843 38844 38847 38849 38850 38852 38853 38855 38856
38869 38899 38900 38902 38903 38905 38906 38908 38909 38913 38917 38918 38925
38926 38928 38929 38931 38932 38934 38936 38938 38940 38941 38943 38944 38946
38947 38949 38951 38953 38954 38955 38957 38958 38960 38961 38962 38965 38966
38968 38969 38971 38972 38974 38975 38977 38978 38980 38982 38983 38985 38986
38988 38989 38990 38992 38994 38996 38997 38999 39000 39001 39003 39004 39006
39008 39015 39021 39022 39025 39028 39030 39031 39033 39034 39036 39037 39038
39040 39042 39044 39045 39047 39048 39049 39051 39052 39054 39056 39057 39059
39060 39062 39063 39065 39066 39067 39069 39071 39072 39074 39076 39078 39079
39080 39082 39083 39085 39086 39087 39090 39091 39095 39099 39101 39102 39104

10 Appendix

39105 39106 39108 39109 39111 39112 39114 39116 39117 39119 39120 39122 39124
39125 39127 39128 39131 39133 39134 39144 39147 39150 39151 39153 39154 39155
39157 39158 39159 39161 39168 39169 39180 39181 39182 39184 39196 39197 39199
39204 39205 39207 39209 39211 39212 39214 39215 39217 39218 39220 39221 39223
39225 39227 39228 39229 39231 39232 39234 39235 39237 39238 39240 39242 39244
39246 39247 39249 39250 39254 39255 39257 39259 39260 39262 39263 39265 39266
39273 39307 39313 39319 39321 39324 39327 39331 39341 39342 39345 39349 39351
39357 39360 39362 39364 39365 39369 39372 39373 39377 39379 39381 39382 39384
39387 39389 39391 39393 39395 39398 39400 39410 39420 39425 39427 39430 39432
39438 39442 39453 39456 39458 39460 39462 39464 39466 39469 39564 39565 39567
39569 39570 39573 39575 39580 39581 39583 39586 39589 39590 39609 39617 39620
39623 39625 39627 39629 39631 39633 39636 39638 39640 39642 39644 39647 39649
39652 39662 39669 39671 39673 39675 39677 39680 39682 39683 39685 39689 39700
39702 39705 39707 39711 39717 39718 39723 39725 39726 39727 39728 39729 39757
39760 39762 39763 39765 39772 39774 39775 40098 40111 40119 40150 40152 40154
40155 40157 40160 40161 40167 40169 40171 40177 40179 40189 40191 40195 40197
40199 40205 40206 40213 40216 40218 40220 40221 40223 40225 40227 40231 40233
40238 40453 40473 40475 40478 40480 40483 40494 40507 40509 40516 40530 40545
40553 40555 40591 40594 40603 40606 40608 40616 40618 40623 40647 40649 40653
40655 40657 40659 40660 40663 40664 40666 40668 40669 40672 40675 40676 40677
40678 40681 40682 40684 40686 40688 40690 40691 40695 40697 40698 40705 40706
40707 40709 40710 40712 40713 40714 40716 40717 40718 40719 40721 40722 40741
40751 40753 40756 40758 40762 40763 40765 40766 40768 40770 40772 40775 40777
40780 40783 40784 40786 40788 40790 40793 40795 40799 40803 40804 40805 40808
40809 40841 40848 40859 40867 40870 40872 40879 40880 40884 40908 40910 40912
40913 40916 40917 40920 40922 40924 40926 40930 40944 40957 40959 40962 40964
40966 40967 40969 41005 41009 41014 41089 41092 41094 41096 41161 41164 41166
41168 41171 41173 41175 41177 41192 41194 41196 41198 41201 41203 41204 41206
41208 41209 41212 41214 41215 41217 41222 41224 41226 41228 41231 41233 41234
41237 41247 41249 41251 41252 41254 41257 41259 41261 41262 41265 41268 41270
41279 41281 41283 41285 41287 41289 41292 41295 41301 41303 41305 41308 41310
41313 41314 41316 41318 41320 41321 41350 41352 41353 41355 41365 41367 41369
41370 41373 41374 41376 41377 41381 41384 41385 41388 41390 41391 41393 41395
41397 41399 41400 41402 41403 41404 41406 41408 41410 41411 41416 41417 41418
41421 41423 41424 41426 41428 41429 41430 41431 41433 41434 41435 41437 41439
41440 41441 41442 41444 41445 41446 41449 41450 41452 41453 41455 41469 41481
41482 41483 41484 41486 41487 41488 41489 41491 41492 41498 41524 41528 41534
41536 41538 41540 41543 41546 41548 41550 41552 41555 41557 41560 41563 41567
41569 41578 41580 41582 41584 41586 41591 41597 41605 41608 41610 41612 41614
41626 41628 41661 41662 41665 41666 41668^s 41673 41675 41677 41679 41684 41687
41690 41691 41692 41694 41696 41697 41699 41702 41703 41706 41711 41712 41714
41715 41717 41719 41722 41724 41727 41729 41731 41733 41737 41740 41742 41744
41769 41780 41781 41784 41787 41789 41803 41808 41810 41812 41815 41822 41826
41828 41830 41835 41836 41839 41842 41844 41845 41847 41850 41852 41854 41870

41886 41899 41913 41937 41939 41940 41944 41947 41950 41952 41971 41973 41975
 41977 41980 41982 41984 41988 41991 41993 41995 41996 41998 42001 42003 42005
 42020 42032 42035 42038 42042 42045 42047 42050 42053 42056 42059 42062 42064
 42066 42069 42072 42074 42076 42086 42088 42090 42091 42096 42102 42109 42111
 42114 42116 42117 42119 42121 42129 42132 42135 42137 42161 42174 42178 42181
 42185 42187 42190 42198 42208 42264 42320 42323 42326 42359 42362 42365 42369
 42373 42376 42379 42381 42407 42412 42415 42417 42420 42425 42477 42482 42494
 42497 42500 42502 42504 42507^s 42511^s 42513 42515 42518 42521 42523 42526 42528
 42530 42533 42536 42541 42543 42545 42547 42550 42554 42577 42580 42585 42588
 42592 42594 42597 42602 42606 42609 42612 42616 42623 42625 42628 42631 42634
 42638 42640 42643 42646 42649 42652 42655 42658 42661 42668 42671 42676 42679
 42682 42686 42689 42692 42695 42698 42746 42750 42753 42756 42758 42765 42771
 42777 42781 42785 42792 42796 42799 42804 42810 42811 42813 42815 42819 42821
 42825 42829 42831 42835 42838 42842 42851 42856 42860 42863 42866 42889 42893
 42897 42900 42906 42909 42912 42915 42919 42922 42926 42936 42941 42944 42950
 42954 42959 42962 42964 42967 42971 42973 42976 42983 42986 42990 42994 42997
 43003 43007 43010 43015 43019 43022 43026 43031 43034 43040 43046 43050 43059
 43062 43066 43069 43073 43078 43081 43086 43091 43098 43101 43105 43108 43112
 43115 43118 43122 43128 43132 43140 43144 43148 43155 43158 43161 43164 43169
 43173 43176 43180 43183 43185 43191 43196^s 43199 43202 43206 43210 43215^s 43219
 43222 43226 43229 43234 43237 43240 43242 43245 43250 43253 43256 43258 43262
 43265 43269 43271 43274 43282 43285 43288 43316 43321 43325 43328 43333 43336
 43343 43347 43350 43353 43359 43362 43366 43372 43376 43379 43385 43390 43396
 43442 43450 43457 43462 43466 43472 43476 43480 43487 43491 43495 43508 43512
 43516 43521 43525 43534 43540 43546 43551 43555 43563 43568 43574 43584 43587
 43591 43596 43600 43606 43610 43612 43615 43620 43624 43627 43629 43632 43634
 43639 43646 43649 43653 43657 43663 43666 43669 43673 43678 43681 43684^s 43689
 43692 43695 43698 43701 43705 43710 43713 43716 43719 43722 43725 43728 43731
 43734 43737 43741 43743 43745 43748 43751 43758 43760 43764 43769 43773 43776
 43778 43782 43787 43796 43800 43806 43812 43817 43823 43826 43831 43834 43837
 43842 43846 43849 43852 43855 43860 43866 43869 43872 43875 43878 43882 43885
 43888 43890 43893 43899 43902 43905 43911 43922 43925 43930 43932 43936 43940
 43959 43964 43969 43974 43978 43981 43984 43987 43991 43996 43999 44003 44007
 44010 44013 44016 44018 44020 44025 44029 44030^s 44035^s 44037 44040 44042 44045
 44049 44053 44056 44060 44064 44070^s 44072 44075 44078 44081 44083 44087 44089
 44098 44105 44107 44108 44109 44112 44115 44118 44121 44124 44129 44137 44141
 44146 44149 44152 44156 44159 44165 44169 44174 44177 44182 44184 44188 44193
 44195 44199 44203 44207 44211 44214 44218 44221 44225 44228 44234 44241 44266
 44268 44271 44274 44277 44281 44285 44289 44293 44296 44298 44304 44307 44311
 44315 44322 45054 45058 45061 45065 45069 45071 45102 45105 45108 45110 45112
 45116 45128 45130 45134 45137 45138 45140 45142 45145 45147 45150 45165 45168
 45169 45172 45173 45174 45176 45177 45179 45181 45183 45185 45188 45191 45193
 45196 45197 45199 45202 45210 45212 45214 45218 45222 45225 45227 45229 45232
 45234 45238 45242 45243 45248 45250 45252 45254 45256 45259 45263 45265 45267

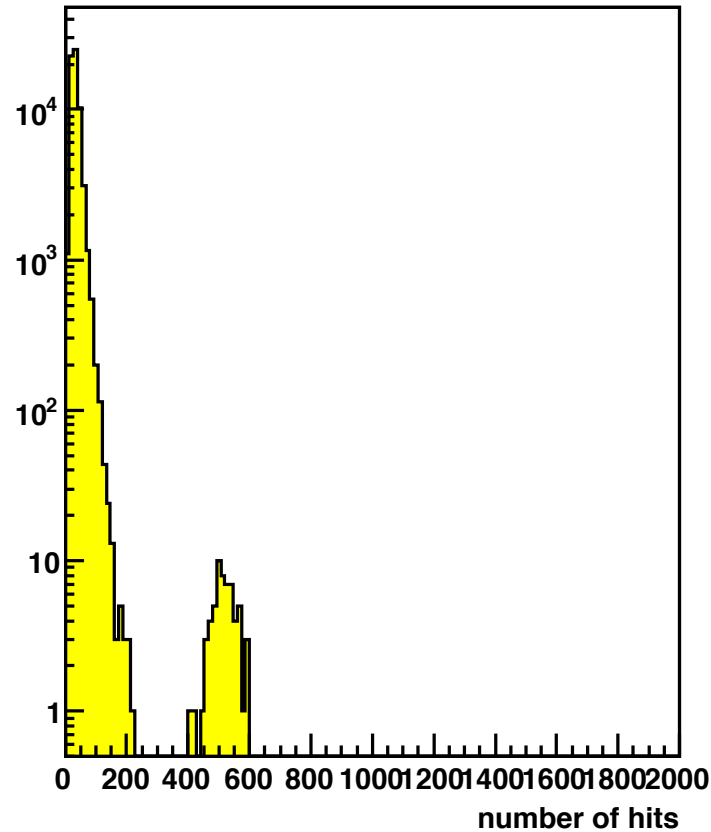


Figure 10.1: Example for a sparking run hit topology: Shown is the number of hits used in the reconstruction. As can be seen a separated bunch of events is visible.

45271 45274 45275 45277 45279 45283 45287 45290 45291 45295 45326 45332 45338
 45342 45349 45354 45356 45358 45363 45367 45379 45385 45388 45391 45393 45395
 45397 45408 45412 45416^e 45419 45424 45431 45435 45438 45440 45442 45444 45446
 45448 45468 45470 45472 45477 45479 45481 45485 45487 45489 45491 45493^e 45495
 45503 45506 45509 45511 45521 45523 45527 45529 45533 45536

10.2 Sparking runs

Runs with an abnormal behavior by one or several optical modules of the detector, so-called sparking runs, have been excluded from the analysis. For most of these runs an isolated population of events with an abnormal high number of events exists. For an example see figure 10.1. Those runs are typically excluded from the corresponding analysis. For further details and picture reference see [125].

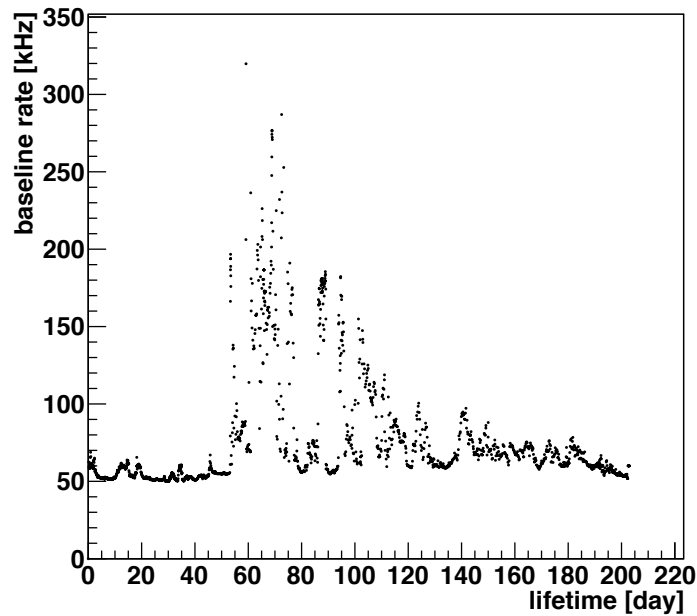


Figure 10.2: Baseline rate as function of lifetime in 2009.

10.3 Baseline rate

Figure 10.2 shows the baseline rate of each run used for the analysis as function of lifetime. As can be seen large variations are observed throughout the year.

10.4 GPS timestamp

To perform transformations (see next section) from local to galactic coordinates events need to be timestamped. This is done by adding relative events to the run start time which is obtained by a GPS board. Unfortunately the connection fails from time to time and the run only obtains a not precise run start time from the DB internal clock. The time difference for runs with both a GPS time and a DB time is plotted in figure 10.3. Figure 10.4 shows the amount of runs with no GPS time.

10.5 Random time generation

Random times used for the generation of scrambled skymaps are generated like this:

```
int64_t frac = random->Uniform(0,31556925e10);
I3Time newtime;
newtime.SetDaqTime(year,frac);
```

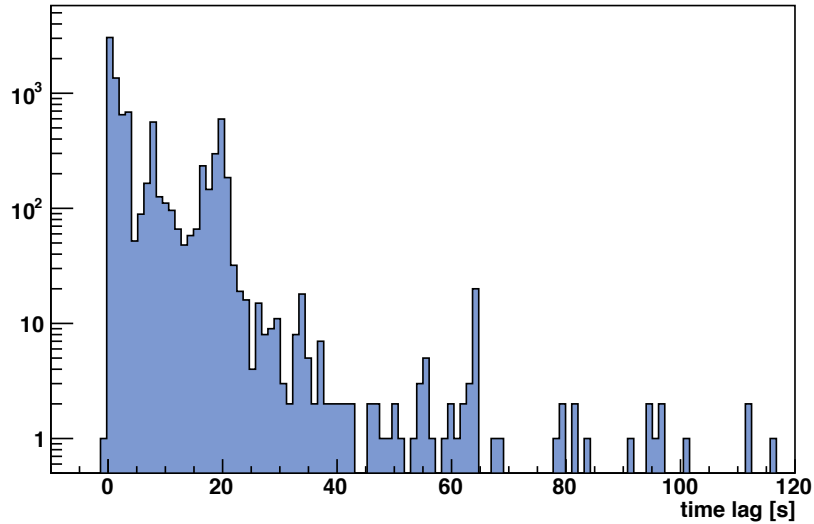


Figure 10.3: Time difference between GPS and DB time. Discrepancies up to two minutes are observed.

10.6 Astro-package and coordinate transformations benchmark

In order to track neutrinos from astrophysical sources, a coordinate transformation from the ANTARES local frame (zenith ϑ , azimuth ϕ) to equatorial coordinates (α , δ) is required. This was done using *SLALIB Positional Astronomy Library* routines inside the Astro-package in SeaTray. The ANTARES detector is located at longitude $\Lambda = 6^\circ 10' = 6.1666666^\circ$ E and latitude $\Phi = 42^\circ 48'$ N. In the ANTARES local frame a track is characterized by two angles:

- zenith $\vartheta \in [0, \pi[$, $\vartheta \in [0; \pi/2[$ corresponds to a down-going track.
- azimuth $\phi \in [0, 2\pi[$.

Table 10.1 contains the benchmark transformation results from local track coordinates (ϑ , ϕ) to equatorial coordinates (α , δ , J2000) for two arbitrary times and eight directions each.

Further the Astro-package has been crosschecked with the ISIS astronomy tool. The result for PKS0208-512 can be seen in figure 10.5.

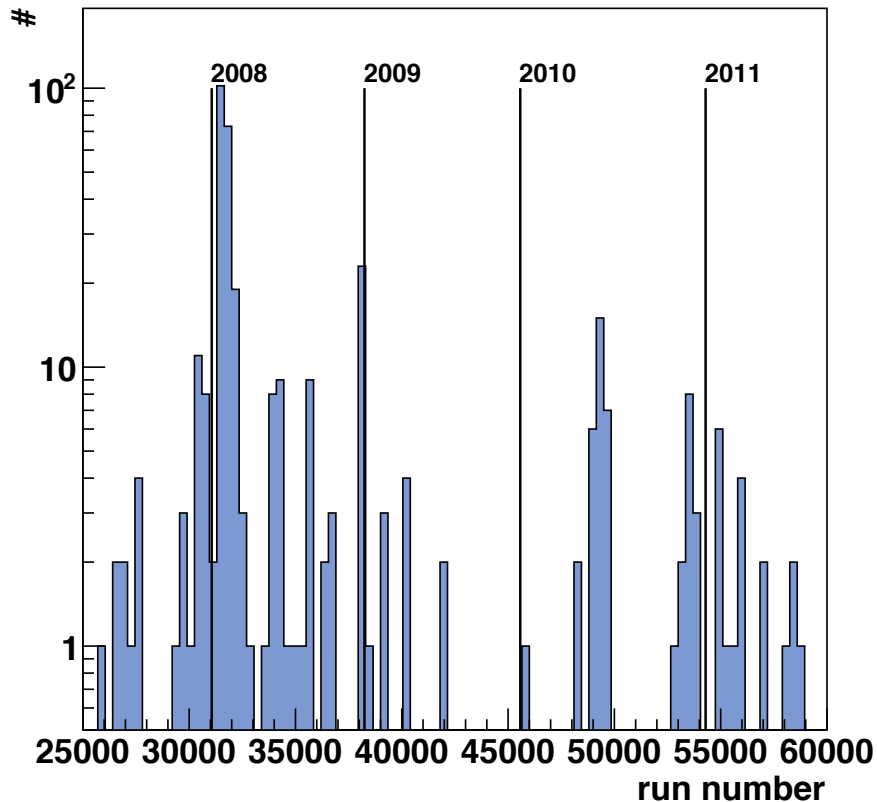


Figure 10.4: Runs with no GPS time.

10.7 Check on SeaTray internal angle conversion

10.8 Additional material on alignment

10.8.1 AlignReco versions

In the following the developed versions and the major improvements of AlignReco are summarized:

- *version 0.98*: The new 2-parameter line fit (v_x, v_y as described in chapter 5) is used, hydrophone positions are now available in the database and read-in from there (before this was done via txt-files due to internal data cleaning procedures).
- *version 0.99*: The hydrophone lever arm is now correctly taken into account. A new database flag, called "invalid", is introduced. It is calculated as $1 + (\text{minimum of hydrophones used on a line})$. This flag can be used as a quality parameter for selecting alignments.

date	time	ϕ	ϑ	α (J2000)	δ (J2000)
04/10/2007	03:03.03	23.46	11.97	260.126	-46.870
04/10/2007	03:03.03	97.07	22.97	235.795	-65.258
04/10/2007	03:03.03	192.50	33.97	206.668	-27.435
04/10/2007	03:03.03	333.33	85.23	313.435	14.422
04/10/2007	03:03.03	23.46	95.23	355.902	-14.598
04/10/2007	03:03.03	97.07	115.32	73.008	-21.391
04/10/2007	03:03.03	192.50	145.42	111.480	41.555
04/10/2007	03:03.03	333.33	179.95	64.165	42.801
27/04/2010	19:19.19	23.46	11.97	347.429	-46.934
27/04/2010	19:19.19	97.07	22.97	323.068	-65.328
27/04/2010	19:19.19	192.50	33.97	293.921	-27.497
27/04/2010	19:19.19	333.33	85.23	40.688	14.409
27/04/2010	19:19.19	23.46	95.23	83.188	-14.562
27/04/2010	19:19.19	97.07	115.32	160.270	-21.324
27/04/2010	19:19.19	192.50	145.42	198.802	41.594
27/04/2010	19:19.19	333.33	179.95	151.445	42.870

Table 10.1: Benchmark coordinate transformations with Astro package in SeaTray.

- *version 0.991*: In order to use hydrophone data obtained using a different set of BSS-coordinated than later used for new detector geometry, different BSS-position handling for hydrophones and line position are included. To discard data from defective or non-proper working tiltmeters and compasses, individual devices can be switched off using a txt-configuration file.
- *version 0.992*: The line lengths are now calculated exactly and individually for each line. In order to speed up the program and limit resources on the database, SQL-commands were rearranged for a parallel data reading at the beginning of each timeslice processing.
- *version 0.993*: Lines shapes that could not be fitted due to missing input data from the measuring devices are obtained by plugging the mean velocity obtained from the other lines into the lineshape formula.
- *version 0.994*: Errors for storey positions included and written to the database.
- *version 0.995*: under construction.

10.8.2 Data format and database tables for detector geometries

All relevant data concerning position calibration is stored in the central ANTARES database at the computing centre at Lyon. The following seven tables are used for the input data (hydrophone positions and data from the TCS; tables for geometrical parameters of the detector are not mentioned here):

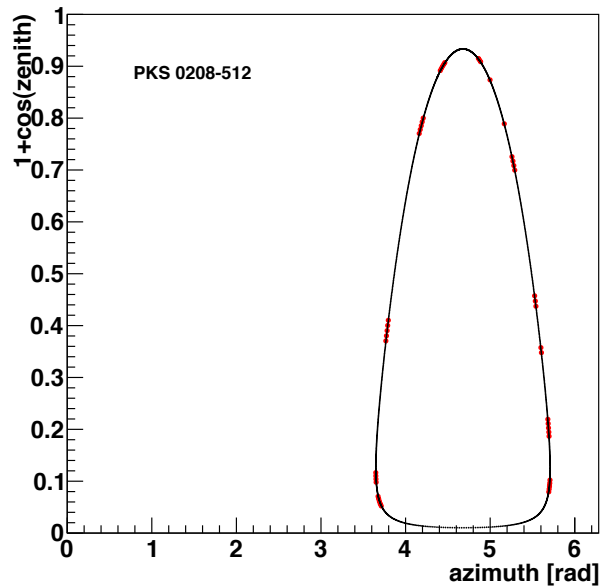


Figure 10.5: Position of source PKS0208-512 in local detector coordinates both using the Astro package (red) and ISIS tools (black) for one sidereal day. A nice agreement is observed.

- `ANTARES.COMPASS_MONITORED_VALUESYYYY`: contains the tiltmeter and compass data from the TCM2 card for year XXXX.
- `ANTARES.HYDRO_POS`: contains the hydrophone positions from the APS.
- `ANTARES.GENISEA_POS(_VALUES)`: contains the hydrophone positions from the APS (outdated).
- `ANTARES.BT_CAL_PAR(_VERSION/_DATA)`: contains the calibration values for the TCS.

For each timeslice and for each storey the UTM X,Y and Z-position (the storey Z-position is defined as the intersection of the OM-plane and the storey axis: 0.576 m above the lower cable attachment of the storey) and the six angles heading, roll and pitch, α , β and γ are recorded. The positioning information is stored in four different tables in the ANTARES DB:

- `ANTARES.ALIGNMENT`: This table contains a row for each timeslice that has been aligned. Columns:
 - `VERSION_ID`: primary key, connection to table `ANTARES.ALIGNMENT_VALUES2`.
 - `LABEL`: contains the software version and the date (e.g. v:0.993 d:2009/12/09 00:00:00).

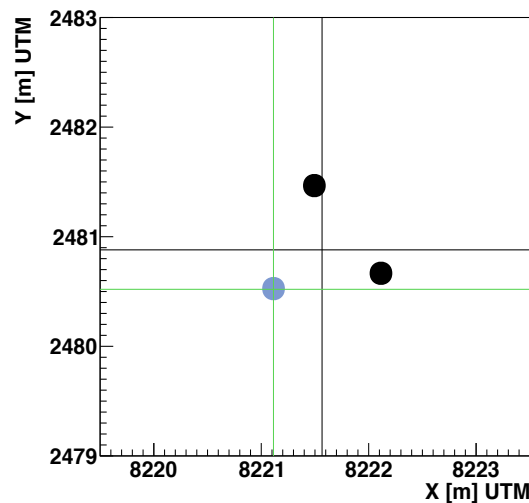


Figure 10.6: Comparison of the UTM-position of OM1 (full blue circle) directly from the heading measurement of the compass and after internal calculation within the SeaTray geometry reader (green crosshair) using Euler angles: Position agree nicely. The black crosshair marks the storey centre.

- USER_ID: user that filled the DB.
- UDATE: creation date.
- USER_COMMENT: contains the number of tiltmeters/hydrophones available on each line. tells you if the line was fitted or calculated (e.g. LF1T12H5 LC2T18H4 ...).
- SOFT_ID: ID of AlignReco version.
- ACC_PERIOD: not used.
- APP_START: begin of timeslice.
- APP_STOP: end of timeslice.
- ISVALID: 1 + min(hydrophones on a line out of 12).
- LINE_POS_ID: VERSION_ID of BBS-position set, data stored in ANTARES.LINE_POSITION and ANTARES.LINE_POSITION_VALUES.
- ANTARES.ALIGNMENT_VALUES: This table contains the OM positions for the nominal alignment. Columns:
 - VERSION_ID: connection to table ANTARES.ALIGNMENT.
 - LCM_ID: LCM-ID (storey ID derived from the IP-address).
 - POSITION: 0,1,2 for the OMs. 3 for the LED-beacons.

- X: X-Position in UTM.
- Y: Y-Position in UTM.
- Z: Z-Position in UTM.
- ANTARES.ALIGNMENT_VALUES2: This table contains the realtime-geometry of ANTARES. Columns:
 - VERSION_ID: connection to table ANTARES.ALIGNMENT.
 - LCM_ID: LCM-ID.
 - POSITION: $100 \cdot \text{Line-ID} + \text{Floor-ID}$ (e.g. L12F22 = 1222).
 - X: X-Position in UTM.
 - Y: Y-Position in UTM.
 - Z: Z-Position in UTM.
 - HEADING: storey heading.
 - PITCH: storey pitch.
 - ROLL: storey roll.
 - ERROR_X: position error.
 - ERROR_Y: position error.
 - ERROR_Z: position error.
 - ERROR_HEADING: angle error.
 - ERROR_PITCH: angle error.
 - ERROR_ROLL: angle error.
 - A1: euler α .
 - A2: euler β .
 - A3: euler γ .
- ANTARES.VELOCITY: This table contains the fitted velocity and velocity error for each line. Columns:
 - VERSION_ID: connection to table ANTARES.ALIGNMENT.
 - LINE: Line-ID (1-12).
 - VELOCITY: velocity from line fit in cm/s.
 - ERROR: error on velocity in cm/s.
 - AZIMUTH: line azimuth.

List of Figures

2.1	Cosmic rays all-particle spectrum	14
2.2	Atmospheric neutrino flux	15
2.3	Neutrino spectrum from GRBs	16
2.4	Diffuse neutrino flux ANTARES	18
2.5	Diffuse neutrino flux IceCube	18
2.6	AGN topology and jet radio emission	19
2.7	M87 jets and radio lobes	20
2.8	Neutrino emission from AGN jets	21
3.1	Illustration: Neutrino detection on Earth	24
3.2	Illustration: Neutrino induced muon in the detector	24
3.3	Feynman-type diagrams for interactions	25
3.4	Muon energy loss and neutrino-muon kinematic angle	26
3.5	Illustration: Cherenkov effect	28
3.6	Depth intensity relation measured by ANTARES	29
3.7	Burst fraction as function of sea current speed	31
3.8	^{40}K coincidence rate	31
3.9	Drawing of the IceCube detector	32
3.10	Artist's view of the KM3NeT detector	33
4.1	Geographical position of the ANTARES site	36
4.2	Detector seabed layout	36
4.3	Schematic view of the ANTARES detector	37
4.4	Drawing of an ANTARES storey	38
4.5	Time calibration via K40-events and LED Optical Beacons	41
4.6	Charge measurement from a lab setup	42
5.1	Histogram of sea current velocity and direction in 2009	46
5.2	Time evolution of sea current velocity and direction	46
5.3	Illustration: Local storey coordinate system	48
5.4	Time evolution of the radial hydrophone positions	50
5.5	Tilt calibration	51
5.6	Heading calibration	51
5.7	Vertical versus horizontal sea current velocity measured by the ADCP in 2009	53
5.8	Illustration: Forces acting on line elements	53
5.9	Illustration: Alignment selection in SeaTray	59
5.10	Line shapes	60

List of Figures

5.11	Difference between hydrophone position and fit	60
5.12	ADCP velocity versus line fit velocity	61
5.13	Heading comparisons with acoustic positioning	62
5.14	Interline velocity comparison	62
5.15	Azimuth comparisons between different lines	64
5.16	Interline velocity direction comparison	64
5.17	Pitch, roll for OM-flooding	65
5.18	Alignment without hydrophone information	65
6.1	Overview of the TANAMI telescopes	69
6.2	TANAMI observation of CenA	69
6.3	TANAMI radio observations of two sources 0208-512 and 0506-612	70
6.4	Redshift distribution of the initial TANAMI sample	71
6.5	Skymap of selected TANAMI sources	72
6.6	Light curve of object PKS0208-512	73
6.7	Variability versus flux	73
6.8	Flow chart of the AAFit-strategy	77
6.9	Lambda versus reconstructed zenith for MC-muons	79
6.10	Quality basic distribution of used runs	79
6.11	β -Distribution of MC atmospheric neutrinos reconstructed better than one degree from the source and mis-reconstructed atmospheric muons	80
6.12	Cumulative number of up-going events in 2009	81
6.13	Generation of scrambled sky maps	82
6.14	Skymap of 534 scrambled data events	83
6.15	RA distribution for scrambled skymaps	83
6.16	Data/MC: Lambda distribution	86
6.17	Data/MC: Azimuth distribution	87
6.18	Data/MC: Zenith distribution	88
6.19	Data/MC: Zenith/Azimuth distribution	89
6.20	Local coordinates for up-going events 2009, $\Lambda > -5.4$	91
6.21	Zenith visibility of two selected sources in ANTARES	92
6.22	Declination distribution of the 24 selected sources	93
6.23	Hour angle distribution	94
6.24	Zenith as function of hour angle	95
6.25	Energy distribution of simulated events	96
6.26	Coordinate check for source simulation	97
6.27	Simulated events as function of declination	98
6.28	Illustration: Cluster building	99
6.29	Source zenith at $\delta = -34^\circ$ versus time	100
6.30	Function $\frac{(rt)^{n-2}}{(n-2)!} e^{-rt} r$	103
6.31	Illustration: Time window within observation period	104
6.32	Cumulative distribution $cd(r, n, T, T_{\text{obs}})$ of the expected number of clusters	105
6.33	p -value calculation	106
6.34	Comparison of theory and data	106
6.35	p -value difference between analytic and numeric calculation	107

6.36	Error estimation on p -value	109
7.1	Discovery potential for sources 2155 and 1424	112
7.2	Discovery potential for sources 0208 and 0506	113
7.3	Discovery potential for sources 0637 and 1057	114
7.4	Discovery potential for sources 2155 and 1057	115
7.5	Discovery potential: Short-duration flare for 0208	117
7.6	Discovery potential: Long-duration flare for 0208-512	117
7.7	Events as function of lifetime	118
7.8	Event rate correlation	118
7.9	Relative residuals of biorate correlation	119
7.10	Distribution of correction factor	119
7.11	Poisson statistics illustration	120
8.1	Skymap of events for unblinding request	123
8.2	Lightcurve 0208-512 for 2009	125
8.3	Limits 0208/1057	126
8.4	Limits 2155/1954	127
8.5	Limits 1424/1104	128
8.6	Limits 00506/0637	129
10.1	Example for sparking run topology	136
10.2	Baseline rate as function of lifetime in 2009	137
10.3	Time difference between GPS and DB time	138
10.4	Runs with no GPS time	139
10.5	Coordinate check for PKS0208-512	141
10.6	Geometry reading in SeaTray.	142

List of Figures

List of Tables

5.1	Time evolution of tiltmeter offsets	52
5.2	Buoancy and drag parameters for the line fit	54
6.1	Table of 24 selected TANAMI sources	74
6.2	Fluxes of 24 selected TANAMI sources	75
6.3	Number of up-going events as function of Λ in 2009	81
6.4	Source subsample for simulation.	93
6.5	Number of expected events as function of source declination	97
6.6	Source visibility fraction for the 24 selected sources	101
7.1	Properties of the short-term flare	116
8.1	Found events and limits	124
10.1	Benchmark coordinate transformations	140

List of Tables

Bibliography

- [1] ANTARES Coll., S Adrin-Martnez et al., “The positioning system of the antares neutrino telescope,” *Journal of Instrumentation*, vol. 7, no. 08, p. T08002, 2012.
- [2] Baikal homepage: <http://baikalweb.jinr.ru>.
- [3] Amanda homepage: <http://amanda.uci.edu>.
- [4] IceCube Collaboration, “Evidence for high-energy extraterrestrial neutrinos at the icecube detector,” *Science*, vol. 342, no. 6161, 2013.
- [5] Tanami homepage: <http://pulsar.sternwarte.uni-erlangen.de/tanami>.
- [6] C. Müller et al., “Southern-Hemisphere AGN Monitoring on (Sub-)Parsec Scales: The TANAMI Program,” *ArXiv e-prints*, May 2012.
- [7] Fermi homepage: <http://fermi.gsfc.nasa.gov>.
- [8] C. Amsler et al. (Particle Data Group) *Physics Letter*, vol. 667, 2008.
- [9] T. Gaisser, “Atmospheric neutrino fluxes,” *Physica Scripta*, vol. 2005, no. T121, p. 51, 2005.
- [10] D. Stransky, “Cosmogenic Neutrinos in KM3Net,” 2012. Diploma thesis in preparation, University of Erlangen-Nuremberg (ECAP).
- [11] G. Battistoni, A. Ferrari, T. Montaruli, P.R. Sala, “The fluka atmospheric neutrino flux calculation,” *Astroparticle Physics*, vol. 19, no. 2, pp. 269 – 290, 2003.
- [12] V. Agrawal et al., “Atmospheric neutrino flux above 1 GeV,” *Phys. Rev. D*, vol. 53, pp. 1314–1323, Feb 1996.
- [13] M. Honda et al., “Calculation of the flux of atmospheric neutrinos,” *Phys. Rev. D*, vol. 52, pp. 4985–5005, Nov 1995.
- [14] L.V. Volkova, “Energy spectra and angular distributions of atmospheric neutrinos,” *Sov.J.Nucl.Phys.*, vol. 31, 1980.
- [15] T.K. Gaisser, “Atmospheric Neutrinos,” in *Next Generation Nucleon Decay and Neutrino Detectors NNN06* (J. R. Wilkes, ed.), vol. 944 of *American Institute of Physics Conference Series*, pp. 140–142, Nov. 2007.

Bibliography

- [16] T. Kajita and Y. Totsuka, “Observation of atmospheric neutrinos,” *Rev. Mod. Phys.*, vol. 73, pp. 85–118, Jan 2001.
- [17] K. Jung et al., “Oscillations of atmospheric neutrinos,” *Ann. Revs. Nucl. Part. Sci.*, vol. 51, 2001.
- [18] T.K. Gaisser, “Atmospheric neutrino fluxes,” *Nuclear Physics B - Proceedings Supplements*, vol. 118, pp. 109 – 117, 2003. Proceedings of the XXth International Conference on Neutrino Physics and Astrophysics.
- [19] H. Yüksel, J.F. Beacom, “Neutrino spectrum from SN 1987A and from cosmic supernovae,” *Phys. Rev. D*, vol. 76, pp. 083007–+, Oct. 2007.
- [20] A. Esteban-Pretel, “Supernovae as laboratories for neutrino properties,” *ArXiv e-prints*, Dec. 2009.
- [21] W.C. Haxton, “Neutrino Astrophysics,” *ArXiv e-prints*, Aug. 2008.
- [22] J. Schmid, “Gamma Ray Bursts with ANTARES,” 2011. Diploma thesis, University of Erlangen-Nuremberg (ECAP).
- [23] E. Waxman, J. Bahcall, “High Energy Neutrinos from Cosmological Gamma-Ray Burst Fireballs,” *Physical Review Letters*, vol. 78, pp. 2292–2295, Mar. 1997.
- [24] S.E. Woosley, J.S. Bloom, “The Supernova Gamma-Ray Burst Connection,” *Annual Review of Astronomy and Astrophysics*, vol. 44, pp. 507–556, sep 2006.
- [25] T. Piran, “Black Holes and High Energy Astrophysics,” *H. Sato & N. Sugiyama (ed.) Frontiers Science Series 23*, vol. 78, p. 217, mar 1998.
- [26] IceCube Coll., R. Abbasi et al., “Search for muon neutrinos from gamma-ray bursts with the icecube neutrino telescope,” *The Astrophysical Journal*, vol. 710, no. 1, p. 346, 2010.
- [27] IceCube Coll., R. Abbasi et al., “An absence of neutrinos associated with cosmic-ray acceleration in γ -ray bursts,” *Nature*, vol. 484, pp. 351–354, 2012.
- [28] H. Motz, “Dark Matter Search with ANTARES,” 2011. PhD thesis, University of Erlangen-Nuremberg (ECAP), Germany.
- [29] P. Gondolo, J. Edsjö, P. Ullio, L. Bergström, M. Schelke, E.A. Baltz, “DarkSUSY: computing supersymmetric dark matter properties numerically,” *Journal of Cosmology and Astroparticle Physics*, vol. 7, pp. 8–+, July 2004.
- [30] IceCube Coll., R. Abbasi et al., “The Design and Performance of IceCube DeepCore,” *Astropart. Phys.*, pp. 615–624, May 2012.
- [31] IceCube Coll., R. Abbasi et al., “Search for dark matter from the galactic halo with the icecube neutrino telescope,” *Phys. Rev. D*, vol. 84, p. 022004, Jul 2011.

- [32] ANTARES Coll., J.A. Aguilar et al., “Search for a diffuse flux of high-energy ν_μ with the antares neutrino telescope,” *Physics Letters B*, vol. 696, no. 1-2, pp. 16 – 22, 2011.
- [33] IceCube Coll., R. Abbasi et al., “Search for a diffuse flux of astrophysical muon neutrinos with the IceCube 40-string detector,” *Phys. Rev. D*, vol. 84, p. 082001, Oct. 2011.
- [34] E. Waxman, J. Bahcall, “High energy neutrinos from astrophysical sources: An upper bound,” *Phys. Rev. D*, vol. 59, p. 023002, Dec 1998.
- [35] J. Bahcall, E. Waxman, “High energy astrophysical neutrinos: The upper bound is robust,” *Phys. Rev. D*, vol. 64, p. 023002, Jun 2001.
- [36] K. Mannheim, R.J. Protheroe, J.P. Rachen, “Cosmic ray bound for models of extragalactic neutrino production,” *Phys. Rev. D*, vol. 63, p. 023003, Dec 2000.
- [37] http://www.auger.org/news/PRagn/images/agn4_prouza.png.
- [38] <http://outreach.atnf.csiro.au/images/astronomical/images/j0116-473.gif>.
- [39] Hubble site: <http://www.spacetelescope.org/images/opo9943b/>.
- [40] G. Morlino, P. Blasi, E. Amato, “Gamma rays and neutrinos from SNR RX J1713.7-3946,” *Astropart. Phys.*, vol. 31, pp. 376–382, June 2009.
- [41] J.K. Becker, P.L. Biermann, “Neutrinos from active black holes, sources of ultra high energy cosmic rays,” *Astropart. Phys.*, vol. 31, pp. 138–148, Mar. 2009.
- [42] D. Osterbrock, “Astrophysics of Gaseous Nebulae and Active Galactic Nuclei,” *University Science Books: Mill Valley*, 1989.
- [43] Fermi-Jansky workshop 2010: http://www.mpifr-bonn.mpg.de/div/vlbi/agn2010/PdfFiles/fmj2010_complete.pdf.
- [44] B. Hartmann, “Reconstruction of Neutrino-Induced Hadronic and Electromagnetic Shower with the ANTARES Experiment,” 2006. PhD thesis, University of Erlangen-Nuremberg, Germany.
- [45] F. Folger, “Reconstruction of neutrino induced hadronic showers with the ANTARES neutrino telescope,” 2009. Diploma thesis, University of Erlangen-Nuremberg, Germany.
- [46] ANTARES Coll., J.A. Aguilar et al., “Amadeus-the acoustic neutrino detection test system of the antares deep-sea neutrino telescope,” *Nuclear Instruments and Methods in Physics Research Section A: Accelerators, Spectrometers, Detectors and Associated Equipment*, vol. 626-627, pp. 128 – 143, 2011.
- [47] S.I. Klimushin, E.V. Bugaev, I.A. Sokalski, “Precise parametrizations of muon energy losses in water,” 2001. Proceedings of the 27th ICRC Hamburg.

Bibliography

- [48] ANTARES Coll., “A Deep Sea Telescope for High Energy Neutrinos,” *ArXiv Astrophysics e-prints*, July 1999.
- [49] ANTARES Coll., J.A. Aguilar et al., “Transmission of light in deep sea water at the site of the Antares neutrino telescope,” *Astropart. Phys.*, vol. 23, pp. 131–155, 2005.
- [50] R. C. Smith and K. S. Baker, “Optical properties of the clearest natural waters (200-800 nm),” *Appl. Opt.*, vol. 20, pp. 177–184, 1981.
- [51] R.M. Pope, E.S. Fry, “Absorption spectrum (380-700 nm) of pure water. II. Integrating cavity measurements,” *Appl. Opt.*, vol. 36, pp. 8710–8723, 1997.
- [52] M. de Jong, “On the attenuation of light in water,” 2011. ANTARES-PHYS-2011-008.
- [53] ANTARES Coll., J.A. Aguilar et al., “Transmission of light in deep sea water at the site of the antares neutrino telescope,” *Astroparticle Physics*, vol. 23, no. 1, pp. 131 – 155, 2005.
- [54] ANTARES Coll., J.A. Aguilar et al., “Zenith distribution and flux of atmospheric muons measured with the 5-line ANTARES detector,” *Astropart. Phys.*, vol. 34, pp. 179–184, 2010.
- [55] T. Karg for the Icecube Coll., “The IceCube neutrino observatory: status and initial results,” *Astrophysics and Space Sciences Transactions*, vol. 7, pp. 157–162, Apr. 2011.
- [56] K. Young, “DUMAND-II (deep underwater muon and neutrino detector) progress report,” vol. 338 of *American Institute of Physics Conference Series*, pp. 886–892, July 1995.
- [57] R. Wischnewski for the BAIKAL Coll., “The BAIKAL neutrino experiment - physics results and perspectives,” *ArXiv e-prints*, Nov. 2008.
- [58] R. Wischnewski for the BAIKAL Coll., “The Baikal Neutrino Telescope: Selected Physics Results,” *ArXiv e-prints*, Oct. 2007.
- [59] NEMO homepage: <http://nemoweb.lns.infn.it>.
- [60] NEMO Coll., P. Sapienza, “The NEMO project: Achievements and perspectives,” *J. Phys. Conf. Ser.*, vol. 120, p. 062010, 2008.
- [61] M. Taiuti et al., “The NEMO project: A status report,” *Nucl. Instrum. Meth.*, vol. A626-627, pp. S25–S29, 2011.
- [62] IceCube Coll., T. De Young et al., “Results from seven years of AMANDA-II,” *Journal of Physics Conference Series*, vol. 136, pp. 022046–+, Nov. 2008.

- [63] IceCube homepage: <http://icecube.wisc.edu>.
- [64] U.F. Katz, “Neutrino telescoping in the Mediterranean sea,” *Prog. Part. Nucl. Phys.*, vol. 57, pp. 273–282, 2006.
- [65] U.F. Katz, “KM3NeT: Towards a km³ Mediterranean neutrino telescope,” *Nucl. Instrum. Meth.*, vol. A567, pp. 457–461, 2006.
- [66] P. Coyle for the ANTARES Coll., “The antares deep-sea neutrino telescope: status and first results,” 2009.
- [67] ANTARES Coll., M. Ageron et al., “Performance of the First ANTARES Detector Line,” *ArXiv e-prints*, Dec. 2008.
- [68] ANTARES homepage: <http://antares.in2p3.fr>.
- [69] Hamamatsu homepage: http://sales.hamamatsu.com/assets/pdf/parts_R/LARGE_AREA_PMT_TPMH1286E05.pdf.
- [70] J. Brunner, “Using video for science,” Presentation at “Deep Ocean Cabled Observatories”, Amsterdam, 24-25 may 2012.
- [71] ANTARES Coll., P. Amram et al., “The ANTARES optical module,” *Nucl. Instrum. Meth.*, vol. A484, pp. 369–383, 2002.
- [72] ANTARES Coll., CAU CEFREM Coll., P. Amram et al., “Sedimentation and fouling of optical surfaces at the ANTARES site,” *Astropart. Phys.*, vol. 19, pp. 253–267, May 2003.
- [73] ANTARES Coll., M. Ageron et al., “The ANTARES optical beacon system,” *Nucl. Instrum. Meth.*, vol. A578, pp. 498–509, 2007.
- [74] G.A. Askaryan et al., “Acoustic detection of high energy particle showers in water,” *Nucl. Instr. and Meth.*, vol. 164, pp. 267–278, 1979.
- [75] Buoy manufacturer: <http://www.trelleborg.com>.
- [76] ANTARES Coll., M. Ageron et al., “ANTARES: the first undersea neutrino telescope,” *ArXiv e-prints*, Apr. 2011.
- [77] ANTARES Coll., J.A. Aguilar et al., “The data acquisition system for the ANTARES neutrino telescope,” *Nucl. Instrum. Meth.*, vol. A570, pp. 107–116, 2007.
- [78] ANTARES Coll., J.A. Aguilar et al., “Performance of the front-end electronics of the ANTARES neutrino telescope,” *Nuclear Instruments and Methods in Physics Research A*, vol. 622, pp. 59–73, Oct. 2010.
- [79] F. Feinstein, “The analogue ring sampler: A front-end chip for ANTARES,” *Nucl. Instr. and Meth. A*, vol. 504, pp. 258–261, 2003.

Bibliography

- [80] ANTARES Coll., M. Ageron et al., “The antares telescope neutrino alert system,” *Astropart. Phys.*, vol. 35, no. 8, pp. 530–536, 2012.
- [81] ROOT homepage: <http://root.cern.ch>.
- [82] GCN network homepage: <http://gcn.gsfc.nasa.gov>.
- [83] SNEWS homepage: <http://snews.bnl.gov>.
- [84] ANTARES Coll., J.A. Aguilar et al., “Time Calibration of the ANTARES Neutrino Telescope,” *Astropart. Phys.*, vol. 34, pp. 539–549, 2011.
- [85] J. Aguilar, “Analysis of the Optical Beacon system and search for point-like sources in the ANTARES neutrino telescope,” 2007. PhD thesis, University of Valencia, <http://antares.in2p3.fr/Publications>.
- [86] J. Zornoza, “Characterization of two photomultiplier models and study by Monte Carlo simulation of several calibration systems based on optical beacons for the ANTARES detector,” 2011.
- [87] B. Baret for the ANTARES Coll., “Charge Calibration of the ANTARES high energy neutrino telescope,” 2009.
- [88] G. Halladjian, “Recherche de neutrinos cosmiques de haute-energie emis par des sources ponctuelles avec ANTARES,” 2010. PhD thesis, CPPM.
- [89] H. van Haren et al., “Acoustic and optical variations during rapid downward motion episodes in the deep north-western Mediterranean Sea,” *Deep Sea Research Part I: Oceanographic Research*, vol. 58, pp. 875–884, Aug. 2011.
- [90] C. Millot, “Circulation in the western mediterranean sea,” *Journal of Marine Systems*, vol. 20, pp. 423–442, 1999.
- [91] P. Vernin, “The UTM grid,” 2008. ANTARES-SOFT-2008-002.
- [92] UTM grid: <http://dmap.co.uk/utmworld.htm>.
- [93] Earth magnetic field: <http://www.ngdc.noaa.gov/seg/geomag>.
- [94] UTM grid: <http://www.pnicorp.com>.
- [95] Earth magnetic field: <http://www.ngdc.noaa.gov/geomag/magfield.shtml>.
- [96] G. Lelaizant, “Acoustic Positioning,” 2007. ANTARES-SLOW-2007-001.
- [97] R. J. Urick, “Principles of underwater sound,” 1983. ISBN 0-932146-62-7.
- [98] T. Eberl and C. Kopper, “The SeaTray software framework,” 2009. ANTARES-SOFT-2009-013.

- [99] R. Lahmann for the ANTARES Coll., “Status and Recent Results of the Acoustic Neutrino Detection Test System AMADEUS,” *ArXiv e-prints*, Apr. 2011.
- [100] A. Gleixner, “Spezielle Methoden zur Berechnung der Geometrie des ANTARES-Detektors,” 2011. Diploma thesis, University of Erlangen-Nuremberg (ECAP).
- [101] M.M. Reynoso, M.C. Medina, G.E. Romero, “A lepto-hadronic model for high-energy emission from FR I radiogalaxies,” *A&A*, vol. 531, p. A30, 2011.
- [102] J.G. Learned, K. Mannheim, “High-Energy Neutrino Astrophysics,” *Annu. Rev. Nucl. Part. Sci.*, vol. 50, pp. 679–749, 2000.
- [103] matthias.kadler@astro.uni-wuerzburg.de.
- [104] jörn.wilms@sternwarte.uni-erlangen.de.
- [105] C. Mueller, “High resolution VLBI observations of Centaurus A,” 2010. Diploma thesis, University of Erlangen-Nuremberg (ECAP).
- [106] R. Ojha et al., “TANAMI: tracking active galactic nuclei with austral milliarcsecond interferometry . I. First-epoch 8.4 GHz images,” *A&A*, vol. 519, p. A45, Sept. 2010.
- [107] LBA homepage: <http://www.atnf.csiro.au/vlbi>.
- [108] Veron catalogue homepage: <http://heasarc.gsfc.nasa.gov/W3Browse/all/veroncat.html>.
- [109] M. Stickel, K. Meisenheimer, H. Kuehr, “The optical identification status of the 1 Jy radio source catalogue,” *Astronomy and Astrophysics Suppl.*, vol. 105, pp. 211–234, June 1994.
- [110] Mojave homepage <https://www.physics.purdue.edu/astro/mojave>.
- [111] Fermi-LAT Coll., A.A. Abdo et al., “Fermi large area telescope first source catalog,” *The Astrophysical Journal Supplement Series*, vol. 188, no. 2, p. 405, 2010.
- [112] Fermi-LAT Coll., P.L. Nolan et al., “Fermi Large Area Telescope Second Source Catalog,” *The Astrophysical Journal Supplement Series*, vol. 199, p. 31, Apr. 2012.
- [113] NED database: <http://ned.ipac.caltech.edu>.
- [114] ANTARES Coll., J.A. Aguilar et al., “A fast algorithm for muon track reconstruction and its application to the antares neutrino telescope,” *Astropart. Phys.*, vol. 34, no. 9, pp. 652 – 662, 2011.

Bibliography

- [115] A. Heijboer, “Track Reconstruction and Point Source Searches with ANTARES,” 2004. PHD thesis, NIKHEF.
- [116] M. Anghinolfi, H. Costantini, K. Fratini, D. Piombo, M. Taiuti, “New measurement of the angular acceptance of the Antares Optical Module,” 2008. ANTARES-OPMO-2008-001.
- [117] F. Fehr, “Systematic studies, calibration, and software development for event reconstruction and data analysis using the ANTARES deep-sea neutrino telescope,” 2011. PHD thesis, University of Erlangen-Nuremberg (ECAP).
- [118] SLALIB homepage: <http://www.starlink.rl.ac.uk/docs/sun67.htx/sun67.html>.
- [119] G. Carminati, A. Margiotta, M. Spurio, “Mupage: a muon generator from parametric formulas,” 2006. ANTARES-PHYS-2006-003.
- [120] K. Kuzmin, T. Montaruli, I.A. Sokalski, “GENHEN v6r3: implementation of the Glashow resonance and of MUSIC transport code,” 2004. ANTARES-SOFT-2004-012.
- [121] L. T. S. Navas, “KM3 User Guide and Reference Manual,” 1999. ANTARES-SOFT-1999-011.
- [122] Geasim ANTARES internal documentation:
<http://antares.in2p3.fr/internal/software/geasim.html>.
- [123] GEANT4 homepage: <http://geant4.cern.ch>.
- [124] M. de Jong, “The TriggerEfficiency Program,” 2009. ANTARES-SOFT-2009-001.
- [125] A. H. Claudio Bogazzi, Joris Hartman, “Point Source Search with 2007 and 2008 data,” 2010. ANTARES-PHYS-2010-008.
- [126] A. Kappes, U. Katz, “On the Use of Event Weights for the Simulation of Atmospheric Muons in ANTARES,” 2005. ANTARES-SOFT-2005-003.
- [127] J. Brunner, “Updated tag list for the new ANTARES event format,” 1999. ANTARES-SOFT-1999-003.
- [128] IceCube Collaboration, S. Tilav et al. , “Atmospheric Variations as observed by IceCube,” *ArXiv e-prints*, Jan. 2010.
- [129] Adrian-Martinez, S. and others, “Search for Cosmic Neutrino Point Sources with Four Year Data of the ANTARES Telescope,” 2012.

Danksagung

Zunächst möchte ich Prof. Uli Katz danken für all die Unterstützung, die vielen physikalischen und nicht-physikalischen Gespräche in seinem auf Kühlschranktemperatur befindlichen kleinen Büro. Ich danke für die vielen Reisen zu ANTARES-Schichten ans schöne Mittelmeer, zu ANTARES-Meetings und Konferenzen in ganz Europa. Lieber Uli, Dein Büro war und ist immer 'offen' für ein herzliches Wort (auch sonntags um 22:00 Uhr).

Ein großer Dank auch an Prof. Gisela Anton für die schöne Zeit bei ANTARES, die Zweitkorrektur meiner Arbeit und die gute Zusammenarbeit im Rahmen der Erstsemesterübungen in Experimentalphysik. Ein großes Dankeschön auch für die großzügige Finanzierung des Käses an den zahlreichen ECAP-Weinproben.

Besonderer Dank gilt Clancy James und Thomas Eberl, die mich für den zweiten Teil dieser Arbeit intensiv betreut haben, mit denen ich viele fachliche Dinge diskutiert habe und die mich bei der Präsentation auf diversen ANTARES-Meetings und im Rahmen des Unblinding-Prozesses sehr unterstützt haben. Dank auch an Alexander Kappes, der diese Analyse mit eingeleitet hat.

Ich danke Holger Motz und Jürgen Hoessl und Robert Lahmann für die gute Zusammenarbeit zum Alignment bei ANTARES, die schließlich zum ersten Teil dieser Arbeit und zu einem Paper geführt hat. Danke an Holger für seine vielen softwaretechnischen Hilfen und die großartigen kulinarischen Erlebnisse während der Zeit in Erlangen.

Ich danke Tilman Rügheimer für diverse 'Cafe subito' und viele unvergeßliche Weinproben. Danke an die Zimmerkollegen Julia Schmid und Andreas Spies für eine schöne Zeit unten im Labor.

Danke an Kay Graf, Claudio Kopper und Thomas Eberl für Support rund um Software und um SeaTray im Speziellen.

Ich danke Cornelia Müller, Kerstin Fehn, Moritz Böck, Prof. Matthias Kadler und Prof. Jörn Wilms für ihre Hilfe von Seiten TANAMI und bei Fragestellungen der astronomischen Art.

Ich danke Frau Kühn und Frau Maerker für eine immer freundliche Aufnahme im Sekretariat und ihre große Hilfe beim Ausfüllen der Reisekostenabrechnungen.

Zuletzt bleibt mir noch meiner lieben Familie und meinem Engel Kathrin zu danken, die mich sehr oft aufgemuntert und mich niemals im Stich gelassen haben. Ich weiß, dass dieses Projekt Euch viele Nerven gekostet hat. Danke, dass ihr da seid und ward und mir die nötige Kraft gegeben habt. Ich werde das niemals vergessen.